

Reconstruction of Cardiomyocyte Growth and Remodeling Networks

A Dissertation

Presented to

the faculty of the School of Engineering and Applied Science

University of Virginia

in partial fulfillment
of the requirements for the degree

Doctor of Philosophy

by

Philip M. Tan

August 2018

APPROVAL SHEET

This Dissertation
is submitted in partial fulfillment of the requirements
for the degree of
Doctor of Philosophy

Author Signature: _____

This Dissertation has been read and approved by the examining committee:

Advisor: Jeffrey J. Saucerman

Committee Member: Jeffrey W. Holmes

Committee Member: Robert K. Nakamoto

Committee Member: Matthew J. Wolf

Committee Member: Zhen Yan

Committee Member: _____

Accepted for the School of Engineering and Applied Science:



Craig H. Benson, School of Engineering and Applied Science

August 2018

In honor of Dr. R. James Swanson.

“But I was thinking of a plan to dye one’s whiskers green...”

—Lewis Carroll, *Through the Looking-Glass*

Abstract

Alterations in cardiomyocyte shape and function are critical to the heart's adaptive capability. Physiological stresses such as exercise can induce beneficial growth of the myocardium, but pathological stresses such as hypertension or myocardial infarction can launch a downward spiral of hypertrophic remodeling. This remodeling of the heart walls results in decompensation due to abnormal chamber geometry and excessive wall thickening or thinning. While many biochemical and mechanical processes influencing cardiac hypertrophy have been isolated, the precise signaling mechanisms separating adaptive and maladaptive responses have remained uncertain. Given the complexity of the cardiac signaling network, a systems-level approach is necessary to tackle this challenge. The overall goal of this dissertation is to integrate high-content image analysis and computational network modeling to identify novel control structures and pathways underlying cardiomyocyte growth and remodeling.

We first examine how cardiomyocytes integrate remodeling signals caused by mechanical stretch, a potent stimulus for growth and remodeling in cells. Although many pathways have been implicated in stretch-induced remodeling, the control structures by which signals from distinct mechano-sensors are integrated to modulate hypertrophy and gene expression in cardiomyocytes remain unclear. We constructed and validated a predictive computational model of the cardiac mechano-signaling network in order to elucidate the mechanisms underlying signal integration. The model identifies calcium, actin, Ras, Raf1, PI3K, and JAK as key regulators of cardiac mechano-signaling and characterizes crosstalk logic imparting differential control of transcription by AT1R, integrins, and calcium channels. We find that while these regulators maintain mostly independent control over distinct groups of transcription factors, synergy between multiple pathways is necessary to activate all the transcription factors necessary for gene transcription and hypertrophy. We also identify a PKG-dependent mechanism by which

valsartan/sacubitril, a combination drug recently approved for treating heart failure, inhibits stretch-induced hypertrophy, and predict further efficacious pairs of drug targets in the network through a networkwide combinatorial search.

Next, we expand the focus to multiple stimuli and investigate which pathways control variant remodeling outcomes in cardiomyocytes. Although previous studies have mapped out the hypertrophy signaling network and have matched network inputs to a variety of morphological phenotypes, the contribution of individual signaling pathways to distinct hypertrophic morphologies, such as area versus elongation, remains relatively unknown. We measured protein expression and activity in response to angiotensin II, endothelin-1 (ET), insulin growth factor-1, and neuregulin-1 (Nrg), and integrated this data with a previously published phenotypic screen in a partial least squares regression model. The model identifies two axes of signaling activity corresponding to growth and eccentricity. Nrg, which produces myocyte elongation, was found to highly activate members of the MAPK and PI3K signaling pathways, whereas Nrg and ET both downregulate apoptotic signaling. Follow-up experiments validated the role of MEK1, PI3K, and Src in mediating Nrg-induced myocyte elongation, whereas MEK5 and p38 were not found to be involved in this process. Our results illuminate the cell-level decisions driving concentric versus eccentric ventricular remodeling.

Finally, we broaden the scope to a genome-wide search and identify novel targets not previously implicated in myocyte growth and remodeling. Although large phenotypic screens have the potential to elucidate novel biological discoveries, they present unique obstacles and challenges to analysis due to the scale of the data. We develop automated image processing algorithms to process a myocyte screen comprising 10 million images and 97,500 shRNAs targeting 15,000 genes. To correct for artifacts common to large screens, such as varying cell health and image quality, we introduce a robust filtering and normalization procedure. We also generate a binomial model and perform a randomized analysis, which indicate that at least two shRNA hits per gene are necessary to avoid high false positive rates. Implementing this workflow, we locate 294 genes regulating myocyte area, 360 genes regulating

elongation, and 345 genes regulating spikiness. Each gene set is highly enriched for cytoskeletal remodeling and for cardiac disease terms, such as congestive heart failure, hypertrophic cardiomyopathy, and dilated cardiomyopathy. Our results not only identify hundreds of candidates for future study, but also validate a comprehensive analysis pipeline for use on other large-scale screens.

Together, the work encompassed in these aims (Fig. 0.1) accomplishes three goals. First, we have identified signaling pathways driving variant myocyte phenotypes. Second, we have discovered new biochemical targets for modulating cardiac remodeling. Third, we have developed innovative image processing algorithms for assessing myocyte form and function. In summary, our systems approach illuminates the complex signaling driving heart failure and contributes to the accelerated development of novel therapies.

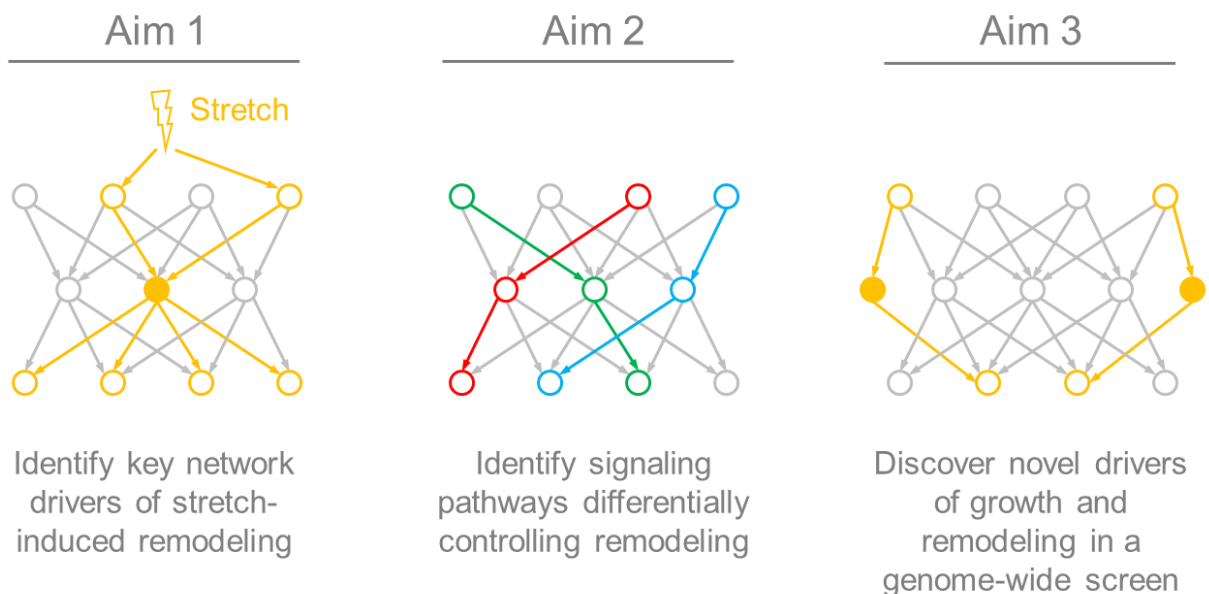


Figure 0.1. Schematic of research plan. The three aims listed correspond to chapters 2, 3, and 4 of this work.

Acknowledgements

“What hast thou that thou didst not receive?” The last five years have juxtaposed my weakness and inadequacy with the generosity of others. First, many thanks to Jeff Saucerman, my advisor. You have encouraged me to persist and have never displayed frustration with my experimental failures. You let me join the lab when I knew nothing about cardiology, cell culture, or even the point of grad school. I aspire to your example of always having your door open for questions. Thank you especially for encouraging my teaching interests, for letting me co-instruct your course, and for providing opportunities to mentor.

I am grateful to Jeff Holmes, Bob Nakamoto, Matt Wolf, and Zhen Yan, my committee members, for experimental troubleshooting and for an enjoyable comprehensive exam. Kevin Janes taught me how to read and write a scientific paper. Chris Smolko initiated me into the secrets of qPCR. I have never met Kyle Buchholz, the co-author of my first paper, in person, but our 53,000-word email correspondence jumpstarted chapter 2 when it was languishing and brought it to completion.

During the difficult transition to graduate studies, Tristan Jones, Pranav Aurora, and Renata Polanowska-Grabowska taught me almost everything I know about cell culture. They also calmed my anxieties, sympathized with my complaints, and kept me from dropping out. Robert Amanfu, Karen Ryall, and Eric Greenwald set a cheerful and collegial tone for the lab as they passed the baton to the next generation. Gabby Maldonado self-sacrificially took over all my lab duties during the last year.

Angela Zeigler, Laura Woo, and Bryan Chun, thanks for being my labmates. You sharpened my thinking and endured my idiosyncrasies. Angela, thank you for your blunt and constructive feedback in lab meetings, and for teaching me not to take myself too seriously. Bryan, thank you for teaching me to ski and for sharing your exotic delicacies. Laura, thank you for being a kind and honest friend.

I have been privileged to work with several creative and dedicated undergraduates and post-baccalaureates. Matt Sutcliffe, John Hulse, Matt van de Graaf, and Elizabeth Snyder-Mounts have given me practice in mentoring, coped with my perfectionism, and accelerated the work presented here. In particular, chapter 4 would not exist apart from Matt van de Graaf's dogged efforts.

I cannot sufficiently thank "Rocky" and "Sparky" (Henry Pritchard and Tracy Burcin) for cheerfully allowing me to disrupt their day with IT questions time out of mind. Both of them have gone out of their way to give me access to equipment and to rescue me from self-inflicted disasters.

It would be impossible to acknowledge the many friends and mentors outside the University who have cheered me on, but I especially want to thank Fitz Green, Patrick Timmis, Joshua Drake, Rick Gross, and Jane Gresham for their prayers and heartening words. Bradley Weaver and John Lawson, thank you for your friendship in Christ and for putting up with Bounty. Finally, thanks to my family—Mom, Dad, Katherine, Isaac, Miriam, Evelyn, Annika, Benjamin, Elisabeth, Peter, Joshua, and Titus. Thank you for encouraging me to ask questions. Thank you for sending cookies and answering my phone calls. Thank you for teaching me that only one thing is necessary.

Philip Tan

May 2018

S.D.G.

This work has been made possible by generous support from the University of Virginia NIH Cell and Molecular Biology Training Grant and from the Sture G. Olsson Engineering Fellowship.

Table of contents

Abstract.....	ii
Acknowledgements.....	v
Table of contents.....	vii
List of figures and tables.....	xi
Abbreviations.....	xiii
Chapter 1: Background and significance	1
1.1. Foreword.....	2
1.2. Introduction.....	2
1.3. The complex signaling network governing cardiac remodeling	3
1.3.1. Overview of hypertrophic signaling in cardiomyocytes	3
1.3.2. The molecular basis for eccentric hypertrophy.....	4
1.3.3. Mechano-sensitive hypertrophic pathways.....	7
1.4. A systems biology approach to cardiac signaling	9
1.4.1. Network modeling	9
1.4.2. High-content automated image analysis	9
1.5. Conclusions.....	10
Chapter 2: Predictive model identifies key network regulators of cardiomyocyte mechano-signaling.....	12
2.1. Foreword.....	13
2.2. Introduction.....	13
2.3. Methods.....	14
2.3.1. Model construction	14
2.3.2. Model validation.....	16
2.3.3. Parameter robustness	16
2.3.4. Sensitivity analysis	17

2.4.	Results.....	17
2.4.1.	A predictive computational model of the cardiomyocyte mechano-signaling network.....	17
2.4.2.	Model validation and importance of reaction logic	22
2.4.3.	Identification of key network regulators.....	24
2.4.4.	Screen for combination mechano-therapies.....	29
2.5.	Discussion.....	31
2.5.1.	Cardiac mechano-signaling model.....	31
2.5.2.	Model validation	32
2.5.3.	Key hubs integrating mechano-signals	32
2.5.4.	Synergistic targets regulate stretch-induced hypertrophy and gene expression.....	33
2.5.5.	Limitations and future directions	34
2.5.6.	Conclusions.....	35
Chapter 3: Differential control of diverse cardiomyocyte hypertrophy phenotypes.....		36
3.1.	Foreword.....	37
3.2.	Introduction.....	37
3.3.	Methods.....	38
3.3.1.	Cell culture.....	38
3.3.2.	Quantifying changes in shape	39
3.3.3.	Quantifying changes in transcript abundance	40
3.3.4.	RPPA proteomics analysis.....	41
3.3.5.	Partial least squares regression	41
3.4.	Results.....	42
3.4.1.	Ligands differentially induce diverse protein signaling pathways.....	42
3.4.2.	PLSR clusters families of protein activity and links them to distinct morphologies	44
3.4.3.	MEK1, PI3K, and Src mediate Nrg-induced elongation	48
3.5.	Discussion.....	50
3.5.1.	Observed protein activity concurs with prior studies.....	50
3.5.2.	Regulation of Nrg-induced elongation by MEK1, PI3K, and Src	50
3.5.2.	Limitations and future directions	51
3.5.3.	Conclusions.....	52
Chapter 4: Novel drivers of cardiomyocyte remodeling from a genome-wide shRNA screen		53
4.1.	Foreword.....	54
4.2.	Introduction.....	54

4.3. Methods.....	55
4.3.1. Cell culture.....	55
4.3.2. Microscopy	56
4.3.3. Image processing	56
4.3.4. Filtering and normalization.....	58
4.3.5. Binomial model of off-target effects.....	58
4.3.6. Gene set enrichment.....	60
4.4. Results.....	61
4.4.1. Image processing algorithms identify distinct myocyte morphologies.....	61
4.4.2. Myocyte quantity and image correlation provide quality control metrics	61
4.4.3. Two-step normalization corrects plate-level variation and eliminates regional artifacts.....	63
4.4.4. Multiple shRNAs above threshold per gene are necessary to identify hits.....	68
4.4.5. Manual verification confirms identification of distinct hypertrophic morphologies	71
4.4.6. Enrichment analysis identifies overrepresented signaling pathways	75
4.5. Discussion	77
4.5.1. A genome-wide index of myocyte morphologies	77
4.5.2. Clinical significance of genes influencing myocyte remodeling	78
4.5.3. Advantages and shortcomings of segmentation-based image analysis.....	79
4.5.4. Principles for optimal design of phenotypic screens	80
4.5.5. Limitations and future directions	81
4.5.6. Conclusions.....	82
Chapter 5: Summary and outlook	83
5.1. Novel contributions.....	84
5.2. Future directions	84
5.3. Conclusions.....	86
Appendix A: Experimental parameters.....	88
Appendix B: Mechano-signaling network model	95
Appendix C: Mechano-signaling network model reactions.....	99
Appendix D: Validation relationships.....	105
Appendix E: Genes with multiple shRNAs above threshold for area.....	110
Appendix F: Genes with multiple shRNAs above threshold for elongation.....	113

Appendix G: Genes with multiple shRNAs above threshold for spikiness 117

References..... 120

List of figures and tables

Figure 0.1. Schematic of research plan.....	5
Figure 2.1. Reconstruction of the mechano-signaling network in cardiac myocytes	18
Figure 2.2. Simulated activation of the cardiac mechano-signaling network.....	20
Figure 2.3. Model predicts dynamics of hypertrophic outputs	21
Figure 2.4. Model predictions validate against experimental observations not used for model reconstruction.....	23
Figure 2.5. Network displays robustness to variation in model parameters	24
Figure 2.6. Model logic influences prediction accuracy.....	25
Figure 2.7. Network-wide sensitivity matrix.....	27
Figure 2.8. Sensitivity analysis reveals network structure	28
Figure 2.9. Network displays higher response to valsartan and sacubitril combined than individually	30
Figure 2.10. Model predicts higher efficacy of combined valsartan and sacubitril treatment.....	30
Figure 2.11. Model predicts efficacy of other combination mechano-therapies	31
Figure 3.1. Hypertrophic ligands induce diverse changes in protein expression and phosphorylation.....	43
Figure 3.2. Protein expression, gene expression, and morphological changes induced by four hypertrophic ligands	45
Figure 3.3. Individual signaling pathways correlate with distinct hypertrophic phenotypes	46
Figure 3.4. PLSR model provides descriptive but not predictive value	47
Figure 3.5. MEK1, PI3K, and Src mediate Nrg-induced elongation.....	49
Figure 4.1. Schematic of image processing algorithm for myocyte identification.....	62
Figure 4.2. Automated image analysis identifies myocytes and quantifies cell boundaries.....	63
Figure 4.3. Filtering by myocyte quantity and image noise removes conditions with abnormal cell health or imaging errors	64

Figure 4.4. Two-step normalization corrects for plate-level variation and eliminates regional artifacts.....	66
Figure 4.5. Two-step normalization stabilizes area values across screen.....	67
Figure 4.6. Two-step normalization stabilizes elongation values across screen	67
Figure 4.7. Two-step normalization stabilizes form factor values across screen	68
Figure 4.8. Significantly high numbers of genes have multiple shRNAs above threshold	70
Figure 4.9. Parameter fitting for off-target rate and pathway size in binomial model	71
Figure 4.10. Overlap between top genes for area, elongation, and spikiness	72
Figure 4.11. Hits identified display expected morphologies	73
Table 4.1. Cardiac function and disease are highly enriched in conditions with high area	75
Table 4.2. Cardiac function and disease are highly enriched in conditions with high area	76
Table 4.3. Cardiac function and disease are highly enriched in conditions with high area	76

Abbreviations

Abbreviation	Description
ACE	angiotensin-converting enzyme
Akt	protein kinase B
α -MHC	α -myosin heavy chain
Ang, Ang II	angiotensin II
ANP	atrial natriuretic peptide
Ao	angiotensinogen
ARB	angiotensin receptor blocker
ARVM	adult rat ventricular myocyte
AT1R	angiotensin type 1 receptor
β -MHC	β -myosin heavy chain
BNP	brain natriuretic peptide
cGMP	cyclic guanosine monophosphate
Ca ²⁺	calcium
CaMK	calmodulin kinase
CaN	calcineurin
cGMP	cyclic guanosine monophosphate
CREB	cAMP response element binding
CT-1	cardiotrophin-1
Cx43	connexin 43
DAG	diacylglycerol
DAPI	4',6-diamidino-2-phenylindole
Dysgl	dystroglycans
EC ₅₀	half-maximal effective concentration
EdU	5-ethynyl-2'-deoxyuridine
ET, ET-1	endothelin-1
ERK	extracellular signal-related kinase
ET1R	endothelin-1 receptor

Abbreviation	Description
FAK	focal adhesion kinase
FCS	fetal calf serum
FHL	four-and-a-half LIM domains protein
FoxO	Forkhead box O
G $\alpha_{q/11}$	G q/11 alpha subunit
GATA4	GATA-binding protein 4
gp130	glycoprotein 130
GSK3 β	Glycogen synthase kinase 3 β
IGF	insulin growth factor-1
JAK	Janus kinase
JNK	c-Jun N-terminal kinase
LDE	logic-based differential equation
LIF	leukemia inhibitory factor
LTCC	L-type calcium channel
MEK	MAPK/ERK kinase
mTOR	mechanistic target of rapamycin
n	Hill coefficient
NCX	sodium–calcium exchanger
NFAT	nuclear factor of activated T-cells
NHE	sodium–hydrogen exchanger
NOS	endothelial nitric oxide synthase
Nrg	neuregulin-1
NRVM	neonatal rat ventricular myocyte
p70S6K	70 kDa ribosomal protein S6 kinase 1
PCA	principal components analysis
PI3K	phosphatidyl inositol 3 kinase
PIP2	phosphatidylinositol 4,5-bisphosphate
PKC	protein kinase C
PKG	cGMP-dependent protein kinase
PLC	phospholipase C
PLSR	partial least squares regression
Raf1	Proto-oncogene c-Raf
Ras	rat sarcoma viral oncogene homolog

Abbreviation	Description
RhoA	Ras homolog gene family, member A
RMSE	root mean-squared errors
RPPA	reverse phase protein array
sACT	skeletal α -actin
SERCA	sarcoplasmic reticulum Ca^{2+} ATPase
sGC	soluble guanylyl cyclase
shRNA	short hairpin
Src	proto-oncogene c-Src
STAT	signal transducers and activators of transcription
τ	time constant
TRP	transient receptor potential channel
Y_{init}	initial node activation
Y_{max}	maximal node activation

Chapter 1

Background and significance

1.1. Foreword

Dozens of signaling pathways are implicated in heart failure, a costly and often fatal condition, but much remains unclear about how they regulate the growth and remodeling of cardiomyocytes. In this chapter, we discuss the increasing burden of heart failure and the need for targeted therapies that promote beneficial remodeling and myocardial recovery. We review existing knowledge of hypertrophic signaling pathways in cardiac myocytes, and consider the strengths and limitations of existing approaches to studying cellular remodeling. Finally, we summarize the most crucial areas where further work needs to be concentrated.

1.2. Introduction

Heart failure, a leading cause of death in developed societies, afflicts over 25 million people worldwide [1]. More than half of heart failure patients die within 5 years [2], and the annual burden in healthcare costs is over \$30 billion in the United States alone [3]. Triggered by many common stresses, heart failure usually involves dramatic growth of ventricular myocytes as the heart attempts to compensate for its increased burden. While hypertrophic remodeling can function as a beneficial compensatory response to extra workload, dramatic ventricular growth can ultimately engender cardiac deterioration [4].

Because normalization of ventricular size and shape typically accompanies myocardial recovery [5], [6], identifying pharmaceutical and device therapies that control and reverse hypertrophy is a high priority. Although anti-adrenergic strategies such as β -blockers have achieved clinical success, many patients become refractory to neurohormonal inhibition and continue to worsen, albeit more slowly [7]. Since ventricular remodeling can contribute independently to heart failure by increasing myocyte strain and thus stretch-induced hypertrophic signaling [8], mechanical interventions such as left ventricular assist devices (LVADs) can promote cardiac recovery by reducing wall stress [9]. Complications of surgery, such as bleeding or infection, may render device implantation less preferable for some patients,

however [10]. Given that maximally effective strategies will likely complement ventricular assistance with pharmacological therapy, continued drug development is essential [11], [12].

Recent success with combination drug therapies inhibiting multiple nodes in the hypertrophy signaling network underscores the need to understand the network as a whole, and not just target one individual pathway in isolation [13], [14]. Distinct forms of cardiac remodeling have been associated not only with different hemodynamic origins [15], but also with varying clinical outcomes. For example, eccentric hypertrophy, characterized by myocyte elongation and ventricular dilation, poses greater risks than concentric hypertrophy, characterized by ventricular thickening [16]. Although certain hypertrophic ligands have been correlated with different hypertrophic phenotypes [17], less is known about the unique roles of individual signaling pathways in modulating remodeling. Likewise, although researchers have discovered many mechano-sensors contributing to stretch-induced hypertrophy, the control structures integrating mechanical signals remain unclear [18], [19]. A better understanding of which signaling pathways drive distinct remodeling patterns would enable development of more targeted and personalized therapies for patients from a wide range of etiologies and genetic backgrounds.

1.3. The complex signaling network governing cardiac remodeling

1.3.1. Overview of hypertrophic signaling in cardiomyocytes

Initiation of cardiac hypertrophy falls into two general categories of neurohormonal and biomechanical mechanisms [4]. The former have been characterized more fully, while the latter will be discussed in section 1.3.3. Among the most important cytokines stimulating hypertrophy are epinephrine, norepinephrine, angiotensin II, endothelin-1, neuregulin, and insulin growth factor-1 [20]. Although a host of proteins are activated in response to these ligands, the most prominent pathways include the Ca^{2+} -calcineurin-NFAT cascade [21], the PI3K-Akt cascade [22], and the three major families of MAPK signaling: ERK1/2 [23], p38 [24], and JNK [25]. These pathways govern a host of transcription factors, which in turn control the expression of numerous cardiac genes. Of particular note in the context of

hemodynamic or metabolic is the downregulation of several post-natal genes and the prominence of several fetal genes, including important clinical markers such as ANP and BNP [26].

Previously, our lab has constructed a predictive model of the hypertrophic signaling cascades downstream of 14 receptors, identifying key network hubs [27]. The outputs of the model were limited to the members of the fetal cardiac gene program and a generic node for “cell area”, and did not reflect the full diversity of gene expression and morphological features. Subsequent work examined 15 receptor agonists largely corresponding to the 14 receptors mentioned above, and quantified their influence on a wider array of phenotypes including elongation, spikiness, fibrosis, inflammation, proliferation, and cell death, in addition to the fetal gene program [17]. However, this work did not characterize the role of individual signaling pathways in transmitting these signals. After connecting stimuli to pathways and stimuli to phenotypes, the missing link of connecting pathways to phenotype remains.

1.3.2. The molecular basis for eccentric hypertrophy

Pathological cardiac hypertrophy is often classified as concentric or eccentric [15]. Concentric hypertrophy, usually associated with pressure overload caused by hypertension or aortic stenosis, involves thickening of the ventricular walls and decreased chamber volume. Eccentric hypertrophy, associated with volume overload caused by conditions such as chronic myocardial infarction or dilated cardiomyopathy, involves dramatic increases in chamber volume. Among the cellular phenotypes mentioned above, myocyte elongation involving serial (as opposed to parallel) addition of sarcomeres stands out because of its contribution to eccentric hypertrophy [28]. Here we briefly review the several signaling pathways regulating elongation in the heart (Fig. 1.1).

Several cytokines promote elongation through the gp130 receptor, which activates both the JAK/STAT and the MEK5/ERK5 pathways [29]. LIF strongly induced elongation in cultured myocytes, an effect that was abrogated in cells with dominant-negative MEK5 [30]. The same study produced severe dilated cardiomyopathy in transgenic mice overexpressing activated MEK5. LIF-induced elongation

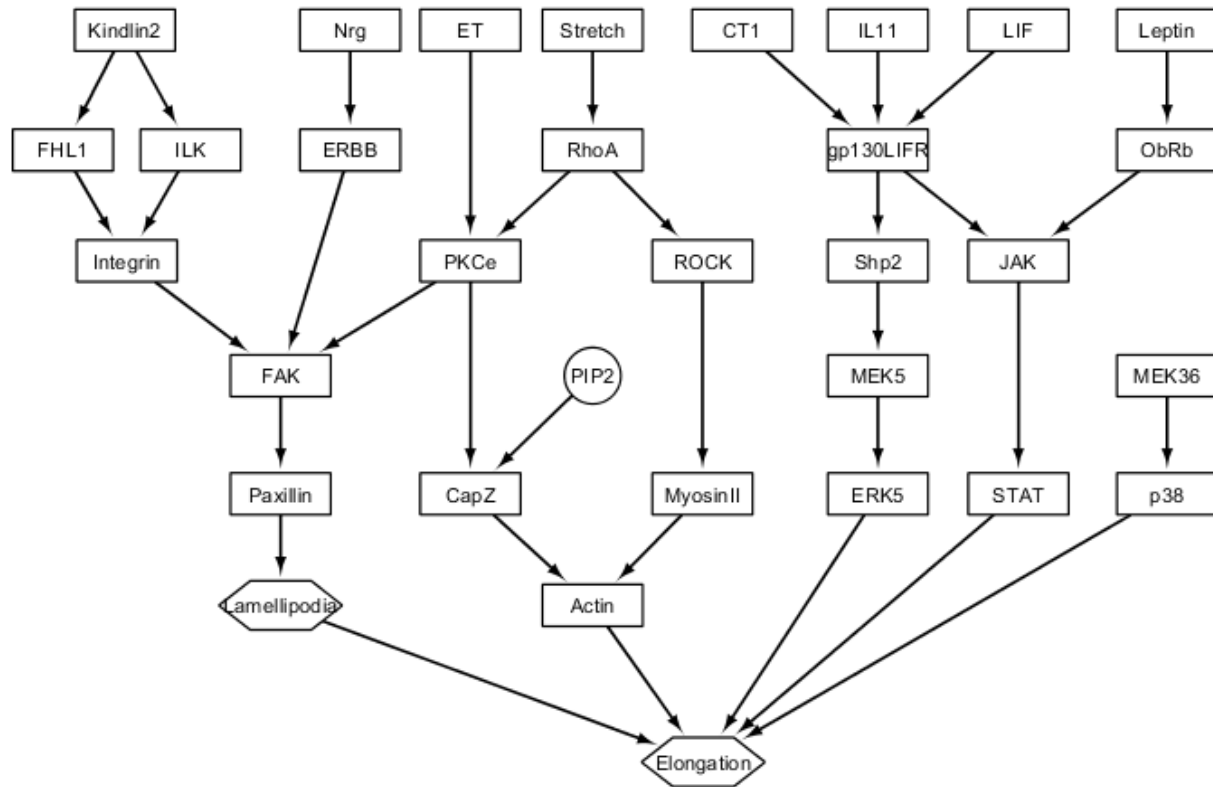


Figure 1.1. Signaling pathways regulating elongation in cardiac myocytes. The model depicted was reconstructed from prior studies in the literature.

through gp130 was later additionally shown to be dependent on SHP2, which binds with Gab1 downstream of gp130 and is necessary for ERK5 activation [31]. Elsewhere, IL-11, another cytokine binding to gp130, activated STAT3 and lengthened myocytes, while also exhibiting cardioprotective effects against ischemia [32]. In like fashion, CT-1-induced myocyte lengthening through gp130 in adult cardiomyocytes requires STAT3 and MEK5 participation; paradoxically, CT-1 overexpression was correlated with myocyte widening in spontaneously hypertensive rats [33]. Leptin is an adipocyte-derived peptide that signals through the Ob-Rb receptor, which is similar to gp130. Interestingly, leptin also induced STAT3 phosphorylation, myocyte elongation, and eccentric left ventricular dilation, an effect that was inhibited by blocking JAK2 [34].

The Src/FAK pathway is also important to lengthening myocytes. Nrg stimulation induced lamellipodium formation, elongation, and synchronous beating in myocytes, effects that were prevented by a Src inhibitor or by an antibody to erbB2 [35]. There, the extension of lamellipodia appeared to be dependent on formation of a complex between erbB2, FAK, p130^{CAS}, and paxillin. One possibly related mechanism for control of myocyte lengthening by FAK and paxillin is regulation of actin capping by CapZ through the mediation of Rho, PKC ϵ , and PIP2 [36], [37]. The role of Rho in elongation remains controversial. Its role in promoting elongation during development and cytokinesis, particularly through activation of myosin II, is well established [38], [39]. However, some have observed both RhoA and Rac1 to be uninvolved in sarcomere assembly in series [40], while others claim that RhoA actually inhibits elongation [31].

Several other miscellaneous signaling molecules have been implicated in influencing myocyte elongation. C2C12 cells lacking kindlin-2, an integrin-associated protein required for muscle development, were unable to elongate or fuse into myotubes [41]. Overexpression of FHL1, another integrin-binding protein, induced hyperelongation in C2C12 cells; this process specifically depended on $\alpha_5\beta_1$ - but not the $\alpha_4\beta_1$ -integrins [42]. Transgenic Cdk8 overexpression resulted in myocyte lengthening and progressive dilated cardiomyopathy in mice [43]. In neonatal rat cardiomyocytes, electrical field stimulation promoted myocyte reorientation and elongation; this response displayed complete dependence on actin polymerization and partial dependence on PI3K activity [44]. Constitutively active MEK3b resulted in elongation and higher sarcomere organization within hESC cardiomyocytes, suggesting a role for p38 [45]. Finally, in contrast to the pro-elongation pathways discussed here, ERK1/2 signaling promotes width increases in myocytes, and myocytes from mouse hearts lacking ERK1/2 demonstrated eccentric growth [46]. It seems unlikely that all these pathways are operating independently; although much overlap and crosstalk likely exists, more work is necessary to determine the overall structure of this network. Furthermore, many of the mechanisms by which these pathways ultimately prompt serial addition of sarcomeres remains unclear.

1.3.3. Mechano-sensitive hypertrophic pathways

Myocyte lengthening and thickening is driven not only by neurohormonal stimulation, but also by increased hemodynamic load [47], [48]. Myocyte growth drives changes in overall ventricular chamber geometry, which can in turn exacerbate the mechanical burden on the heart [8]. Although cells possess myriad mechanisms for sensing mechanical stress [49], cardiomyocytes detect pressure or volume overload primarily through three major groups of mechano-sensors: calcium channels, cytoskeletal proteins, and the angiotensin type 1 receptor (AT1R) [50], [51].

AT1R was one of the first molecules implicated in cardiac mechano-signaling [52], [53]. In response to stretch, AT1R increases MAPK phosphorylation [54], [55], JAK–STAT signaling [56], [57], and expression of several hypertrophic markers [52], [58]. Not until much later, however, was AT1R proved to be directly stretch-sensitive apart from the involvement of angiotensin II (Ang II) [59]. Subsequent studies showed that stretch-induced AT1R signaling depends on β -arrestin [60], [61], and pinpointed the specific amino residues responsible for activation of the receptor [62]. Interestingly, β -arrestin activity in coordination with AT1R was subsequently shown to mediate the Frank–Starling mechanism of cardiac contractility [63]. Although myocytes do release Ang II in response to stretch [52]–[54], [58], [64], [65], both the mechanism behind Ang II release and its specific effect on myocyte remodeling remain unclear [19]. Nonetheless, the importance of AT1R in cardiomyocyte mechano-sensing is firmly established, especially given the prevalence of AT1R blockers for treating cardiovascular disease [66].

Intracellular calcium release was reported in several of the earliest studies stretching myocytes [67]–[69], but it has taken many years to identify the channels responsible. Among the ion channels claimed to be stretch-sensitive, the L-type calcium channel (LTCC) [32], [70]–[75] and members of the transient receptor potential (TRP) channel family [76]–[80] have the most support. As is the case with AT1R activation, calcium release triggers the upregulation of a wide range of hypertrophic factors [74], [81]. Many of these calcium-dependent effects are mediated by the calcineurin–NFAT pathway [82]–[84]. Importantly, the mechano-sensing ability of cardiac ion channels has electrophysiological as well as

hypertrophic significance [85]. As further studies clarify the role of LTCC and TRP channels in the heart, their pharmacological significance will continue to increase [86], [87].

The third major group of mechano-sensors, cytoskeletal proteins, was initially popularized through the tensegrity model of the cytoskeleton [88]. Whether or not this model is helpful in understanding cell mechanics, several cytoskeletal structures are crucial to enabling myocytes to modify their architecture and initiate signaling in response to mechanical forces [89]. Two important proteins propagating signals from the extracellular matrix to the cell interior are integrin and dystroglycan. Exerting tension on integrins not only causes overall deformation of the cell [88], but also induces activation of proteins such as FAK, Src, and RhoA [90], [91]. Dystroglycan, a membrane protein binding to laminin, connects internally to dystrophin, which links to the actin cytoskeleton [92]. Disruption of the dystrophin–dystroglycan complex, a hallmark of Duchenne muscular dystrophy, impairs the ability of the cardiomyocyte to produce NO and to reduce myocyte slippage in response to stretch [93], [94].

In light of the abundant literature detailing protein activation and gene expression in response to stretch, surprisingly little is known about other stretch-induced phenotypes in cardiomyocytes, such as cell orientation and elongation. Although it is agreed that cardiomyocytes realign in response to uniaxial stretch, some have found them to orient parallel to the stretch direction [95], while others have found them to orient transverse to the stretch direction [80], [96]. This discrepancy does not seem to be discussed in any of the relevant literature. Furthermore, almost no studies have examined the differences between stretching in a uniaxial versus a biaxial direction. One study in diaphragm muscle reported that longitudinal stress differentially activates PI3K, PKC, and MEK1/2, whereas cyclic AMP–dependent PKA was activated only in response to transverse stress [97]. In another study in NRVMs, transverse stress induced greater levels of FAK and ERK phosphorylation than longitudinal stress [98]. This same study reported that FAK and ERK phosphorylation increased with higher frequencies of cyclic stretch, but beyond this little is known about the difference between static and cyclic stretch, or between different patterns of cyclic stretch. Other areas deserving further attention are the role of feedback loops in the

mechano-signaling network, and the function of paracrine signaling between cardiac fibroblasts and myocytes [99]–[102].

1.4. A systems biology approach to cardiac signaling

1.4.1. Network modeling

By complementing data generation with engineering tools, such as predictive modeling and quantitative analysis, systems biologists can penetrate large-scale datasets with greater insight [103]. For example, computational models help reveal mechanisms regulating complex signaling networks by synthesizing large bodies of experimental data into a quantitative, predictive framework [104]. In the case of the cardiac hypertrophy signaling network, a logic-based differential equation (LDE) modeling approach [105] successfully interrogated a network whose size rendered kinetic models infeasible, identifying key hubs and global functional relationships [27]. The insights afforded into the distinct roles of various hypertrophic signaling pathways, however, has been limited by gaps in the experimental literature on which previous models have been based. In order to reconstruct pathways differentially controlling remodeling outcomes, approaches need to be developed that can incorporate a wide range of proteomic and phenotypic metrics and that can quantitatively compare the roles of multiple hypertrophic signaling hubs.

1.4.2. High-content automated image analysis

As robotic cell culture and automated microscopy systems improve, it is often difficult for researchers to keep pace with the wealth of data such technologies generate. In order to translate the massive influx of experimental outputs into actual mechanistic insights, novel methods for image analysis are increasingly vital [106]. Previous studies have developed innovative image processing algorithms to reveal distinct morphological signatures and to discriminate between levels of sarcomere organization [17], [107], but such techniques have not yet been used to study myocyte growth and remodeling on a large scale.

Unlike analysis of smaller image collections, for which algorithms can be manually adjusted for individual batches of images, processing millions of images at a time requires a highly generalizable segmentation and sorting strategy. In addition, the unavoidable variation in cell health and staining and image quality across large screens requires development of new protocols for background subtraction and data normalization. To successfully perform unbiased phenotypic screens on cardiomyocytes at a genome-wide scale, it will be necessary to combine advanced image processing algorithms with innovative normalization techniques.

1.5. Conclusions

Ventricular remodeling plays a critical role as an independent driver of heart failure. Given the complexity of the molecular signaling networks driving remodeling, modeling has become an essential tool for synthesizing large data sets and indicating optimal directions for further experimentation. Recent computational models have identified context-dependent roles of network hubs, determined relationships between network structure and function, and screened for optimal drug therapies. In the future, data-driven modeling approaches will remain crucial for revealing novel signaling mechanisms and for generating testable predictions of how myocytes control growth and remodeling. In this work, we integrate such modeling and experimental methods to identify the control structures and pathways underlying cardiomyocyte growth and remodeling.

In the first aim (chapter 2), we focus on mechanically-induced myocyte remodeling. By constructing, validating, and analyzing the first computational model of the cardiac mechano-signaling network, we locate the control structures governing the hypertrophic response and identify patterns of crosstalk between the several mechano-sensitive pathways operating in parallel. In addition, we use the model to predict drug targets for development of combination therapies. Our second aim (chapter 3) then expands the focus from a single stimulus (stretch) to multiple stimuli, investigating how multiple pathways differentially regulate distinct hypertrophic phenotypes such as area, elongation, and fetal gene

expression. In order to identify and validate targets that uniquely govern variant remodeling outcomes, we combine high-content imaging, RPPA, and gene expression in a data-driven modeling framework. Finally, in the third aim (chapter 4), we expand the focus still further to the entire genome in order to identify drivers of myocyte growth and remodeling that have not been previously implicated. We develop a complete workflow for automated cell segmentation, morphological measurement, normalization, statistical validation, and pathway enrichment of an shRNA screen encompassing 97,500 conditions. Using this workflow, we discover hundreds of candidate genes regulating area, elongation, and spikiness in cardiomyocytes. Together, these aims accomplish three goals: Identification of signaling pathways driving variant myocyte phenotypes; discovery of new biochemical targets for modulating cardiac remodeling; and development of innovative image processing algorithms for assessing myocyte form and function.

Chapter 2

Predictive model identifies key network regulators of cardiomyocyte mechano-signaling

The work in this chapter is adapted from P. M. Tan, K. S. Buchholz, J. H. Omens, A. D. McCulloch, and J. J. Saucerman, “Systems analysis identifies key network regulators of cardiomyocyte mechano-signaling,” *PLoS Comput. Biol.*, vol. 13, no. 11, p. e1005854, Nov. 2017.

Author contributions: P. M. Tan—conceptualization, computational modeling, paper writing. K. S. Buchholz—computational modeling, paper editing. J. H. Omens—funding acquisition, supervision, paper editing. A. D. McCulloch—conceptualization, funding acquisition, supervision, paper editing. J. J. Saucerman—conceptualization, funding acquisition, supervision, paper editing.

2.1. Foreword

In chapter 1, we considered the diverse array of stimuli contributing to cardiac hypertrophy and remodeling. We now restrict our scope to consider remodeling signals caused by a single stimulus, mechanical stretch. While a plethora of mechano-sensitive proteins have been discovered in cardiomyocytes, the mechanisms whereby the downstream signaling cascades are integrated into the cell's hypertrophic response remain unknown. In this chapter, we reconstruct cardiac mechano-signaling pathways in a computational model that identifies top network hubs and predicts effective combination mechano-therapies controlling remodeling.

2.2. Introduction

Cardiac mechano-signaling, the ability of the heart to sense and respond to mechanical cues, plays an integral role in driving ventricular hypertrophy and remodeling [108], [109]. Although hypertrophic remodeling initially functions as a compensatory response to extra workload, the dramatic growth of the ventricles ultimately engenders further cardiac deterioration [4]. Current therapies such as beta blockers and angiotensin II receptor blockers (ARBs) seek to block the chemical ligands initiating hypertrophy in addition to their direct hemodynamic effects [7]. As heart failure worsens, however, many patients become refractory to neurohormonal inhibition, and increased mechanical stretch of the myocytes can stimulate cardiac remodeling independently of the patient's biochemical status [8], [110]. Abnormal ventricular geometry in turn increases the mechanical burden, further heightening wall stress. A better understanding of cardiac mechano-signaling is crucial for identifying therapies that can interrupt this downward spiral [111].

While many mechano-sensitive proteins have been identified in cardiomyocytes [59], [76], the mechanisms whereby the downstream signaling cascades are integrated into the hypertrophic response remain unknown [18], [19]. Computational models can accelerate insight into complex signaling networks [104], and influential network hubs have previously been identified using logic-based models of

biochemically-initiated hypertrophy signaling [27], [112]. Past studies of mechano-sensing have used finite element or force dipole models to predict concentric or eccentric cardiac growth [113], to identify the mechanisms coordinating beating between adjacent myocytes [114], [115], and to gain insights into force transmission between contracting cells [116]. Others have developed mass-action kinetic models of individual stretch-sensitive pathways to study calcium dynamics [117], or to study TGF- β release in response to substrate stiffness [118]. These approaches, however, have not been used to examine systems-level properties of the signaling network itself.

In this study, we constructed and validated the first computational model of the cardiac mechano-signaling network in order to predict key signaling regulators integrating the stretch-induced hypertrophic response. Synthesizing the current understanding of mechanically driven signaling cascades, the model identifies signaling motifs and crosstalk logic crucial to network function. In particular, coordination between AT1R, integrins, and calcium channels was found to be essential for increased cell size, protein synthesis, and upregulation of the fetal gene program in response to mechanical stress. Rather than converging on a common set of nodes, each mechano-responsive pathway contributes to the cellular response through a distinct group of transcription factors. The model also elucidates cGMP-dependent cooperative mechanisms underlying valsartan/sacubitril, the combination angiotensin receptor–neprilysin inhibitor recently approved for treating heart failure. Combined responses to inhibition or activation of every pair of nodes in the network are then calculated, predicting additional combinations of drug targets with maximal influence over stretch-induced remodeling.

2.3. Methods

2.3.1. Model construction

A predictive computational model of the mechano-signaling network in cardiac myocytes was manually reconstructed from experimental studies described in published literature. To reconstruct the cardiomyocyte mechano-signaling network, experimental observations were synthesized from over 170

peer-reviewed papers. The literature search began by identifying papers that indicated a role for certain proteins in cardiac mechanotransduction, whether in the context of *in vivo* pressure overload or *in vitro* cardiomyocyte stretching. Individual reactions between mechano-responsive proteins were then included if other papers could be found (not necessarily in a mechanotransduction context) confirming a direct molecular interaction between them. During literature review, all papers involving *in vitro* cell-stretching experiments performed in rat cardiomyocytes were set aside for validation. Primary mechano-sensors were included only if evidence from at least three separate studies existed in which either that particular mechano-sensor alone was stretched, or if the mechano-sensor was reconstituted in a cell type previously unresponsive to stretch. Other nodes were only included if identified as mechano-responsive, or if necessarily inferred between other nodes. Outputs were selected for frequency of measurement across the literature and relevance to cardiac function. The full database of literature used in model construction or validation is provided in Appendix A.

Signaling dynamics were predicted with a logic-based differential equation (LDE) approach, in which activation of one node by another is modeled using a normalized Hill function. Logical AND or OR operations were used to represent pathway crosstalk, using the equation $f(x)f(y)$ for AND gating and $f(x) + f(y) - f(x)f(y)$ for OR gating [105]. In general, OR gating is used when each input to a node is sufficient but not necessary for activation, whereas AND gating is used when each input is necessary. Default reaction parameters included Hill coefficient $n = 1.4$ and half-maximal effective concentration $EC_{50} = 0.5$. Default node parameters included initial activation $Y_{init} = 0$, maximal activation $Y_{max} = 1$, and time constant $\tau = 1$. Logic decisions were primarily made using known biochemical mechanisms, but sometimes inferred from comparing experiments in the literature. The system of LDEs was generated in Netflux (available at <https://github.com/saucermanlab/Netflux>) and implemented in MATLAB. The input value of 0.7 weight and the weight $w = 0.9$ for other nodes was chosen to maximize the number of nodes activated between 50 and 95%, thus preventing undersaturation or oversaturation in

order to obtain the most information from the sensitivity analysis. The full databases of model species and reactions are provided in Appendices B and C, respectively.

2.3.2. Model validation

Qualitative activity changes of network nodes were predicted by simulating the response to stretch alone or to stretch together with inhibition of various nodes, and then comparing with published experimental observations of *in vitro* rat cardiomyocytes. Observations used for validation were exclusively from literature not used for model construction and only included mechano-signaling experiments performed in rat cardiomyocytes (mostly neonatal ventricular myocytes, with a few studies using adult ventricular or neonatal atrial myocytes). Input-output and input-intermediate activity changes were defined relative to no stretch, while inhibition activity changes were defined relative to steady-state stretch. Observations were encoded as increase, decrease, or no change and were compared with model predictions using a threshold of 5% absolute change, a more robust threshold than that used in previous studies[27], [112]. The full database of validation relationships is provided in Appendix D.

2.3.3. Parameter robustness

Network robustness to variation in model parameters was tested, using a validation threshold of 5% absolute change. For each parameter shown (\mathbf{Y}_{\max} , \mathbf{w} , \mathbf{n} , and \mathbf{EC}_{50}), new values for every instance of that parameter were generated by sampling from a uniform random distribution with indicated half-width about the original parameter value. 100 new parameter sets were created for each distribution range for each parameter, and simulations were run to compare model predictions with literature observations. No changes in validation accuracy resulted from varying τ or \mathbf{Y}_{init} . Robustness to simultaneous changes in overall reaction weight and weight of initial stretch input were also simulated across the ranges shown.

2.3.4. Sensitivity analysis

Sensitivity analysis was performed with knockdown simulations run in MATLAB by setting each Y_{\max} to 50% of the default value and measuring the resulting change in activity of every other node compared to steady state activation. Included in the top 12 most influential nodes are the 9 with the highest influence over the transcription factors (Akt, AT1R, Ca^{2+} , $G\alpha_{q/11}$, JAK, PDK1, PI3K, Raf1, and Ras) and the 9 with the highest influence over the outputs (α -actinin, actin, Akt, AP1, Ca^{2+} , calmodulin, PDK1, PI3K, and Ras). Hierarchical clustering of this subset of the sensitivity matrix (columns with 12 most influential nodes versus rows with transcription factors and outputs) was performed in MATLAB using Euclidean distance metrics and the unweighted average distance algorithm using a distance criterion of 0.3 to separate clusters. The topologically highest node from each cluster was identified, and grouping of transcription factors was performed by hierarchical clustering of the subset of the sensitivity matrix comprising columns with the 12 most influential nodes and rows with the transcription factors, using the same settings as before.

Double sensitivity analysis was run by measuring the network response to all pairwise combinations of decreasing or increasing Y_{\max} by 50% of its original value. Additional effects of pairs of nodes were measured by subtracting the higher sensitivity value due to decrease (or increase) of either node individually from the sensitivity due to decrease (or increase) of both nodes simultaneously.

2.4. Results

2.4.1. A predictive computational model of the cardiomyocyte mechano-signaling network

To reconstruct the cardiomyocyte mechano-signaling network (Fig. 2.1), experimental observations were collected from published literature. During literature review, papers involving *in vitro* cell stretching experiments performed in rat cardiomyocytes were set aside for validation, while remaining papers were used to reconstruct the signaling network. In all, a group of 172 papers designated

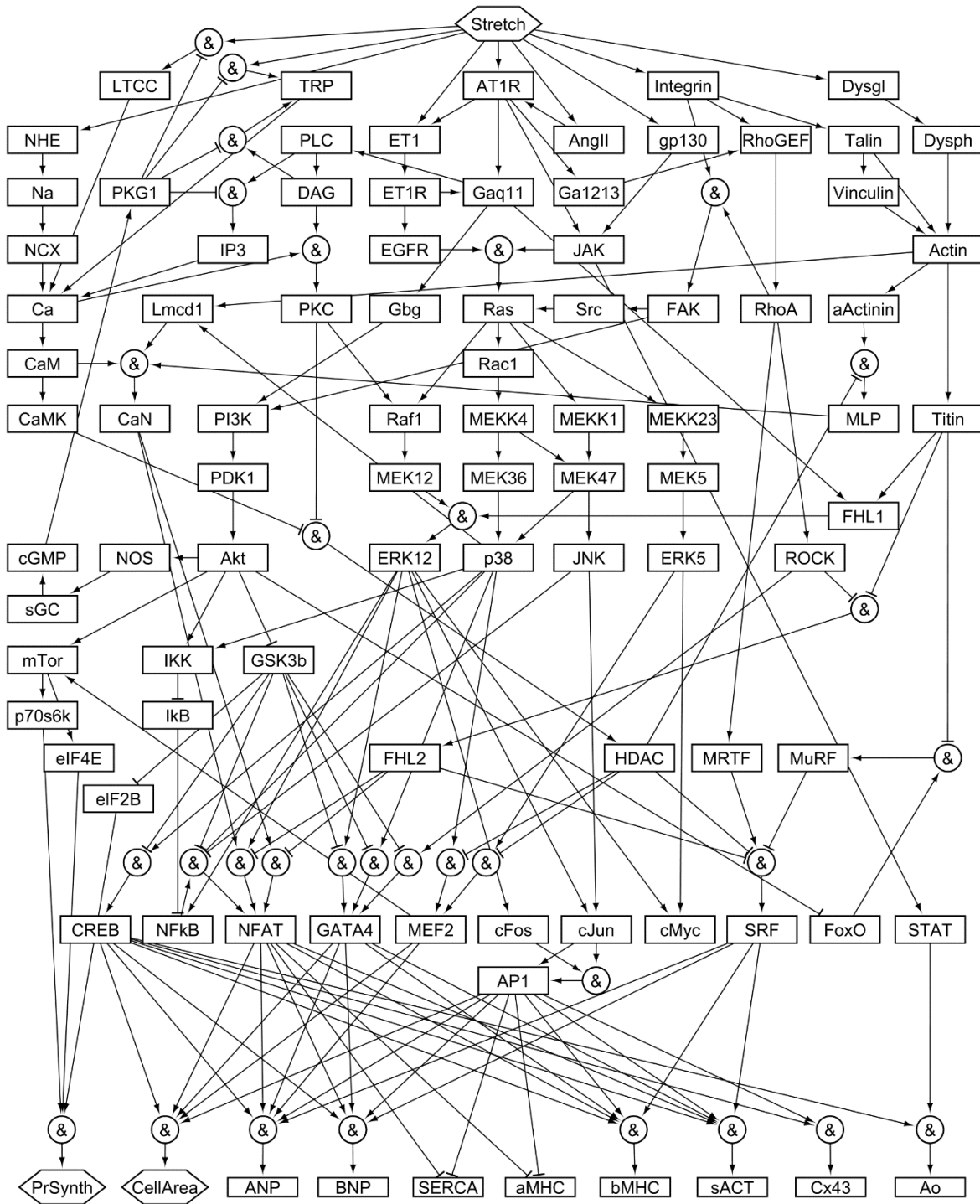


Figure 2.1. Reconstruction of the mechano-signaling network in cardiac myocytes. The model comprises 125 activating or inhibitory reactions linking 94 nodes, beginning with 9 mechano-sensors (NHE, LTCC, TRP, ET1, AT1R, AngII, gp130, Integrin, and Dysgl) and proceeding through multiple signaling cascades and transcription factors (penultimate row) to 10 hypertrophy-related gene products or phenotypes (final row). Complete lists of model reactions and of abbreviations for node names are provided in Appendices B and C.

for model construction was used to define network architecture (Appendices B and C), and a separate group of 55 papers designated for model validation was used to validate model predictions of network activity (Appendix D), an approach used in previous network reconstructions [27], [112].

The network incorporates five mechano-sensors each shown to be directly responsive to physical stretch: AT1R (angiotensin type 1 receptor) [59], LTCC (L-type calcium channel) [70], TRP (transient receptor potential channel) [77], integrin [119], and dystroglycan [120]. Also represented are four proteins known to be mechano-responsive, but whose mechanism of stretch-induced activation or release is unknown or disputed: gp130 (glycoprotein 130) [57], NHE (sodium–hydrogen exchanger) [121], Ang II (angiotensin II) [52], and ET-1 (endothelin 1) [122]. Signal propagation continues through downstream mechano-responsive proteins known to be regulated by these mechano-sensors, such as MAPKs (mitogen-activated protein kinases), Akt (protein kinase B), CaN (calcineurin), and FAK (focal adhesion kinase). These proteins in turn activate various transcription factors regulating the 10 phenotypic outputs most commonly reported in the literature, including protein synthesis, cell area, and expression of eight genes: ANP (atrial natriuretic peptide), BNP (brain natriuretic peptide), SERCA (sarcoplasmic reticulum Ca^{2+} ATPase), α -MHC (α -myosin heavy chain), β -MHC (β -myosin heavy chain), sACT (skeletal α -actin), Cx43 (connexin 43), and Ao (angiotensinogen). Activation of the fetal gene program, a hallmark of cardiac stress, encompasses upregulation of ANP, BNP, β -MHC, and sACT, and downregulation of SERCA and α -MHC [123]. In all, the reconstructed network of cardiomyocyte mechano-signaling includes 94 nodes (cytokines, proteins, mRNA, and cell processes), connected by 125 reactions. Further details of network reconstruction are included in the methods.

To convert the network into a predictive computational tool, we modeled reactions with logic-based differential equations (LDEs), a strategy previously used to combine the strengths of mass action kinetic and Boolean models for large-scale networks [105], [27], [112]. In this approach, the normalized activation of each node (such as phosphorylation for proteins, or expression for mRNAs) is represented by ordinary differential equations with saturating Hill functions, and continuous logical AND or OR logic

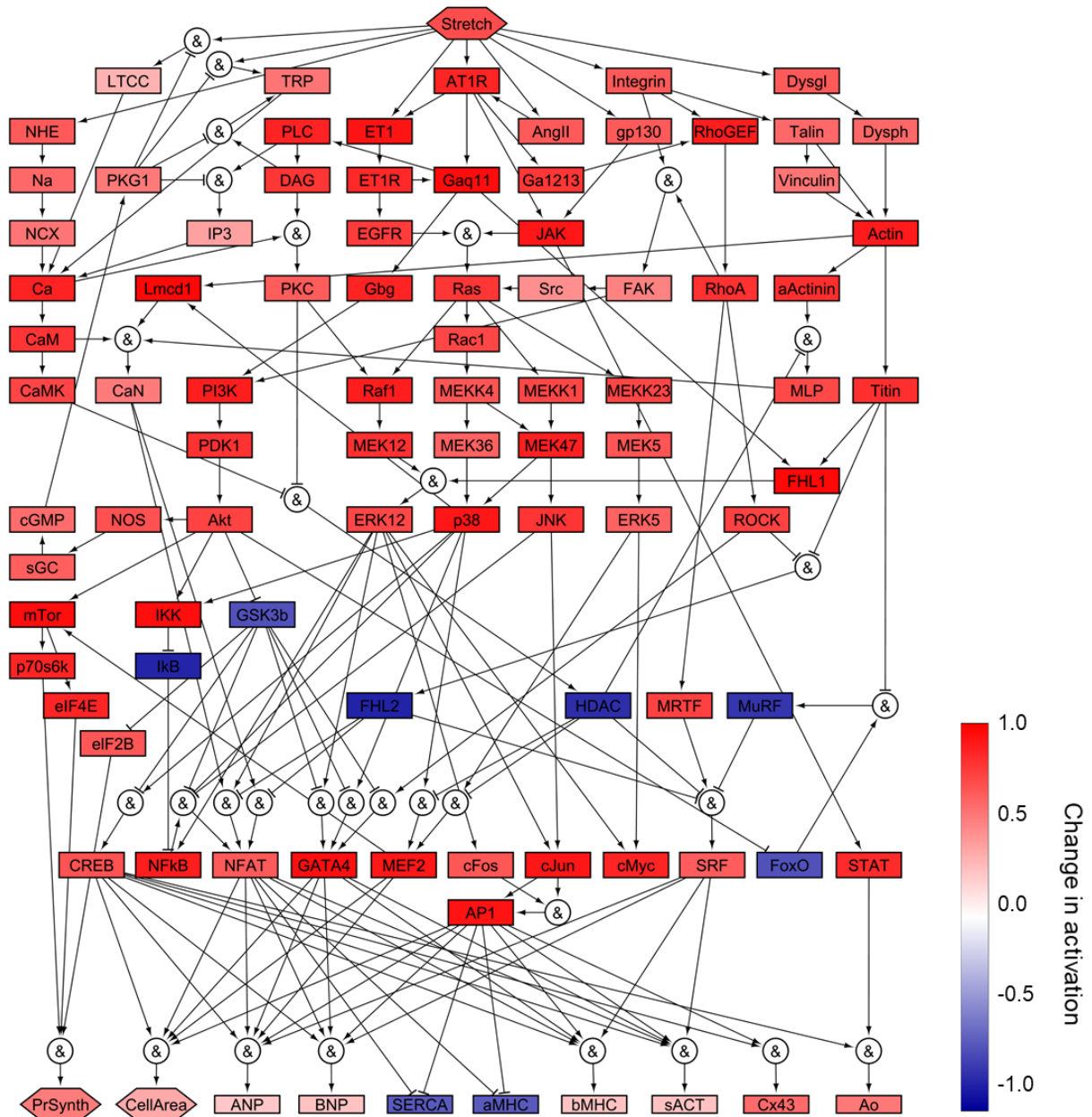


Figure 2.2. Simulated activation of the cardiac mechano-signaling network. The steady-state response to a stretch input of 0.7 is displayed.

gates are used to represent pathway crosstalk. In general, OR gating is used when each input to a node is sufficient but not necessary for activation, whereas AND gating is used when each input is necessary. As in previously published models [27], [105], [112], uniform default values were used for all network parameters. Preservation of network predictions to these constraints has been previously demonstrated

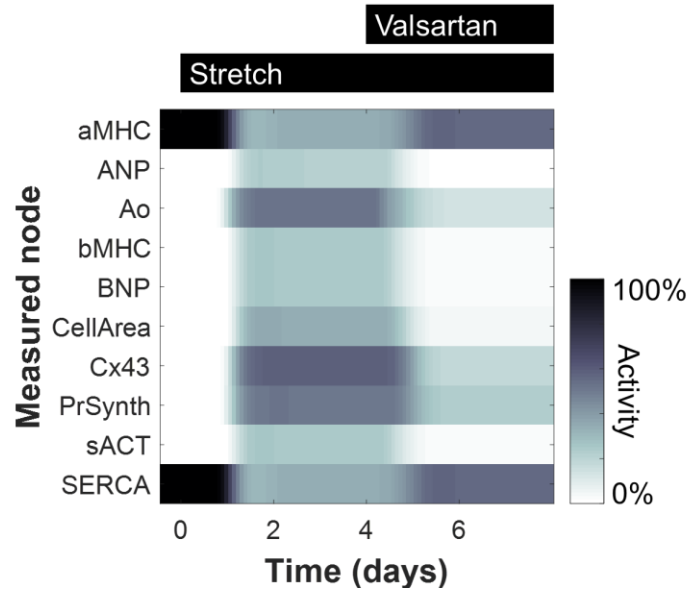


Figure 2.3. Model predicts dynamics of hypertrophic outputs. Gene expression and phenotype levels are shown for 10 model outputs in response in response to cell stretching (starting at 20 min.) and valsartan (starting at 4 hrs.).

[27], [112], [124], although individual parameters can be tuned when necessary by fitting to experimental measurements [125].

Based on the network structure in Appendix A, the system of LDEs was automatically generated in Netflux and implemented in MATLAB, as detailed in the Methods. A baseline condition of no external stretch is simulated by setting the stretch input at zero, and the response of the network to a high level of stretch can be predicted by increasing the input to 0.7, corresponding to applying approximately a 20% strain to myocytes cultured on a flexible membrane (Fig. 2.2). In addition, the model can predict the effects on stretch-induced signaling caused by adding an inhibitor against any node in the network. For example, stretch-induced increases in BNP, cell area, and other model outputs are predicted to be partially reduced with the AT1R antagonist valsartan (Fig. 2.3), consistent with previously published results [64], [126], [127].

2.4.2. Model validation and importance of reaction logic

To assess the accuracy of model predictions, we simulated activity changes of network nodes in response to stretch alone or to stretch together with inhibition of various nodes, and then compared them with published experimental observations of *in vitro* rat cardiomyocytes. Observations used for validation (Appendix D) included only mechano-signaling experiments performed in rat cardiomyocytes, and were gathered exclusively from literature not used for model construction. Simulated input-output and input-intermediate activity changes were defined relative to no stretch, while inhibition activity changes were defined relative to steady-state stretch. After encoding observations from literature as increase, decrease, or no change, they were compared with model predictions using a 5% threshold for defining change, a more stringent threshold than that of previously published network validations [27], [112]. Overall, the model correctly predicts 78% (134/172) of observations from papers not used to construct the model, including 100% (9/9) of input–output predictions, 100% (43/43) of input–intermediate predictions, and 68% (82/120) of inhibition predictions (Fig. 2.4, Appendix D).

To evaluate model robustness to variations in parameters, simulations were tested against parameter sets sampled from uniform random distributions. Consistent with studies of other networks [112], [124], validation accuracy is highly robust (>70%) to variation in model parameters over a uniform random distribution of up to $\pm 20\%$ for Y_{\max} , and up to $\pm 30\%$ or more for all other parameters (Fig. 2.5). In addition, validation accuracy remains high (>70%) with up to $\pm 30\%$ changes in baseline input levels (Fig. 2.6).

We also examined whether correct reaction logic is necessary for model accuracy. For example, AND logic was used to model the reaction for BNP, since multiple transcription factors are each necessary (though not individually sufficient) to drive gene expression [128]. In a variation of the model identical to the original but without AND gates (all logic gates set to OR), validation accuracy drops to 51% at the original reaction weight and input levels. Even with reduced reaction weights, the version

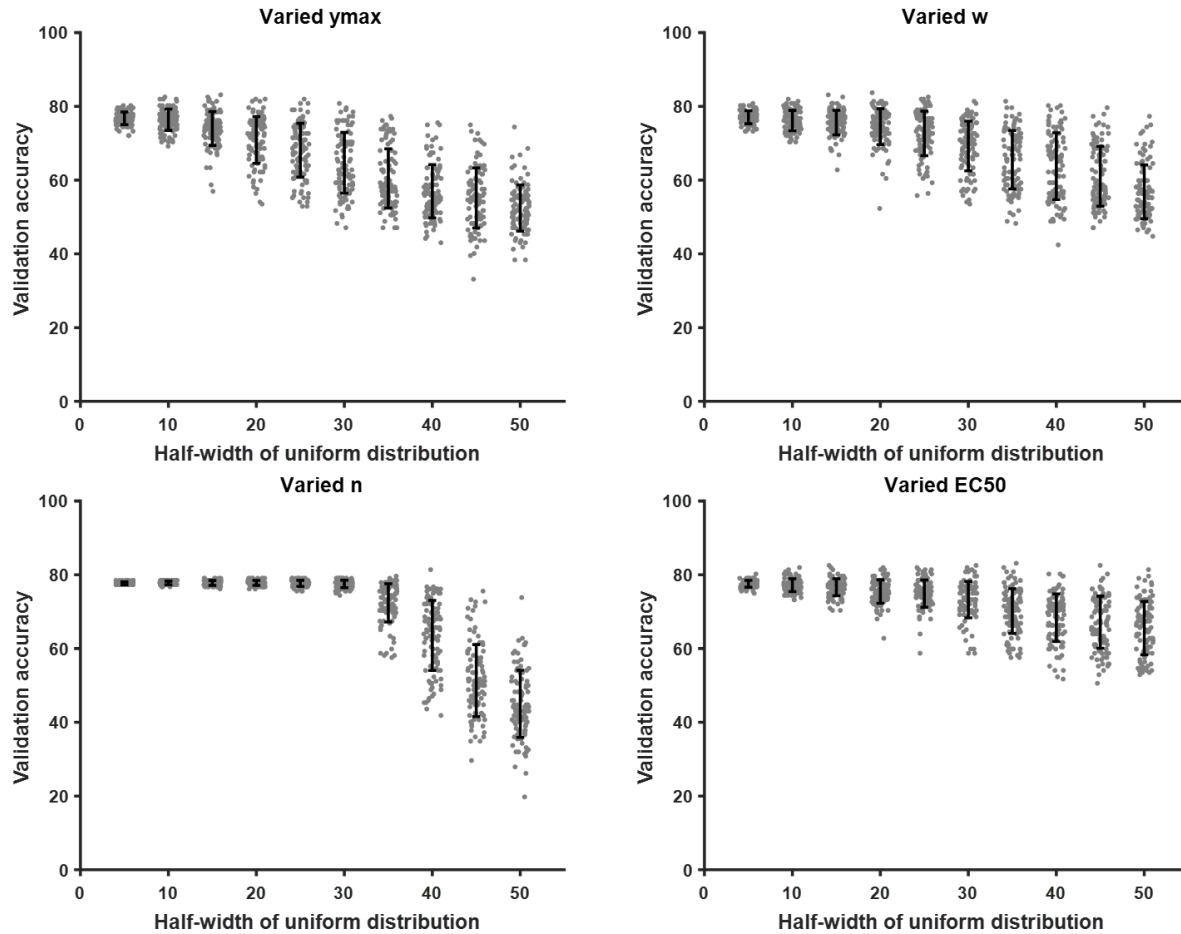


Figure 2.5. Network displays robustness to variation in model parameters. 100 new parameter sets were created for each distribution range for each parameter, and simulations were run to compare model predictions with literature observations, using a validation threshold of 5% absolute change. For each parameter tested (Y_{max} , w , n , and EC_{50}), new values for every instance of that parameter were generated by sampling from a uniform random distribution with indicated half-width about the original parameter value. (No changes in validation accuracy occurred in response to varying τ or y_0 .)

2.4.3. Identification of key network regulators

After validating the model's predictive capability, we performed a network-wide sensitivity analysis in order to determine quantitative functional relationships across the network. We hypothesized that the structure of the resulting sensitivity matrix would enable identification of key hubs regulating transcriptional activity. Knockdown of individual nodes was simulated by reducing Y_{max} for that node, and the resulting change in activity of every other node was measured, thus predicting the response of the

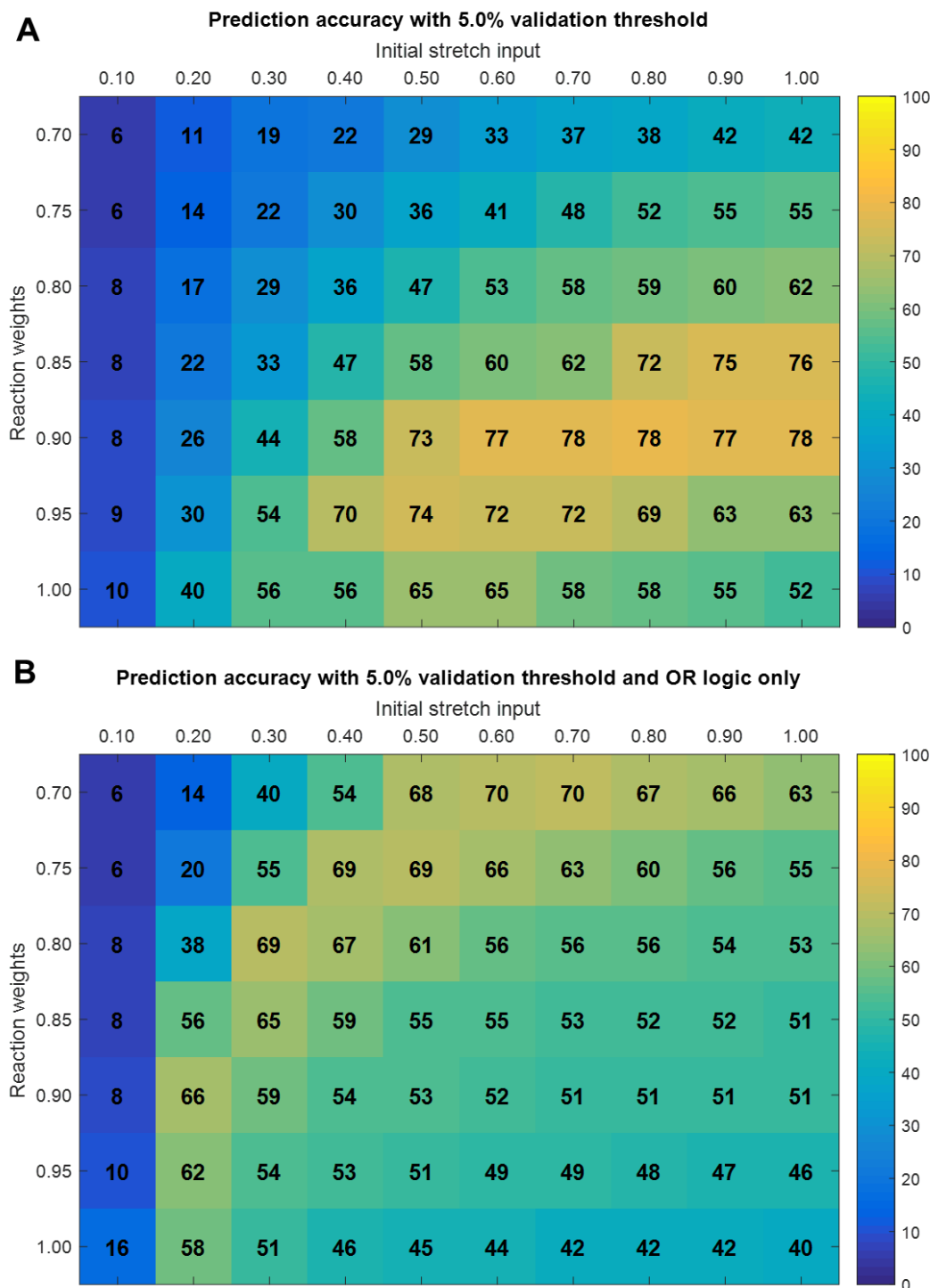


Figure 2.6. Model logic influences prediction accuracy. (A) Prediction accuracy of the original model. (B) Prediction accuracy of a model version with all activating AND reactions converted to OR reactions. For each version, network validation was tested across a range of initial stretch inputs (from 0.10 to 1.0) and default reaction weights (from 0.7 to 1.0), using a validation threshold of 5% absolute change.

network to inhibition of specific receptors, kinases, or genes. Influential nodes were defined as those whose knockdown causes the greatest activity changes across a given portion of the network. Based on the network-wide sensitivity analysis (Fig. 2.7), we identified the 15 nodes with the highest influence over transcriptional activity and over the gene expression outputs (Fig. 2.8A). These most influential nodes encompass proteins mediating signals from each of the primary mechano-sensors: Ca^{2+} and calmodulin, downstream of the stretch-sensitive ion channels; $G\alpha_{q/11}$, which transmits signals from AT1R; and actin and α -actinin, which relay forces from integrins and the dystrophin–dystroglycan complex. Also highly included are previously identified central network hubs for biochemically-stimulated hypertrophy, such as Ras and PI3K. Rather than being controlled by one specific mechano-sensor, most of the hypertrophic outputs display sensitivity to all the stretch-responsive pathways (Fig. 2.8A, lower panel).

In contrast to the outputs, which tend to be broadly sensitive to perturbations in many different parts of the network, most of the transcription factors display sensitivity only to certain mechano-signaling pathways (Fig. 2.8A, upper panel). For example, CREB, FoxO, and GATA4 are primarily regulated by AT1R through the PI3K/Akt pathway, while cFos activity is specific to Raf1 signaling through MEK1/2. To systematically determine the control structure underlying differential control of transcriptional activity, we performed hierarchical clustering on the reduced sensitivity matrix shown in Fig. 2.8A. Using a distance criterion of 0.3 to form groups revealed six clusters, each of which regulates a distinct set of transcription factors. We identified the topologically highest node from each cluster, and then used this to create a simplified network schematic demonstrating how these key hubs—calcium, actin, Ras, Raf1, PI3K, and JAK—link the mechano-sensors to the transcription factors (Fig. 2.8B). Of these six hubs, two are influenced by the mechano-sensitive calcium channels (TRP and LTCC), two are influenced by the cytoskeletal mechano-sensors (integrin and dystroglycan), and five are influenced by AT1R.

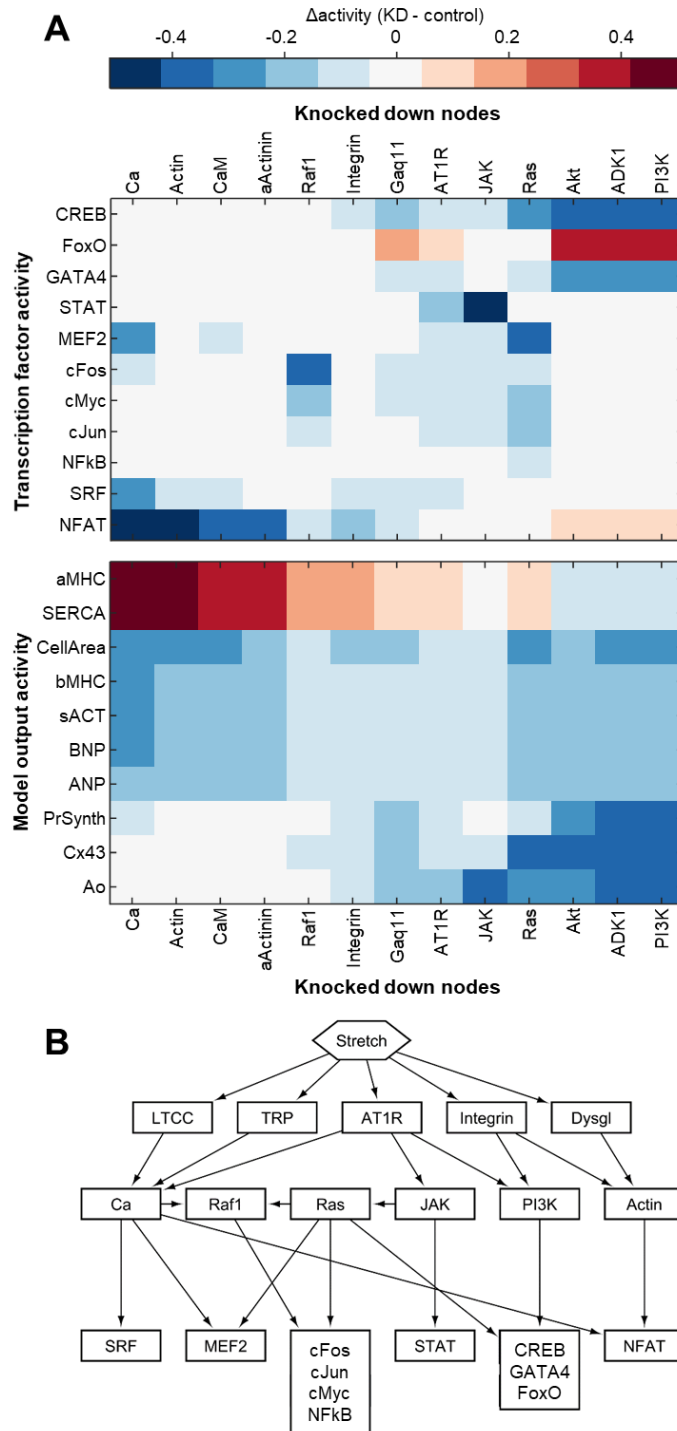


Figure 2.8. Sensitivity analysis reveals modular network structure. (A) Network sensitivity to most highly influential hubs. Subset of the sensitivity matrix showing the response of each of the transcription factors and outputs to half-knockdown of each of the 12 nodes causing the highest average response across the transcription factors and outputs, as well as integrin. (B) Simplified network schematic showing control of transcription factors by 6 key hubs.

2.4.4. Screen for combination mechano-therapies

While we predicted several individual regulators whose inhibition could reduce stretch-induced gene expression, combination therapies may outperform individual perturbations administered in isolation [129]. For example, the FDA recently approved valsartan/sacubitril (initially known as LCZ696 and branded as Entresto) for treating heart failure [13], [14]. Both components of this combination drug affect pathways known to be mechano-sensitive: valsartan inhibits AT1R, and sacubitril increases cGMP by inhibiting neprilysin and thus reducing natriuretic peptide degradation. However, neither the combined effects of these two components on stretch-induced signaling, nor the effect of sacubitril alone, have been assessed to date. To examine valsartan/sacubitril's influence on cardiac mechano-signaling, we simulated the response to varying levels of valsartan and sacubitril both separately and together. Sacubitril's anti-hypertrophic effects result from cGMP activating PKG1, which inhibits several different calcium channels and the downstream calcineurin/NFAT pathway (Fig. 2.9). The model predicts that valsartan/sacubitril will attenuate stretch-induced hypertrophy in myocytes at lower concentrations than either of its individual components (Fig. 2.10).

Given the predicted benefits of valsartan/sacubitril, as well as the power of systems analysis of drug interactions to uncover network function [130], we were interested in exploring the potential for other drug pairs to reduce mechanically driven hypertrophy. To identify other mutualistic combinations, we ran a sensitivity analysis simulating all pairwise combinations of inhibiting or activating every node in the network, and compared their inhibitory power to that of targeting single nodes (results for BNP shown in Fig. 2.11). Many of these combinations have additional benefit over single perturbations, including several other combinations with angiotensin receptor blockers. These include inhibiting ET1R, Ras, or integrin signaling simultaneously with AT1R inhibition. The highest-scoring combinations also include several pairings with drugs increasing cGMP, such as those inhibiting NHE or NCX (sodium–calcium exchanger). Other upregulated members of the fetal gene program followed similar patterns to those for BNP, each sharing at least 72% of the top 50 combinations with highest additional benefit.

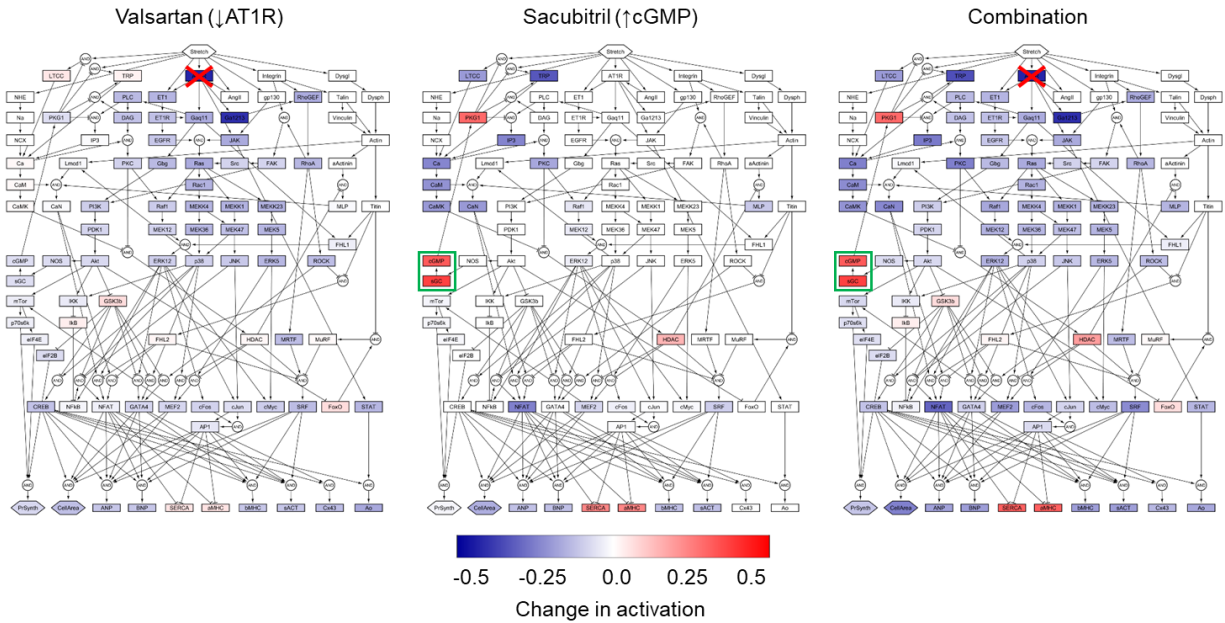


Figure 2.9. Network displays higher response to valsartan and sacubitril combined than individually. Response of network to valsartan (simulated by progressive inhibition of AT1R), sacubitril (simulated by progressive activation of cGMP through sGC), and the combination of valsartan and sacubitril, all in the context of steady-state stretch activation.

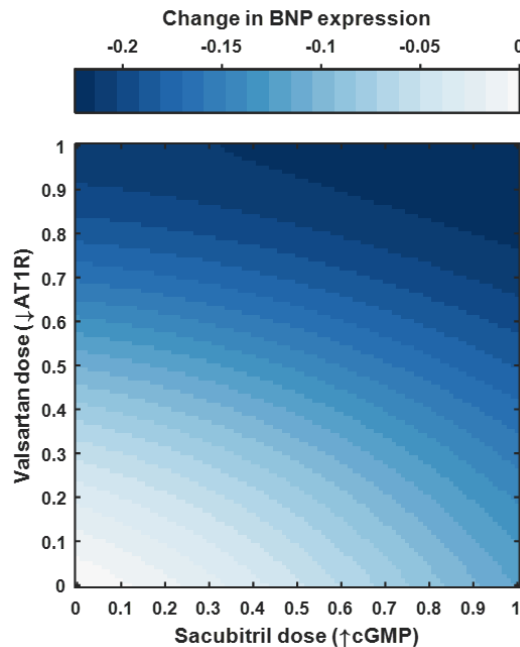


Figure 2.10. Model predicts higher efficacy of combined valsartan and sacubitril treatment. Response of BNP to increasing doses of valsartan (simulated by progressive inhibition of AT1R) and sacubitril (simulated by progressive activation of cGMP through sGC) in the context of steady-state stretch activation.

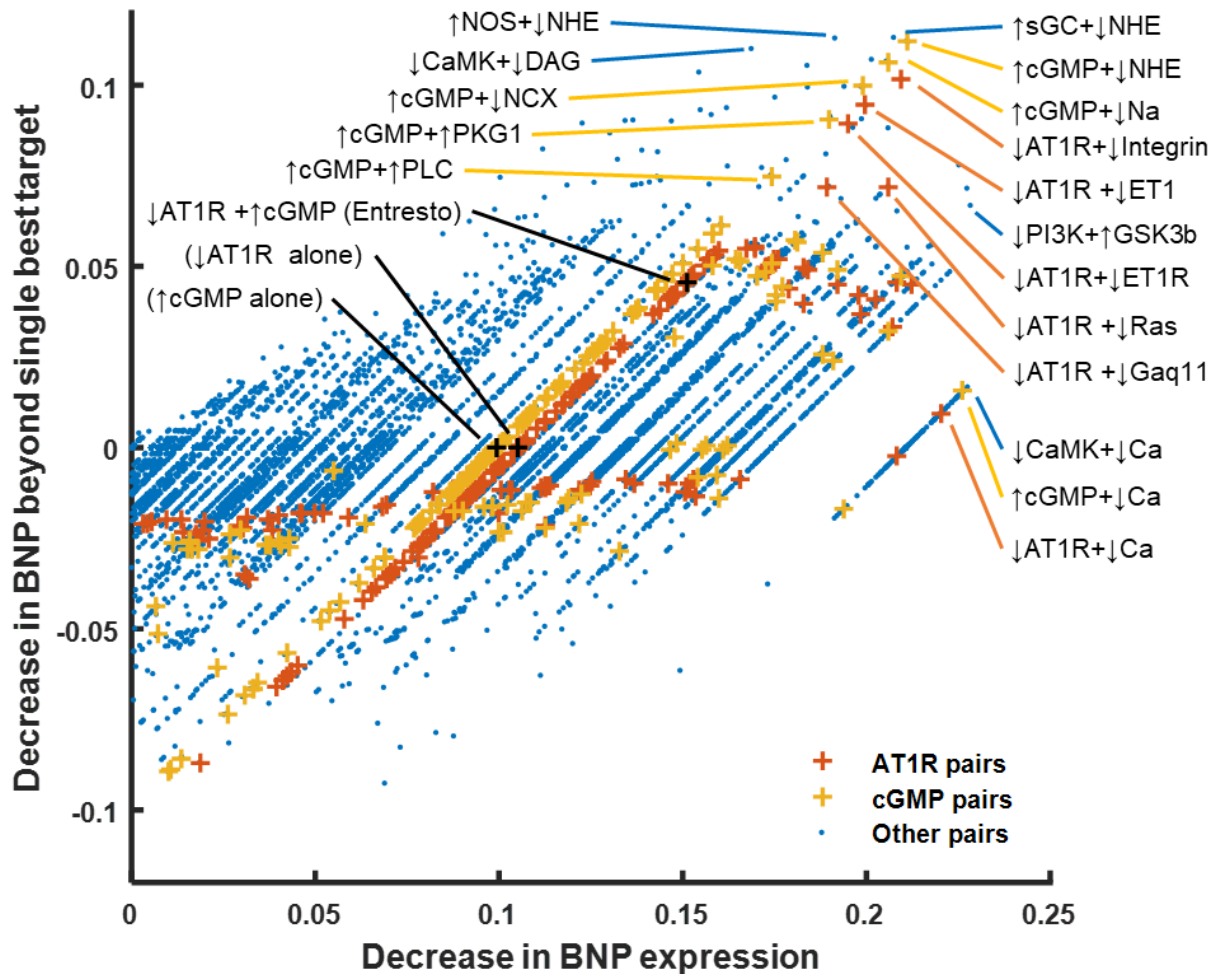


Figure 2.11. Model predicts efficacy of other combination mechano-therapies. All pairwise combinations of reducing or increasing Y_{\max} that lowered BNP expression. The x-axis shows the change in BNP relative to steady-state stretch activation, and the y-axis shows the difference between this change and the larger of those caused by targeting either node independently.

2.5. Discussion

2.5.1. Cardiac mechano-signaling model

The high degree of redundancy and crosstalk [111] between stretch-sensitive pathways in the heart renders a systems approach invaluable for identifying mechanisms of signal integration. By developing and validating a comprehensive literature-based reconstruction of the cardiac mechano-

signaling network, we demonstrated how network logic and crosstalk between signaling pathways enable cardiomyocytes to integrate distinct mechanical stimuli into a coherent response. Our model, which incorporates five primary mechano-sensors and 94 mechano-responsive nodes connected by 125 reactions, identified calcium, actin, Ras, Raf1, PI3K, and JAK as key regulators of mechanical cues. Although each of these hubs operates through distinct sets of transcription factors, all are crucial for stretch-induced cellular remodeling and activation of the fetal gene program. We also revealed a PKG-dependent mechanism contributing to the mutualistic action of the combination drug valsartan/sacubitril, and predicted further pairs of drug targets with maximum effects on mechano-signaling.

2.5.2. Model validation

Observations from literature not used in network construction confirmed 78% of model predictions, and the validation rate remained high across wide range of random variation in multiple model parameters. Of the 38 disagreements, the most common (18 instances) were due to the model correctly predicting a change in response to inhibition that was observed in the literature (e.g., a decrease in stretch-induced ANP expression caused by LTCC blockade), but at a magnitude below the 5% threshold. In these cases, more influence could be given to LTCC by modulating the relative weights of downstream reactions within the model to bring the response magnitude above the threshold. Other discrepancies involved inhibitory effects observed in the literature where no connection exists in the model (9 instances), such as lowered stretch-induced Ras phosphorylation in response to PI3K inhibition, or inhibitory effects predicted in the model that were not observed in the literature (7 instances), such as lowered stretch-induced ERK1/2 activity after Ras inhibition. These points of disagreement highlight specific areas where future model revision or further experiments are necessary.

2.5.3. Key hubs integrating mechano-signals

A longstanding question in cardiac mechanotransduction has been whether the diverse array of stretch-induced signaling pathways function independently or synergistically [131]. Our sensitivity

analysis found that while the various pathways maintain mostly independent control over distinct groups of transcription factors, synergy between multiple pathways is necessary to activate all the transcription factors necessary for gene transcription and hypertrophy. Hierarchical clustering based on our sensitivity analysis identified calcium, actin, Ras, Raf1, PI3K, and JAK as the key network hubs integrating signals from the mechano-sensors. Rather than being concentrated in a single pathway, these most influential nodes are distributed across the network and integrate stretch signals from all five primary mechano-sensors. These results help explain why modeling network connectivity and logic correctly is essential for successfully predicting myocyte sensitivity to modulation of a diverse array of stretch-activated pathways.

2.5.4. Synergistic targets regulate stretch-induced hypertrophy and gene expression

Inhibiting neprilysin counters wide-ranging effects of neurohormonal overactivation, such as vasoconstriction and sodium retention, and angiotensin receptor blockers (ARBs) can reduce blood pressure without the angioedemic effects of angiotensin-converting–enzyme (ACE) inhibitors [13]. Here, however, we were particularly interested in how these two interventions could modulate mechano-signaling in cardiomyocytes. Multiple studies have shown that ARBs can attenuate stretch-induced signaling in cardiomyocytes [64], [132], [133], but a corresponding function for neprilysin inhibition has not been examined either by itself or together with ARBs. We identified a mechano-inhibitory role of the neprilysin inhibitor sacubitril in blocking stretch-sensitive calcium channels with PKG1 by increasing cGMP levels through increased natriuretic peptide receptor stimulation. Our model also predicts that the valsartan and sacubitril reduce hypertrophy more in combination than on their own.

Analysis of all pairs of targets in the network revealed hundreds of potential combinations that inhibit mechano-signaling more significantly in tandem than individually. The high levels of additional inhibition predicted from targeting two nodes simultaneously underscore the importance of a systems pharmacology perspective for crafting new therapies, rather than merely attempting to target the single most important mechano-sensor [134]. Although few of these combinatorial perturbations have

previously been tested in the context of cardiac mechano-signaling, the available evidence concurs with our results. For example, the model predicts that inhibiting AT1R and ET1R together should reduce BNP secretion more than inhibiting either individually, and this outcome has been confirmed both in stretched cardiomyocytes [122] and in rats induced with volume overload [133]. Many of the highest changes predicted involve other pairs targeting AT1R or cGMP, suggesting that other drug combinations involving valsartan or sacubitril would be worth pursuing experimentally.

2.5.5. Limitations and future directions

While the scope of the network reconstruction necessitated the use of default parameters, refinement of parameter weighting as more data becomes available can increase model accuracy. To further enrich the model, future curation could incorporate paracrine signaling from mechanically activated fibroblasts [112], juxtacrine signaling through cadherins [135], more complex autocrine feedback [58], and interaction with related signaling cascades, such as the beta-adrenergic network [105]. Integrating biophysical mechanisms such as force propagation, diffusion, and electrophysiology, which are not directly represented in the current model, could also prove fruitful [113], [115], [117], [136].

Our work also highlights critical gaps in the current understanding of cardiac mechano-signaling. Although the five primary mechano-sensors in the model have each been verified as immediately responsive to mechanical strain, it is unclear whether the activation of several other “stretch receptors” is direct or indirect. For example, there is broad agreement that NHE mediates stretch-dependent signals [121], but it remains controversial whether the role of NHE is dependent on both AT1R and ET1R [132], [137], on ET1R alone [138], or on neither [139], [140]. Likewise, activation of gp130 and autocrine release of Ang II and ET-1 have all been implicated as contributors to stretch-induced signaling [52], [57], [122], but the direct cause of each of these effects remains unknown. As others have noted [19], more work is needed to discern which “stretch receptors” are indeed directly responsive to mechanical strain, and which are activated indirectly.

2.5.6. Conclusions

In this chapter, we developed a large-scale predictive model of cardiac mechano-signaling that identifies the nodes and network structures regulating the response to stretch in cardiomyocytes. Sensitivity analysis of our manually curated network showed that rather than a single stretch sensor governing the response to mechanotransduction, coordination is likely necessary between AT1R, cytoskeletal proteins, and stretch-sensitive ion channels to induce gene expression and hypertrophy. The model also predicts that calcium, actin, Ras, Raf1, PI3K, and JAK are each key hubs with distinct signatures of transcriptional regulation. In addition, we found that network logic is essential for allowing gene expression to be sensitive to a diverse array of mechano-sensors. Our approach integrates results from hundreds of past studies into a coherent model, revealing network interactions unapparent from studying any one pathway in isolation.

Chapter 3

Differential control of diverse cardiomyocyte hypertrophy phenotypes

The following individuals contributed to the work in this chapter: Philip M. Tan, Karen A. Ryall, Alexander M. Paap, Matthew T. Rhoads, and Jeffrey J. Saucerman. Some work in this chapter adapted from Karen A. Ryall, Vassilios J. Bezzerides, Anthony Rosenzweig, and Jeffrey J. Saucerman, “Phenotypic screen quantifying differential regulation of cardiac myocyte hypertrophy identifies CITED4 regulation of myocyte elongation,” *J. Molec. Cell. Cardiol.*, vol. 72, p. 74–84, Jul. 2014.

Author contributions: P. M. Tan—conceptualization, data analysis, validation experiments, computational modeling, paper writing. K. A. Ryall—conceptualization, initial experiments. A. M. Paap—data analysis. M. T. Rhoads—data analysis. J. J. Saucerman—conceptualization, funding acquisition, supervision, paper editing.

3.1. Foreword

In the previous chapter, we determine key network drivers of cardiomyocyte remodeling in response to a single stimulus, mechanical stretch. We now expand the focus to multiple stimuli, investigating which signaling pathways control variant remodeling outcomes in cardiomyocytes. The divergent response of the heart to physiological versus pathological stresses has been well characterized. However, less is known about which signaling pathways govern distinct features of hypertrophy, such as area, elongation, and fetal gene expression. By combining high-content imaging, RPPA, and gene expression in a data-driven modeling framework, we identify and validate targets that differentially regulate hypertrophic phenotypes.

3.2. Introduction

Hypertrophic remodeling is associated with a wide range of clinical outcomes. Remodeling induced by physiological stresses such as athletic training occurs without cardiac dysfunction, but heart growth that occurs in a disease setting places patients at high risk of heart failure [141]. The distinct trajectories of cardiac remodeling associated with varying clinical outcomes are driven at the cellular level by different forms of myocyte growth [46]. For example, myocyte elongation, caused by assembly of contractile protein units in series, characterizes hearts undergoing eccentric hypertrophy with ventricular dilation. In contrast, increased cross-sectional area, caused by assembly of contractile units in parallel, characterizes hearts undergoing concentric hypertrophy with ventricular thickening [142], [143]. Since eccentric remodeling poses a particular risk to patients [16], identifying the molecular networks governing shape changes in myocytes is important to developing more effective therapies.

Previous work has reconstructed the signaling cascades launched by a wide array of hypertrophic stimuli and located the most influential hubs governing the network [27]. In addition, these hypertrophic stimuli have been found to differentially regulate varying responses in myocytes in vitro [17]. Phenylephrine and endothelin-1, for instance, strongly induce increased area; neuregulin-1 (Nrg), on the

other hand, is associated with CITED4 expression and myocyte elongation. However, given the high degree of crosstalk and feedback in the system, it remains unclear which specific pathways in the hypertrophy signaling network govern these inputs and outputs.

Here, we integrate biochemical and image data to identify signaling pathways differentially controlling distinct types of cardiomyocyte remodeling. We quantified the response of 172 proteins and phospho-proteins to four hypertrophic agonists, and developed a partial least squares regression model to correlate this activity with changes in gene expression and myocyte shape. The model revealed two primary axes of signaling activity, corresponding to growth and eccentricity. Members of the MAPK and PI3K cascades were strongly associated with Nrg stimulation, suggesting that Nrg-induced elongation is dependent on these pathways. In addition, pro-apoptotic proteins were highly anti-correlated with ET and Nrg stimulation. Follow-up experiments validated a role for MEK1 and PI3K in Nrg-induced myocyte elongation, and implicated Src involvement as well.

3.3. Methods

Note: All portions of sections 3.3.1 through 3.3.3 involving the phenotypic screen have been published as Karen A. Ryall, Vassilios J. Bezzerides, Anthony Rosenzweig, and Jeffrey J. Saucerman, “Phenotypic screen quantifying differential regulation of cardiac myocyte hypertrophy identifies CITED4 regulation of myocyte elongation,” *J. Molec. Cell. Cardiol.*, vol. 72, p. 74–84, Jul. 2014.

3.3.1. Cell culture

Cardiac myocytes were isolated from 1–2-day-old Sprague Dawley rats using the Neomyts isolation kit (Cellutron, Baltimore, MD). Myocytes were cultured on dishes coated with SureCoat (a combination of collagen and laminin; Cellutron) and in plating medium (Dulbecco’s modified Eagle medium, 17% M199, 10% horse serum, 5% fetal bovine serum, 100 U/mL penicillin, and 50 mg/mL streptomycin). All procedures were performed in accordance with the Guide for the Care and Use of

Laboratory Animals published by the US National Institutes of Health and approved by the University of Virginia Institutional Animal Care and Use Committee.

Cardiac myocytes were harvested from 1 to 2 day old Sprague Dawley rats using the Neomys isolation kit (Cellutron, Baltimore, MD). Myocytes were cultured in plating media (Dulbecco's modified Eagle media, 17% M199, 10% horse serum, 5% fetal bovine serum, 100 U/mL penicillin, and 50 mg/mL streptomycin) at a density of 100,000 cells per well of a 96-well plate coated with SureCoat (a combination of collagen and laminin, Cellutron). All procedures were performed in accordance with the Guide for the Care and Use of Laboratory Animals published by the US National Institutes of Health and approved by the University of Virginia Institutional Animal Care and Use Committee. Two days after isolation, myocytes were transfected with GFP under a cardiac myocyte specific troponin T promoter [17] using Lipofectamine 2000 (Invitrogen, Carlsbad, California; transfection efficiency: 10–15%). Two days after transfection, myocytes were imaged using automated image acquisition scripts, which collect a 5×5 grid of images in each well of interest in the 96-well plate [18]. Images were collected using an Olympus IX81 inverted microscope with 10× UPlanSApo 0.40 NA objective, Orca-AG CCD camera (Hamamatsu, Bridgewater, NJ), automated stage (Prior Scientific, Rockland, MA), and IPLab (Scanalytics, Fairfax, VA) or MetaMorph (Molecular Devices, San Jose, CA) software.

3.3.2. Quantifying changes in shape

After initial images were collected, myocytes were rinsed and cultured in serum-free medium. For the phenotypic screen, each well contained a hypertrophic agonist: 1 μ M angiotensin II (Ang), 100 nM endothelin-1 (ET), 10 nM insulin growth factor-1 (IGF), or 10 ng/mL neuregulin-1 (Nrg). For the validation experiments, 100 ng/mL Nrg was used, and each well contained one of two concentrations (0.1 μ M or 10 μ M) of an inhibitor: PD0325901 (against MEK1); BIX-02189 (against MEK5); SB203580 (against p38); GDC-0941 (against PI3K); or WH-4-023 (against Src).

After 48 hr post-treatment, myocytes were imaged again. 48-hr stimulation allowed for robust changes in cell size and shape to be measured while maintaining cell health in serum free conditions. Changes in myocyte area, perimeter, form factor, elongation, and integrated fluorescence intensity were calculated using automated custom MATLAB image analysis algorithms. The elongation of a cell body is similar to but distinct from its eccentricity; it is defined as the major axis divided by the minor axis, where the major and minor axes are those of an ellipse with the same normalized second central moments as the cell body. A perfectly circular cell thus has the minimum possible elongation of 1. The form factor, in turn, is a measure of the compactness of a cell body given its size, and equals $4\pi A/P^2$, where A is the area and P is the perimeter. For the phenotypic screen, shape measurements were recorded from two wells from three independent myocyte isolations, taking the median value for each change in a morphological metric across the cells within each isolation. For the validation experiments, shape measurements were recorded from four wells, taking the median value for each change in a morphological metric across the cells within each well.

3.3.3. Quantifying changes in transcript abundance

48 hr after stimulation with the hypertrophic agonists, total RNA was purified from myocytes using the RNeasyMini kit (Qiagen, Valencia, CA). Complementary DNA was synthesized from 85.5 ng of total RNA using the iScript cDNA synthesis kit (Bio-Rad). mRNA levels of twelve genes (Bcl-2, Bax, C/EBP β , CITED4, VEGF, Serca2a, BNP, skeletal α -actin, I κ B, TNF α , CTGF, and GAPDH) were measured using qPCR (BioRad CFX Connect) using iTaq Universal SYBR Green Supermix (Bio-Rad), 2 ng of cDNA, and 400 nM of each primer set. GAPDH served as internal control. Gene-specific primers were designed on PrimerQuest (Integrated DNA Technologies, Inc.) A list of primers used is shown in Supplementary Table S2 of the original publication [17]. Data were analyzed using the comparative CT method with efficiency correction [144]. Measurements were collected from three independent myocyte isolations.

3.3.4. RPPA proteomics analysis

For the reverse phase protein array (RPPA), neonatal rat ventricular myocytes were cultured in 24-well plates (500,000 myocytes/well). Four days after isolation, myocytes were rinsed and cultured in serum-free media containing 10 ng/mL Nrg, 10 nM ET, 1 μ M Ang, 10 nM IGF, or serum (10% horse serum and 5% fetal bovine serum). Myocyte protein was isolated at two time points (1 hr and 48 hr) following administration of the agonists, according to the protocol on the MD Anderson Cancer Center RPPA Core Facility website. Protein concentration was quantified using the Pierce 660 nM Protein Assay Kit (Thermo Scientific). Cell lysates were submitted to the MD Anderson Cancer Center RPPA Core Facility for analysis of 172 proteins and phospho-proteins. Data was collected from two independent myocyte isolations per condition, and all data points were normalized for protein loading.

3.3.5. Partial least squares regression

Partial least squares regression (PLSR) was performed in MATLAB, using the RPPA data (protein expression) as the predictor block and the phenotypic screen data (gene expression and morphology) as the response block. The predictor block contained 4 ligands versus 172 proteins, and the response block contained 4 ligands versus 15 phenotypes (11 mRNAs and 4 morphology metrics). For each block, data for each output were centered and scaled beforehand by taking the z-score across the ligands. To calculate the calibration root mean-squared errors (RMSE), the data from all four ligands were used to build a PLSR model, which was then evaluated using the same data. To calculate the validation RMSE, four different PLSR models were built, each using the data from only three of the ligands. Each model was then evaluated using data from the one ligand that had been held out, and the mean of the resulting errors was taken.

3.4. Results

3.4.1. Ligands differentially induce diverse protein signaling pathways

In the phenotypic screen previously published [17], we measured protein activity from four ligands—Ang, ET, IGF, and Nrg—using a reverse phase protein array. The ligands tested induced a diverse array of responses among the 172 proteins and phospho-proteins measured (Fig. 3.1). Among the most intense responses were members of the PI3K signaling pathway. PI3K, a key hub in the cardiomyocyte hypertrophy signaling network [27], binds to PDK1 and enables it to phosphorylate Akt [145], [146]. Akt in turn phosphorylates GSK3 β and mTOR [147], and mTOR catalyzes phosphorylation of S6 kinases such as p70S6K [148]. From this pathway, several proteins showed strong phosphorylation in response to Nrg-1, including Akt (at T308 and S473), GSK3 (at S9), GSK3 α/β (at S9/S21), mTOR (at S2448), p70S6K (at T389), and S6 (at S235/S236 and S240/244). Some of these proteins also showed phosphorylation in response to Ang or ET, though to a lesser degree. In contrast, a slew of pro-apoptotic proteins, such as Bim, Beclin, and caspase 8 [149], were all downregulated by both ET and Nrg.

As with the PI3K pathway, proteins within the MAPK pathway also showed strong activation in response to Nrg, including phosphorylation of C-Raf (at S338) and MAPK (at T202/Y204). Ang strongly increased expression of YAP and TAZ, the main effectors of the Hippo pathway [150], as well as ERCC1 (an excision repair protein), phospho-PEA15 (a death effector domain-containing protein), Bax, and paxillin. Fewer proteins increased specifically in response to ET, but among these were c-Myc, FASN (fatty acid synthase), PR (progesterone receptor), and CDK1 (cyclin-dependent kinase 1). Likewise, not many proteins increased specifically in response to IGF. Notably, GAPDH, which is often used as a housekeeping protein for normalization [151], varied widely among the four conditions, being expressed most abundantly under Ang and least abundantly under Nrg.

It should be noted that the correlation between the two biological replicates for the RPPA was fairly low, with a median Pearson's correlation coefficient of $r = 0.24$ and a median p -value of 0.45 across the

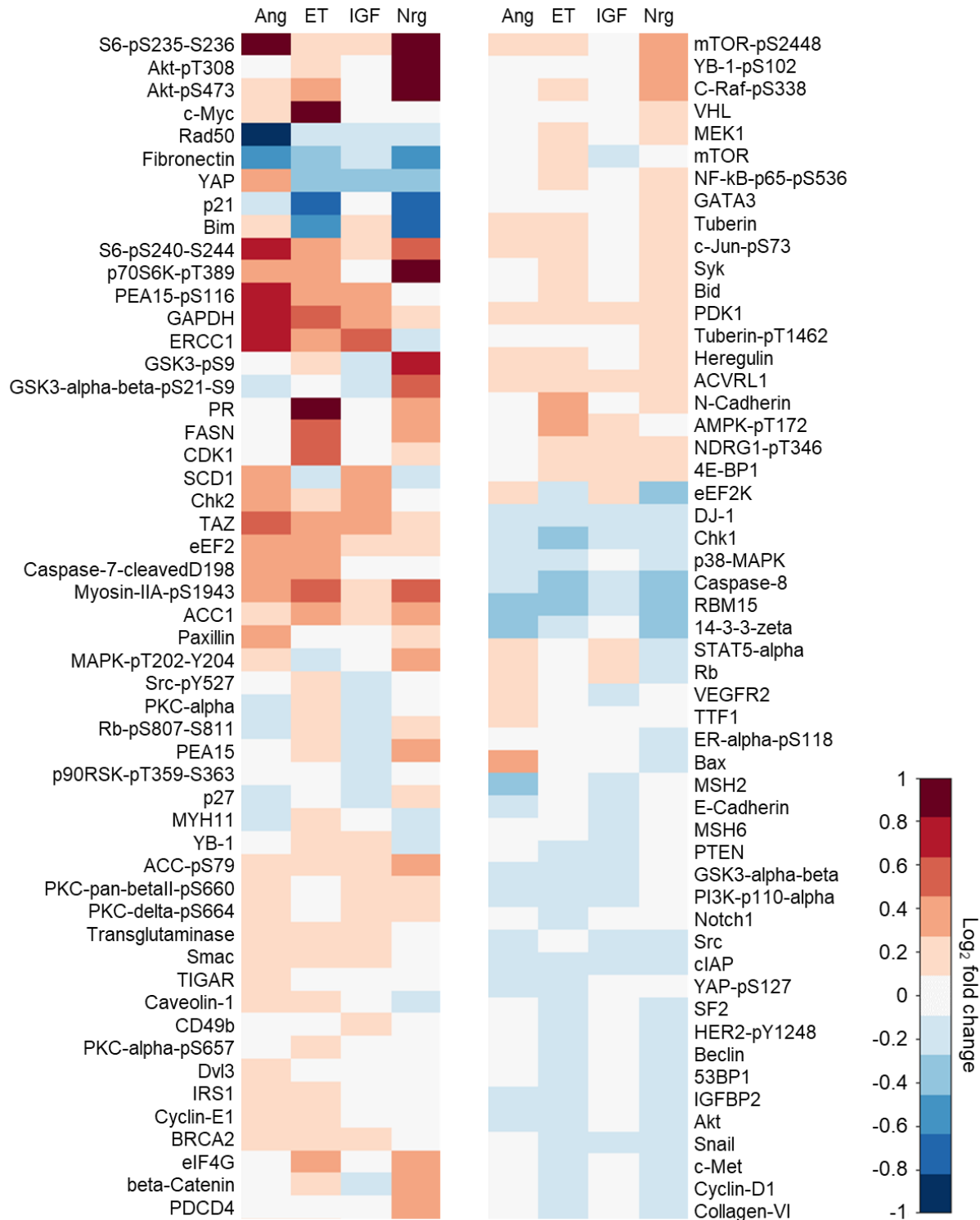


Figure 3.1. Hypertrophic ligands induce diverse changes in protein expression and phosphorylation. Hierarchical clustering of the subset of RPPA data with a total log₂ fold change of at least 0.2 across conditions. Protein levels were measured after 48 hours of treatment. Values shown are averages of two biological replicates, normalized against a serum-free condition.

172 proteins. Only 21% of the proteins had an r -value of more than 0.50, and only 15% of them had a p -value of less than 0.05. However, when we restricted the RPPA proteins in the predictor block to those with high (>0.5) correlation values, the overall structure of the resulting projection did not change, confirming that the model was robust to involving the entire dataset. Moreover, the internal consistency of phosphorylation activity within individual signaling pathways and the consistency of the observations with prior knowledge suggested that the dynamics observed were biologically significant. In particular, we sought to educe the links in cardiac myocytes between protein phosphorylation and the resulting downstream phenotypes.

3.4.2. PLSR clusters families of protein activity and links them to distinct morphologies

In our previously published phenotypic screen [17], ET was shown to increase myocyte area strongly, and Nrg was identified as a potent regulator of myocyte elongation. To link these experiments on shape and transcript abundance to our proteomic data, we developed a partial least squares regression (PLSR) model encompassing both datasets. PLSR is a powerful tool for reducing dimensionality and visualizing correlations in order to gain insight into signaling network design [152]. Our model uses protein expression as the predictor block and uses gene expression and morphology as the response block, condensing the 172-axis RPPA space and mapping it onto the 15-axis space from the phenotypic screen (Fig. 3.2). The model visualizes the two datasets on a single pair of axis that together capture 93% of the variance across the four ligands (Fig. 3.3).

As expected from examining the RPPA data alone, the four ligands each drive distinct clusters of protein signaling activity, as seen by superimposing the PLSR scores of the ligand inputs over the loadings of the RPPA and phenotypic outputs. Several of the patterns that had been noted earlier now appear more starkly. For example, many members of the PI3K pathway cluster together tightly and in close association with elongation, such as phospho-PI3K, phospho-Akt, phospho-PDK1, phospho-GSK3, phospho-mTOR, and phospho-p70S6K. A similar cluster emerges for participants in MEK signaling, such

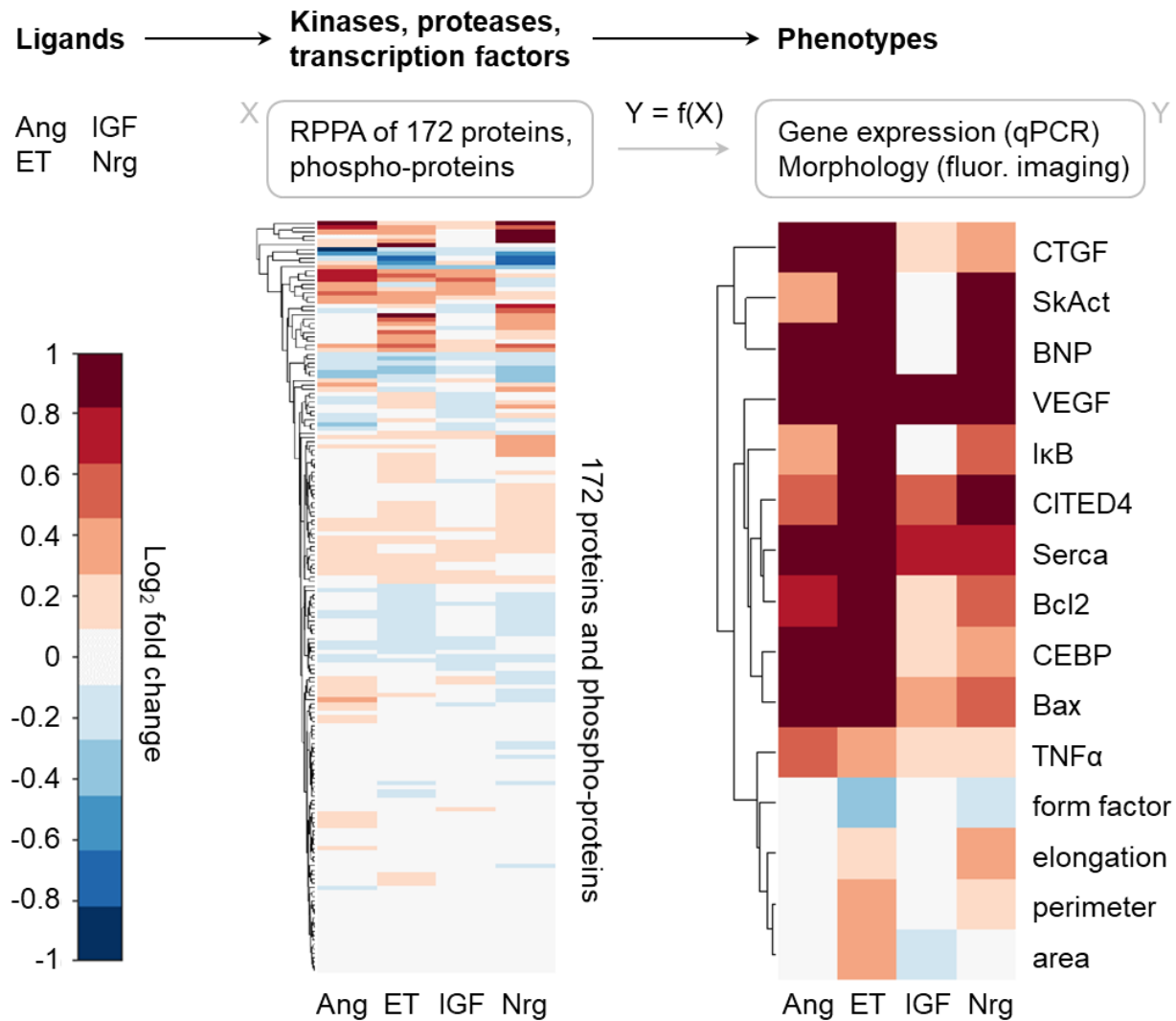


Figure 3.2. Protein expression, gene expression, and morphological changes induced by four hypertrophic ligands. Overview of experimental design for PLSR model, in which the goal is to identify fundamental relationships between protein and phospho-protein expression (predictor block) and gene expression and morphological changes (response block). Protein levels were measured by RPPA 48 hours after treatment, gene expression was measured by qPCR 48 hours after treatment, and morphology of individual cells was tracked by fluorescent microscopy from before treatment to 48 hours after treatment. Values shown are averages of two biological replicates for RPPA, and of three biological replicates for qPCR and fluorescent imaging (average of 347 cells tracked for each replicate). All values are normalized against serum-free controls. Data from phenotypic screen previously published in Ryall *J. Molec. Cell. Cardiol.* 72, 2014.

as phospho-C-Raf, phospho-MEK1, phospho-MAPK, and phospho-p90RSK. The absolute abundance of some of these proteins, such as C-Raf and MEK1, displays a similar trend, and phospho-p38 appears

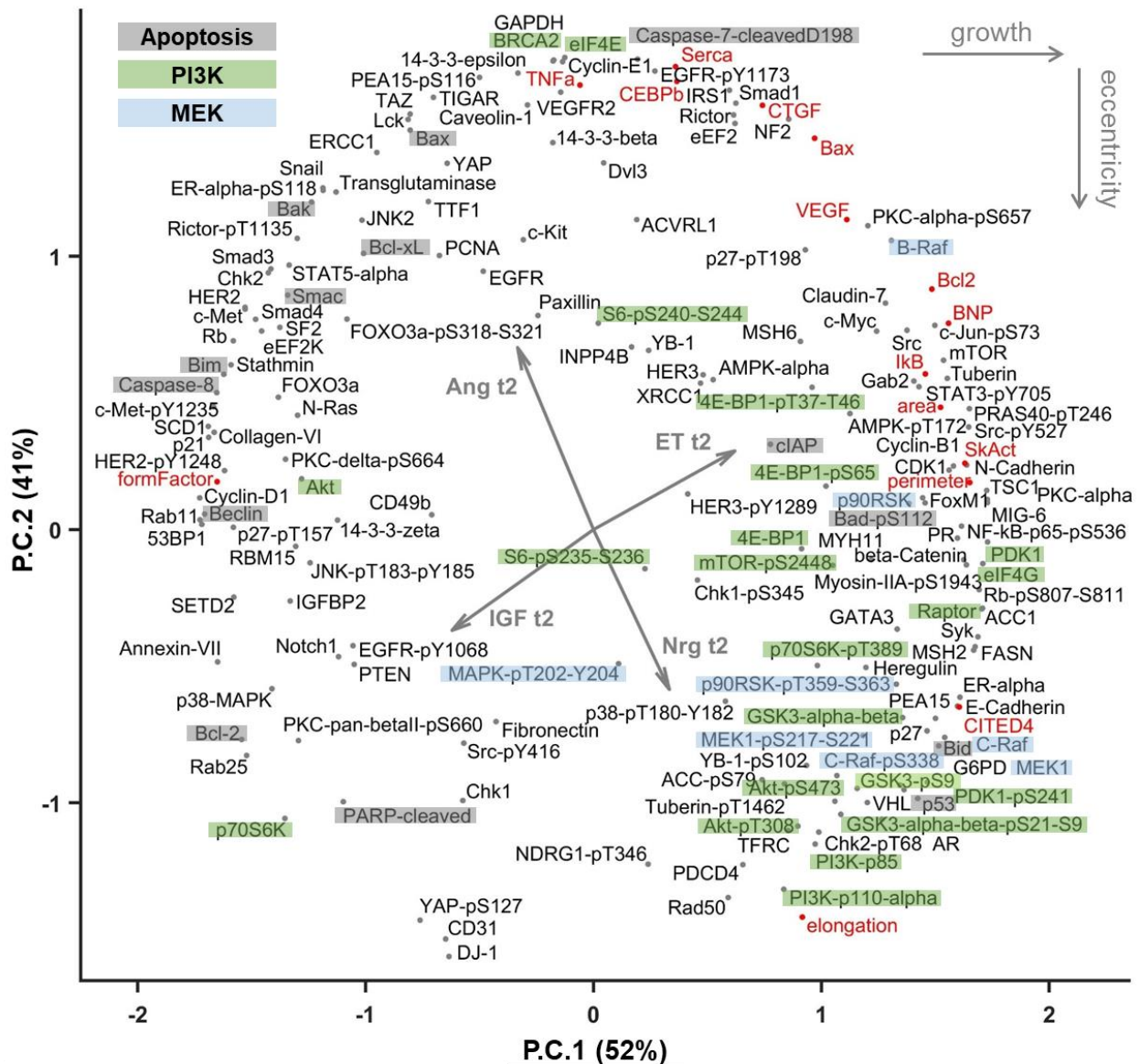


Figure 3.3. Individual signaling pathways correlate with distinct hypertrophic phenotypes. PLSR loadings are plotted for protein expression (predictor block; black) and for gene expression and morphology (response block; red). Members of MEK, PI3K, and apoptotic signaling pathways tend to cluster together as emphasized by highlighting, which was applied manually based on canonical groupings in the literature. Grey arrows show orientation and relative magnitude of PLSR scores for ligand inputs. Percentages indicate variance explained by each principal component.

nearby. In contrast, pro-apoptotic proteins are projected to the opposite end of the PLSR space, in the direction of form factor and the Ang direction: In this region are located Bax, Bak, Bim, Bcl-xL, Beclin, Smac, Caspase 8, and (to a lesser extent) Bcl-2, cleaved PARP, and cleaved caspase 7.

While area and perimeter are projected to the far right of the space, form factor (a measure of cell roundedness), which would be expected to be higher in apoptotic cells, appears on the far left, close to the pro-apoptotic signaling cluster. Based on this observation, we interpreted the first principal component of the model as a “growth axis”. Similarly, since elongation appears toward the right side of the space but at the very bottom, we interpreted the second principal component as an orthogonal “eccentricity” axis. Nrg strongly drives the eccentricity axis, whereas ET, with some contribution from Nrg, is primarily responsible for the growth axis.

While this model is useful for visualizing trends and inferring correlations between protein activity and downstream remodeling, it has no ability to predict one condition solely based on the other three, indicating that each governs relatively distinct regions of the signaling space (Fig. 3.4). This is not surprising, given that it was built using only four conditions (corresponding to the four ligands) from each block. In essence, this approach is conceptually similar to running principal components analysis (PCA) on each of the two data blocks separately and then superimposing the results, but has the added benefit of

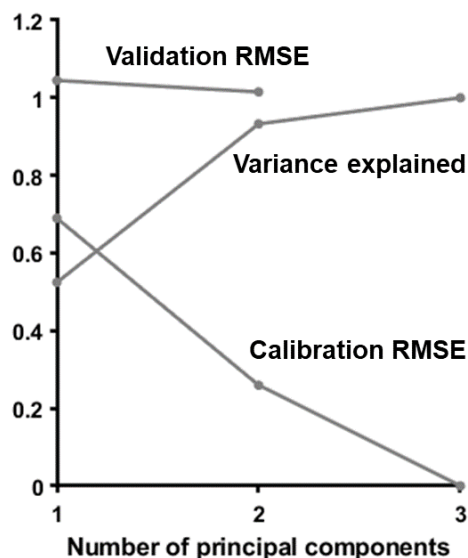


Figure 3.4. PLSR model provides descriptive but not predictive value. Increasing the number of principal components captures more variance and decreases root mean-squared errors (RMSE) when resubstituting original data, but does not decrease RMSE of validation by holdout.

maximizing covariance between the two blocks to gain correlative insight between proteomics and phenotype. Indeed, when we reduced each block to two dimensions using PCA, the resulting structure of the outputs for each block was very similar to that observed within the PLSR (data not shown).

3.4.3. MEK1, PI3K, and Src mediate Nrg-induced elongation

Given the close association of the MEK1, PI3K, and p38 signaling pathways with Nrg and elongation in the PLSR model, we hypothesized that one or more of these could be responsible for mediating Nrg-induced elongation. To evaluate this possibility, we tested inhibitors against MEK1, PI3K, and p38 in myocytes exposed to Nrg. We also included inhibitors against Src and against MEK5; Src has been identified as a modulator of Nrg-induced elongation in myocytes [35], whereas MEK5 has been implicated in myocyte elongation downstream of gp130 in response to CT-1 [33] and LIF [30], [31].

As observed in the phenotypic screen, myocytes displayed a robust lengthening response to Nrg, with median increase in elongation over the course of 48 hr exceeding 20% (Fig. 3.5). The average of the median elongation values in the Nrg-treated wells was 2.37 as opposed to 1.81 in the control wells. Examination of the original images, however, shows individual cells with elongation values above 4 or 5. As predicted, the MEK inhibitor completely abrogated Nrg-induced elongation. Importantly, when Nrg was not added, the MEK inhibitor had no effect on elongation. At higher doses, the PI3K and Src inhibitors likewise prevented Nrg-induced elongation. Although each of these inhibitors did reduce elongation when tested alone, these effects were much smaller than those observed when used with Nrg. In contrast, inhibiting MEK5 only partially decreased the elongation response to Nrg, and inhibiting p38 actually enhanced this response.

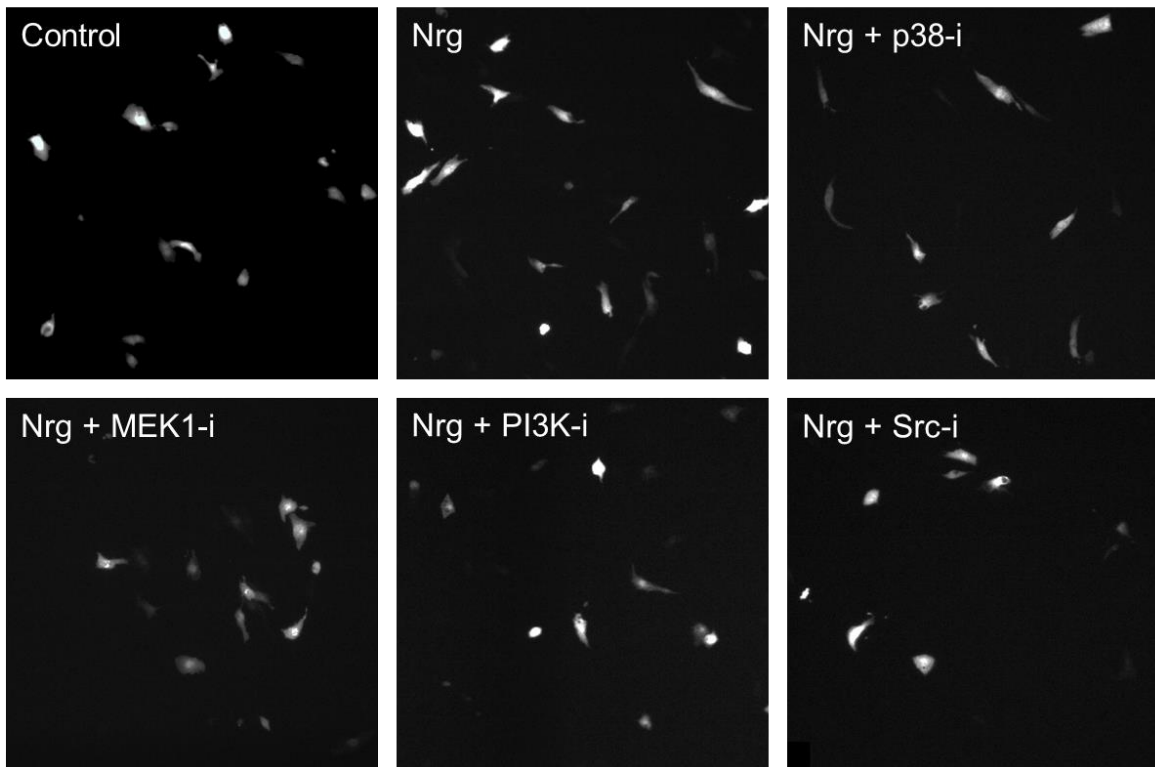
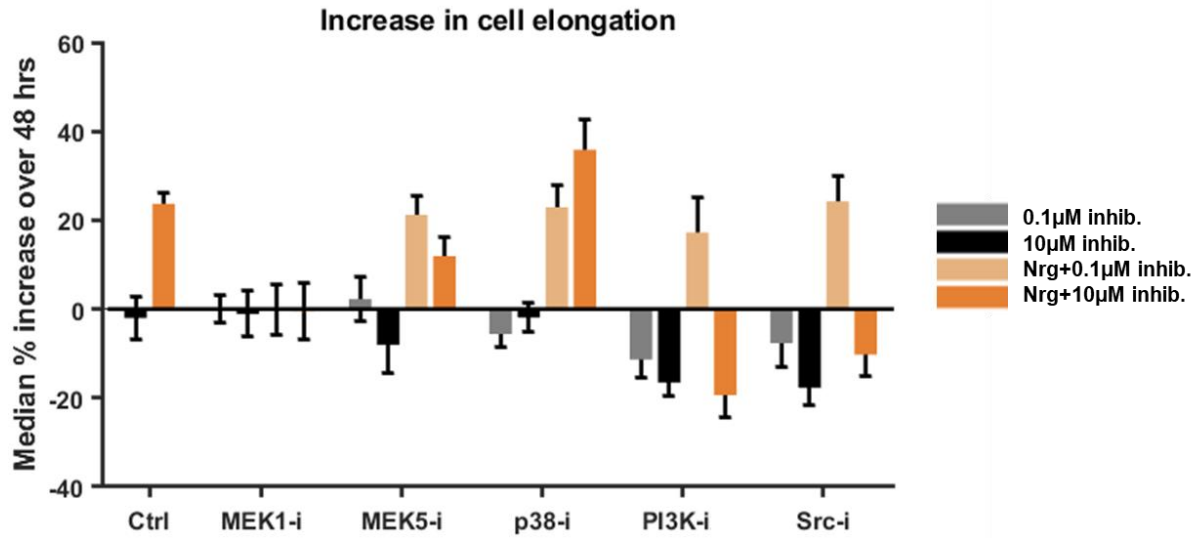


Figure 3.5. MEK1, PI3K, and Src mediate Nrg-induced elongation. Individual cells expressing GFP were tracked from before treatment to 48 hr post-treatment with Nrg and/or specified dose of indicated inhibitor. Within each well, the median change in elongation was calculated across all tracked cells (approximately 50 cells tracked per well). Values shown are averages of at least four wells for each condition, with bars showing standard error. Representative images shown (high inhibitor dose). Scale bar = 200 µm.

3.5. Discussion

3.5.1. *Observed protein activity concurs with prior studies*

The groups of proteins and phenotypes activated in response to the four ligands tested display internal consistency matching the canonical pathways associated with PI3K, MAPK, and pro-apoptotic signaling. Furthermore, the association of groups of proteins with specific stimuli accords with previous observations. Apoptotic proteins and PI3K-related proteins clustered toward opposite poles of the PLSR space, which made sense in light of the well-established cardioprotective role of the PI3K–Akt family [153], [154]. Likewise, CITED4, which promotes post-ischemic recovery and activates the mTOR pathway [155], projected close to phospho-mTOR and opposite the pro-apoptotic group. Both CITED4 and mTOR were strongly induced by Nrg.

Ang, which increased Bim and Bax in our myocytes, plays a key role in activating the apoptosis program of myocytes [156]. Clinical studies with losartan, an AT1R blocker, suggested that this pro-death behavior contributes toward cardiac apoptosis observed in the context of essential hypertension [157]. Interestingly, IGF was not observed to induce strong phosphorylation within the PI3K cascade, although IGF signaling through PI3K, PDK1, Akt, and GSK3 β is one of the most important initiators of physiological growth signaling in the heart [158]. This lack of response could merely be part of the attenuated response overall of our myocytes to IGF across the entire RPPA assay. Finally, the wide variation in GAPDH levels across conditions confirms previous observations that many common “housekeeping” proteins have limitations in their use as normalization controls [151].

3.5.2. *Regulation of Nrg-induced elongation by MEK1, PI3K, and Src*

Follow-up experiments validated our inference from the PLSR model that MEK1, PI3K, and Src each play a role in mediating Nrg-induced elongation. Our results agree with previous work finding that Nrg-induced elongation and formation of lamellipodia depends on Src and FAK activation downstream of erbB2 [35]. However, the elongation we observe is more unidimensional and creates an overall

lengthening of the cell, as opposed to the elongation of individual lamellipodia on all sides of the cell. Although the MEK1 inhibitor used alone exhibited no effect on cell elongation, both the PI3K and Src inhibitors caused mild decreases in elongation when tested alone. This behavior suggests the existence of some constitutively active process promoting elongation that acts both through PI3K and through Src. Although the study linking Nrg, FAK, and lamellipodia found FAK activation to be independent of the PI3K/Akt pathway, they do not report whether or not elongation was likewise independent. Previously, PI3K has been implicated in electrically-induced elongation [44], but this is the first time its influence over elongation in response to Nrg has been tested.

Past studies have found an important role for MEK5 in governing elongation induced through the gp130 receptor in response to LIF, IL-11, and CT-1 [30]–[33]. Since we observed little to no dependence on MEK5 for elongation in the context of Nrg, this suggests that the gp130–MEK5 pathway operates by a separate process from that downstream of Nrg. This independence makes sense in light of the implication of gp130 in inflammation, adverse remodeling, and ventricular rupture [159], in contrast with the importance of Nrg for maintenance of heart function and its mediation of reverse remodeling [160].

Interestingly, although we found MEK1 to promote eccentric growth, studies in adult mice and engineered heart tissue found MEK1 overexpression to govern concentric growth, and simultaneously noted ERK1/2 deletions to promote myocyte eccentricity [46]. These observations, however, were not made in the context of Nrg stimulation, which governs many other pathways operating in coordination with the MAPK cascade. It is also possible that in overexpression experiments, MEK1 could prompt phenotypes conflicting with its typical role at-physiological levels of expression. More work is needed to delineate the difference between MEK1 activity in these two contexts.

3.5.2. Limitations and future directions

Despite the identification of several proteins governing elongation in cardiomyocytes, the precise molecular mechanisms by which many of them promote concentric versus eccentric growth remain

unidentified [46]. More work needs to be done to connect individual stimuli and pathways to the intracellular regulatory units that control sarcomeric assembly. Furthermore, the role of crosstalk and feedback between the various elongation pathways remains unclear. The gp130–MEK5–ERK5 axis appears to be independent of Nrg–erbB2–FAK signaling, but other proteins, such as PKC ϵ , seem to be involved upstream of FAK as well [36].

Although some studies remove antibodies with a Pearson correlation coefficient of less than 0.5 between biological replicates [161], [162], we found that the PLSR was robust to inclusion of the full antibody set. Even antibodies with moderately low correlation coefficients grouped together, suggesting that noise in the data was reduced by averaging replicates. Nevertheless, further experiments could help clarify the role of proteins that displayed unexpected behavior, such as Bid and phospho-Bad appearing across from the main pro-apoptotic group. In addition, a larger RPPA panel would help illuminate the role of proteins, such as MEK5, that were not among the 172 tested here.

3.5.3. Conclusions

In this chapter, we integrated proteomic activity with downstream phenotypes to construct a model that connects hypertrophic stimuli, signaling cascades, and ultimate myocyte shape. MAPK and PI3K signaling activity downstream of Nrg was highly correlated with elongation, an association that was confirmed in additional experiments demonstrating that Nrg-induced elongation depends on MEK1 and on PI3K, as well as on Src. These results suggest an important role for these signaling hubs in mediating eccentric versus concentric forms of ventricular remodeling. More work is needed to identify the precise mechanisms by which these pathways regulate myocyte elongation.

Chapter 4

Novel drivers of cardiomyocyte remodeling from a genome-wide shRNA screen

The following individuals contributed to the work in this chapter: Philip M. Tan, Matthew W. van de Graaf, John C. Hulse, Jeffrey D. Molkentin, Jop H. van Berlo, and Jeffrey J. Saucerman.

Author contributions: P. M. Tan—conceptualization, image processing, data analysis, paper writing. M. W. van de Graaf—data analysis, paper writing. J. C. Hulse—data analysis. J. D. Molkentin—conceptualization, funding acquisition, supervision. J. H. van Berlo—conceptualization, funding acquisition, supervision, experiments. J. J. Saucerman—conceptualization, funding acquisition, supervision, paper editing.

4.1. Foreword

In chapters 2 and 3, we determined key regulators of stretch-induced hypertrophy, and identified signaling pathways differentially controlling distinct forms of remodeling. However, the scope of our discoveries was necessarily restricted to those genes and proteins included in our assays or examined in prior literature. We now broaden our focus to encompass the entire genome, identifying targets not previously implicated in myocyte growth and remodeling. Using automated image analysis on a shRNA screen comprising 97,500 conditions and millions of images, we discover hundreds of candidate genes that regulate area, elongation, and spikiness in cardiomyocytes.

4.2. Introduction

Although the heart displays a capacity to compensate by growing in response to stress, these changes are often insufficient to prevent subsequent cardiac events [163]. Patients suffering from heart failure need targeted therapies that promote beneficial remodeling and myocardial recovery. Current drugs aimed at suppressing or reversing hypertrophy block numerous signaling nodes within the cardiomyocyte, but pathway redundancy and side effects limit the effectiveness of existing therapies [164]. Moreover, our knowledge of the proteins and genes composing these pathways is far from complete. The discovery of novel regulators of myocyte size and shape could supply missing links in our efforts to map the signaling network in the heart, and would expand the range of potential therapeutic targets.

Recent developments in robotic cell culture and automated microscopy systems make it possible to test tens or hundreds of thousands of conditions in parallel [165]. However, the wealth of data such technologies generate far outstrip the capacity of researchers to process it, let alone glean insights from it, using manual techniques alone. Consequently, computational methods for image analysis have become increasingly vital [166]. Past studies have developed automated approaches for objectively quantifying multiple myocyte morphologies from immunofluorescence images [17], [107]. However, these efforts were limited to fewer than a hundred conditions, a scale at which manual inspection (if not quantification)

of the data is still feasible. The benefits of massive screens are accompanied by inevitable sources of variability due to the lack of direct human oversight and the need to break larger experiments into several separate batches. Furthermore, genome-scale experiments often test only a single replicate of each condition, making them more prone to false positives and thus necessitating secondary assays. Novel processing methods are necessary for translating terabyte-level raw data into meaningful conclusions with a high potential for replication.

Here, we developed a complete workflow for detecting conditions modulating cell size and shape in a genome-wide shRNA screen comprising 97,500 shRNAs targeting 15,000 different genes. Our image analysis pipeline identifies cell nuclei, separates myocytes from fibroblasts, distinguishes binucleated cells, determines cytoskeletal boundaries, and locates proliferating cells. In addition, we developed a robust filtering and normalization procedure to mitigate several types of artifacts. Implementing our workflow across 7 million images, we detected over 900 genes specifically regulating myocyte area, elongation, or spikiness. These included known drivers of cardiomyopathies, such as *Mybpc3* and *Dsp*, as well as scores of novel genes. By accomplishing in hours what would take years of manual work, our image analysis techniques accelerate the identification of prime targets for influencing cardiomyocyte morphology.

4.3. Methods

4.3.1. Cell culture

Timed mating was used in CD1 mice, and embryos were harvested with Worthington enzymes for cardiomyocyte isolation at E17.5. Enzymes were blocked with 15% FCS and cell culture was transitioned to 2% FCS afterwards. Isolated cells were pre-plated for one hour to enrich for cardiomyocytes. Cells were plated at a target density of 400 cells per well in 2% FCS on gelatin coated 384-well plates. Cardiomyocytes were treated with a lentivirus encoding either a mouse shRNA or a human cDNA targeting an individual gene in each well. shRNA knockdown was performed on over 15,000 genes and

cDNA over-expression was performed on over 11,000 genes. Within each plate, Myc adenovirus, sh002 lentivirus (scrambled shRNA), GATA adenovirus, and 10% FCS were included in fixed positions (O13–24 and P13–24) as control wells. All viruses were added immediately when cells were plated, and plates were allowed to settle at room temperature for one hour. Plates were then cultured using standard incubation conditions. Media was changed at 24 hours, and EdU (10 μ M) was added at 48 hours. At 72 hours, the cells were fixed in 4% PFA.

4.3.2. Microscopy

Images were taken with a Molecular Devices ImageXpress microscope using a 20x objective, with eighteen sites being imaged in each well. Channels included brightfield, DAPI, EdU (stained with Alexa 488), and troponin T (stained with Alexa 647). Image sizes were 1392 \times 1040, corresponding to dimensions of 0.449 \times 0.335 mm (0.323 μ m/pixel). Pixels were not binned.

4.3.3. Image processing

Image processing was performed using CellProfiler 2.1 [167], [168] and was implemented on Rivanna, the High-Performance Computing (HPC) system at the University of Virginia. The complete CellProfiler processing files are available upon request. Processing involved the following steps:

1. Image quality metrics were measured.
2. Background subtraction was performed based on the median percentile (for DAPI and EDU) or lower-quartile percentile (for troponin T) of each image.
3. To remove autofluorescing dead cells from the troponin T channel, pixels above the intensity of 0.8, together with a 15-pixel border surrounding them, were set to zero.
4. A complete nuclear image was obtained by adding DAPI and EdU channels (in the ratio 1.5:1), since some of the EdU-expressing cells were very faint in the DAPI channel.

5. Nuclei were identified using two-class adaptive Otsu thresholding with weighted variance minimization, shape-based division and an expected diameter of 20–80 pixels. An aggressive threshold correction factor of 5 was used in order to properly segment clumped nuclei. (Versions 3.0 and later of CellProfiler have a corrected Otsu algorithm that does not require the high correction factor.)
6. Nuclei were binned into myocytes or non-myocytes based on the lower-quartile intensity of the troponin T channel behind them, using a threshold of 0.002.
7. Adjoining myocyte nuclei were merged in order to unify binucleated cells.
8. Both myocytes and non-myocytes were binned into EdU⁺ or EdU⁻ based on the upper-quartile intensity of the EdU channel behind them, using a threshold of 0.03.
9. Myocyte cell bodies were identified by propagating from the myocyte nuclei with the watershed propagation method using two-class global Otsu thresholding with weighted variance minimization.
10. Object intensity and morphological features, such as area, elongation, and form factor, were measured and exported. The elongation of a cell body is similar to but distinct from its eccentricity; it is defined as the major axis divided by the minor axis, where the major and minor axes are those of an ellipse with the same normalized second central moments as the cell body. A perfectly circular cell thus has the minimum possible elongation of 1. The form factor, in turn, is a measure of the compactness of a cell body given its size, and equals $4\pi A/P^2$, where A is the area and P is the perimeter. Since form factor is a relatively unintuitive descriptor, after normalization we will deal with its inverse, which we refer to as the spikiness, S :

$$S = \frac{P^2}{4\pi A}$$

Cells with greater numbers of protrusions or with ruffled edges have a higher spikiness, whereas a perfectly circular cell has the minimum possible elongation of 1. Multiple replicates of a distinct shRNA for a given gene were averaged after filtering and normalization (see below) but before selecting hits.

4.3.4. Filtering and normalization

Wells generally displayed poor cell health or severe imaging artifacts if they had a total myocyte quantity of less than 100, or a correlation value of less than 0.1 in the troponin T channel. These wells were removed from consideration for all downstream steps.

Normalization occurred in two steps. First, we multiplied areas within each plate by a constant such that the median of all the wells within a plate was equivalent to the screen-wide median area (plate-level normalization). When calculating these medians, the 24 control wells on each plate were ignored. Next, for each batch of plates, we divided the areas of each well by the median area of all other wells within that batch occupying the same position on the plate (batch-level normalization). This procedure was completed in like fashion for each of the other metrics of interest, elongation and form factor.

4.3.5. Binomial model of off-target effects

The following model was developed from a version published by Sigoillot and King [169]. Consider a screen that comprises N genes, in which each gene is represented by A independent shRNAs. We assume that a given shRNA has on average M off-target mRNAs, and that these off-targets are random. Furthermore, we assume that the efficiency of the shRNA expression is E , such that in a fraction of the conditions equal to $1 - E$ no knockdown occurs. Last, let us assume that K is the number of genes in our pathway of interest—that is, the number of genes which when knocked down produce a phenotype interpreted as a positive result.

The probability that a given shRNA has a match that results in off-targeting for a specific mRNA out of N genes can then be defined as $m = E \times M \div N$. Now for each shRNA, let Y denote the number of genes out of the K genes in our pathway that have a match to that shRNA. If each of these K genes is independent of each other, then $P(Y)$ will follow the binomial distribution $B(K, m)$. Thus, the probability that a given shRNA does *not* match any of these K genes is given by

$$P(Y = 0) = C_{K,0} m^0 (1 - m)^{K-0}$$

and thus the probability that a given shRNA matches at least one of these K genes is $p = 1 - P(Y = 0)$.

We may then conclude that the probability that exactly $a = \{1: A\}$ shRNAs out of A independent shRNAs tested for a given gene in the overall screen will produce the phenotype due to off-target effects follows the binomial distribution

$$P(a_f) = C_{A,a} p^a (1 - p)^{A-a}$$

This implies that F_a , the estimated number of genes with exactly a out of A shRNAs giving the phenotype as a false positive (due to off-target effects), is $F_a = a_f \times N$. Likewise, the probability that exactly $a = \{1: A\}$ shRNAs for a given gene in the pathway will produce the phenotype due to knockdown of the correct mRNA follows the binomial distribution

$$P(a_t) = C_{A,a} E^a (1 - E)^{A-a}$$

This implies that T_a , the estimated number of genes with exactly a out of A shRNAs giving the phenotype as a true positive, is $T_a = a_t \times K$. The likelihood that a gene is a true positive, if exactly a out of its A shRNAs give the phenotype, must then be

$$\frac{T_a}{T_a + F_a}$$

To generate our predictions for parameter fitting, we set $N = 15000$ total genes, $A = 5$ independent shRNAs per gene, and $E = 0.4$ efficiency. Our estimate for E was based on examining EdU⁺ rates for

replicates of shRNAs targeting known inducers of proliferation: 41% (7 out of 17) of replicates across 10 distinct shRNAs targeting *Cdkn1a* and 40% (2 out of 5) of replicates across 5 distinct shRNAs targeting *Rbl1* had $\geq 5\%$ EdU⁺ myocytes. We then investigated values between 1 and 100 for M , the number of off-target mRNAs per shRNA, and for K , the total number of genes whose knockdown produces the phenotype of interest (in this case, high area). Predicted numbers of genes with $a = \{1:3\}$ positive shRNAs were compared with R_a , the actual number of observed hits, and mean relative error was calculated as

$$\varepsilon = \frac{1}{3} \sum_{a=1}^3 \frac{T_a + F_a - R_a}{R_a}$$

For the final predictions, we used values of $M = 50$ off-target mRNAs per shRNA and $K = 32$ genes in the pathway.

4.3.6. Gene set enrichment

For each metric of interest, the set of genes with two or more distinct shRNAs above threshold for was compared against five databases in Enrichr: KEGG 2017, WikiPathways 2017, GO Biological Process 2017, Human Phenotype Ontology, and OMIM Disease. For each database, the top 10 results were collected, and entries related to heart, muscle, or cytoskeleton were saved. Full results from Enrichr are available at the following locations:

Area: <http://amp.pharm.mssm.edu/Enrichr/enrich?dataset=3re0g>

Elongation: <http://amp.pharm.mssm.edu/Enrichr/enrich?dataset=3re0k>

Form factor: <http://amp.pharm.mssm.edu/Enrichr/enrich?dataset=3re0m>

4.4. Results

4.4.1. Image processing algorithms identify distinct myocyte morphologies

We previously developed automated methods for morphological analysis of neonatal rat cardiomyocytes [107]. Here, we extended these techniques (Fig. 4.1) and applied them to a genome-wide shRNA screen that tested 97,500 shRNAs targeting 21,000 different genes in mouse embryonic cardiomyocytes. First, we performed background subtraction based on the median percentile (for DAPI and EDU) or first-quartile percentile (for troponin T) of each image. We eliminated autofluorescing dead cells from the troponin T channel by setting pixels at an extremely high intensity to zero, together with a 15-pixel border surrounding them. A complete nuclear image was obtained by adding DAPI and EdU channels, since some of the EdU-expressing cells were very faint in the DAPI channel. Nuclei were identified with two-class adaptive Otsu thresholding, using an aggressive threshold correction factor in order to properly segment clumped nuclei (Fig. 4.2A). Nuclei were binned into myocytes or non-myocytes based on the lower-quartile intensity of the troponin T channel behind them (Fig. 4.2B), and adjoining myocyte nuclei were merged in order to unify binucleated cells (Fig. 4.2C). Both myocytes and non-myocytes were then binned into EdU⁺ or EdU⁻ based on the upper-quartile intensity of the EdU channel behind them. Finally, myocyte cell bodies were identified by propagating from the myocyte nuclei with the watershed propagation method using two-class global Otsu thresholding (Fig. 4.2D).

4.4.2. Myocyte quantity and image correlation provide quality control metrics

Due to the massive scope of the screen, it was essential to develop automated methods for filtering out conditions with subpar cell health or poor image quality. We hypothesized that myocyte quantity would serve as a simple proxy for overall cell health; moreover, morphological measurements from wells with fewer myocytes would be less reliable in the first place due to small sample size. Indeed, sorting conditions by the total number of myocytes present revealed much higher variance and a steep overall dropoff in cell area at myocyte counts below 100 (Fig. 4.3A, left).

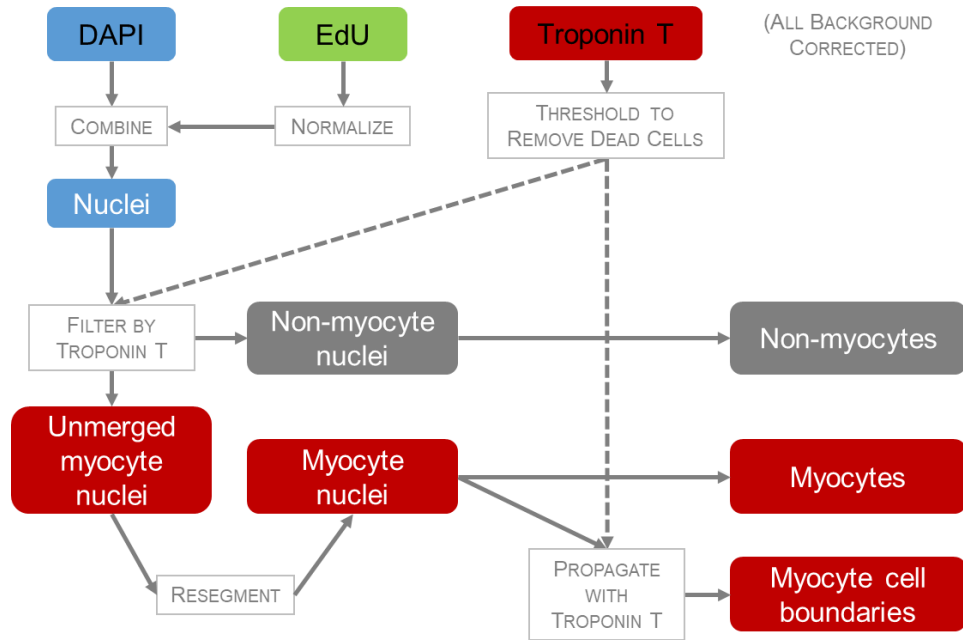


Figure 4.1. Schematic of image processing algorithm for myocyte identification.

First, background subtraction is performed based on a median or first-quartile percentile for each image. Autofluorescing dead cells are eliminated from the troponin T channel by setting blocking out regions with extremely high intensities. The DAPI and EdU channels are then combined, since some cells are only visible in one or the other, and nuclei are identified by Otsu thresholding. Nuclei are binned into myocytes or non-myocytes based on the troponin T channel behind them, and adjoining myocyte nuclei are merged in order to unify binucleated cells. Finally, myocyte cell bodies are identified by propagating from the myocyte nuclei with the watershed method using Otsu thresholding.

We also needed an objective criterion for discarding wells with failed staining in the troponin T channel or with shutter problems causing other channels (especially brightfield) to appear overlaid with the troponin T channel. One common feature uniting these problematic images was their grainy texture, whether due to scattered antibody particles or to erroneously overlapping channels. To filter out these images, we used the “correlation” feature developed by Haralick from the co-occurrence metric [170], which measures local self-similarity. As with myocyte quantity, sorting conditions by image correlation in the troponin T channel showed a sharp decline in calculated cell area at correlation values below 0.1 (Fig. 4.3A, right).

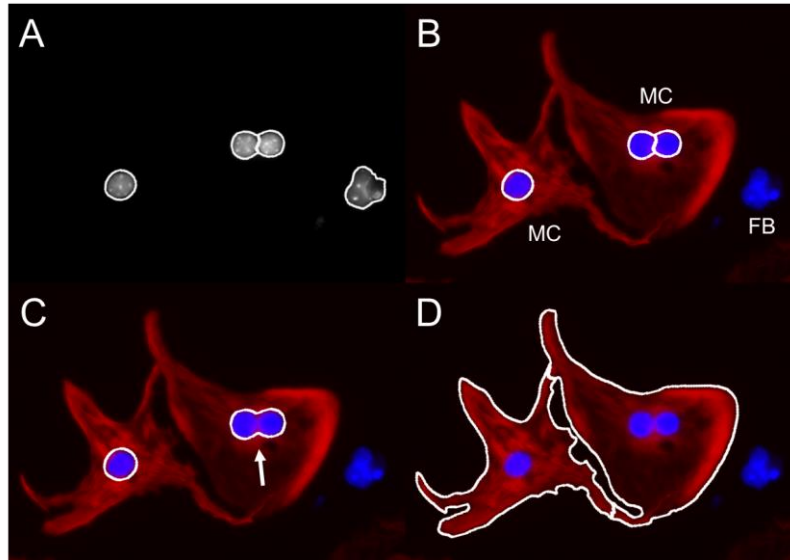


Figure 4.2. Automated image analysis identifies myocytes and quantifies cell boundaries. (A) Identification of nuclei in DAPI channel. (B) Sorting of nuclei into myocytes (MC) and fibroblasts (FB) based on intensity of troponin T behind them. (C) Merging of adjoining myocyte nuclei in order to unify binucleated cells. (D) Identification of myocyte cell bodies by propagating from the myocyte nuclei in the troponin T channel. From Plate 30, well F11, site 9.

Importantly, while subsequent normalization steps (see section 4.4.3) stabilized cell areas across most values, areas remained dramatically lower within wells with low cell quantity or low troponin T correlation (Fig. 4.2B). To confirm our subjective impression that these were appropriate quality control thresholds, we returned to the original pre-normalized areas and performed a two-sample t -test for each bin, evaluating the null hypothesis that the areas in each bin and the areas from the entire screen come from distributions with equal means (Fig. 4.3C). As expected, p -values remained relatively large across most values, but declined precipitously below the quality control thresholds. Given these results, we eliminated all wells with fewer than 100 myocytes or with a troponin T correlation below 0.1, and proceeded to data normalization.

4.4.3. Two-step normalization corrects plate-level variation and eliminates regional artifacts

Because cell culture and imaging for the screen was carried out in several batches over multiple weeks, small variations in cell size occurred from one batch to the next. Ideally, wells with the control

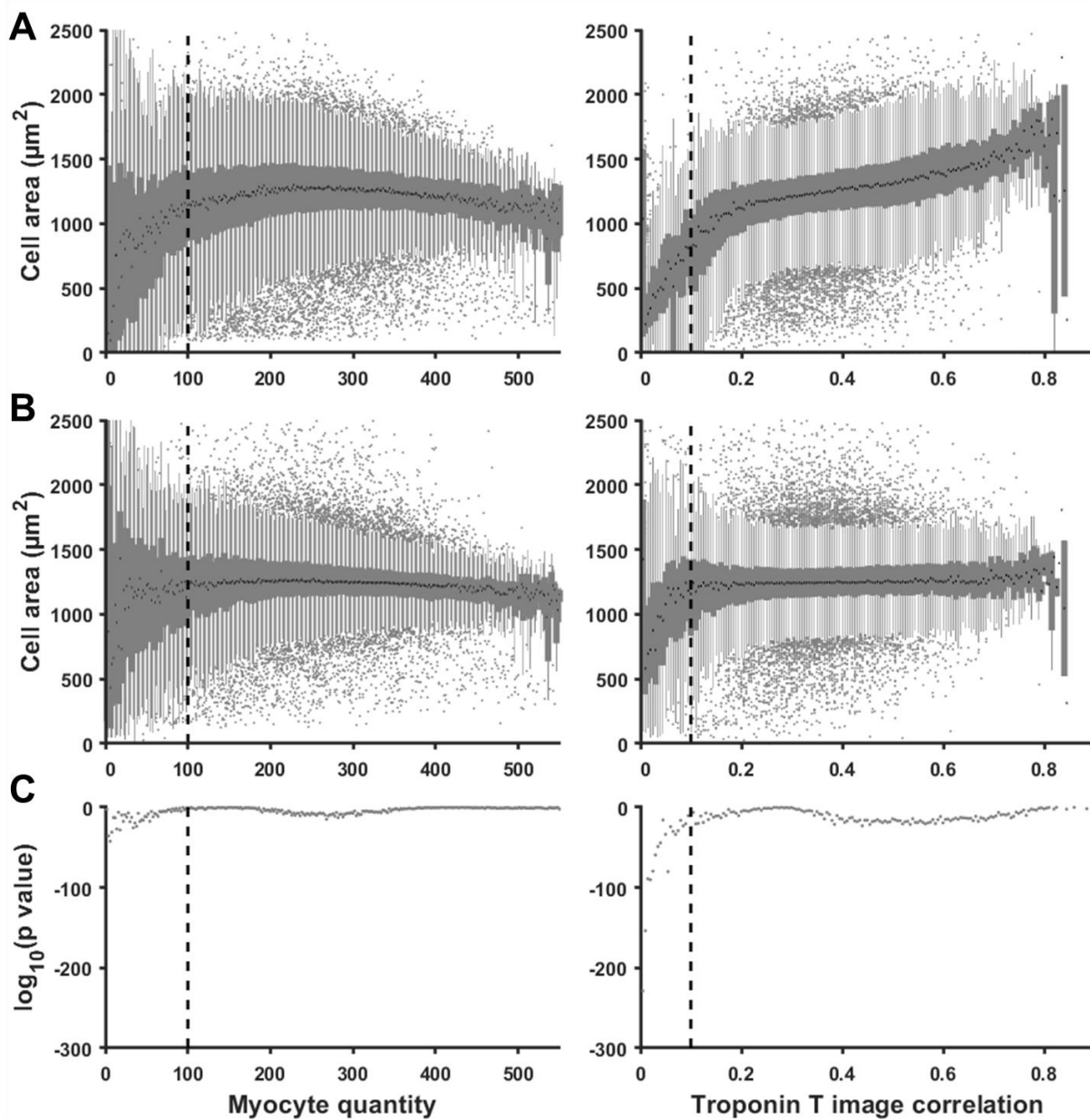


Figure 4.3. Filtering by myocyte quantity and image noise removes conditions with abnormal cell health or imaging errors. (A) Measured myocyte cell areas (pre-normalized values) decline with low cell counts or low image correlation (a measure of regional self-similarity) in the troponin T channel. Bin width = 2 for myocyte quantity and 0.005 for image correlation. For each bin, box plots show 25th, 50th, and 75th percentile values for wells within the bin, along with whiskers extending up to 1.5 times beyond the width of the interquartile range, and outliers. Dashed lines indicate threshold below which wells are eliminated. (B) Same as (A), but with normalized values. Normalization is insufficient to stabilize wells below thresholds. (C) Significance of two-sample *t*-tests for each bin (pre-normalized values) evaluating the null hypothesis that the areas in each bin and the areas from the entire screen come from distributions with equal means.

conditions could be used for normalization. However, these control wells were always located along the edge of each plate, and thus were highly susceptible to edge artifacts. In addition, within each batch, plates often displayed regional variation in area from one side of the plate to the other, presumably due to minor differences in temperature or air composition within the incubators. In other batches, plates displayed a “checkerboarding” effect with variations in area in every other well, caused by blockages or inadequate mixing in the robotic liquid handling and imaging system, coupled with its pattern of traversing the plate.

To correct for these artifacts, we developed a robust two-stage normalization scheme (Fig. 4.4). First, we multiplied areas within each plate by a constant such that the median of all the wells within a plate was equivalent to the screen-wide median area (plate-level normalization). This step ensured that plates with higher overall cell health were not given an unfair advantage. Next, for each batch of plates, we normalized the areas of each well against the median area of all other wells within that batch occupying the same position on the plate (batch-level normalization). This step mitigated edge effects, gradients across plates, and checkerboarding within each batch. The entire normalization process was repeated for each of the other metrics under consideration, elongation and form factor.

Visualizing values for each morphological metric across all plates in the screen before and after normalization confirmed relative uniformity not only in medians, but also in lower and upper quartiles (Figs. 4.5–4.7). Significantly, hits identified in subsequent steps (see section 4.4.4) were evenly dispersed across the screen, rather than biased toward a small number of plates and batches as they would have been before normalization. Having normalized the data, we established a threshold at the 95th percentile for area and elongation, and at the 5th percentile for form factor (that is, the 95th percentile for spikiness). Of the three metrics, elongation displayed the lowest range: the ratios of the 95th percentile to the median for area ($1,579 \mu\text{m}^2$ to $1,253 \mu\text{m}^2 = 1.26$) and for spikiness (7.86 to $6.13 = 1.28$) were much higher than that for elongation (2.12 to $1.99 = 1.07$). When more than one replicate of a distinct shRNA for a given gene

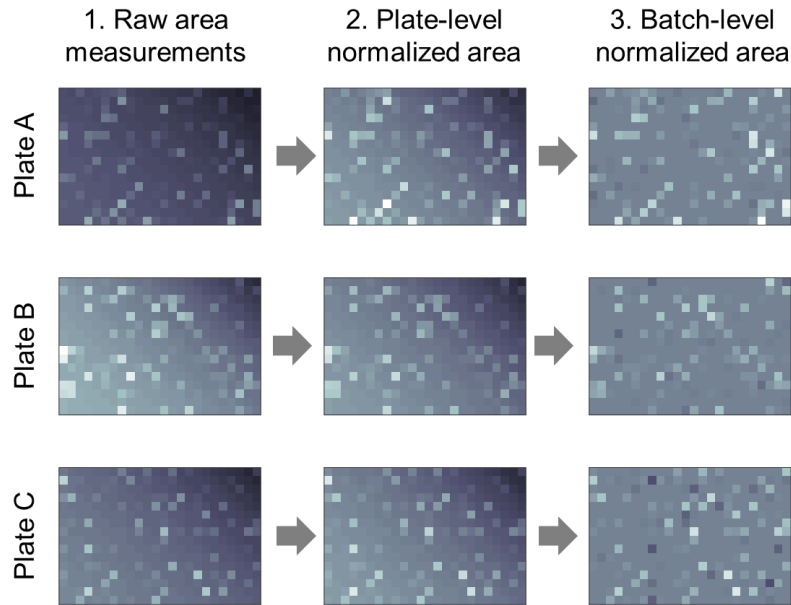
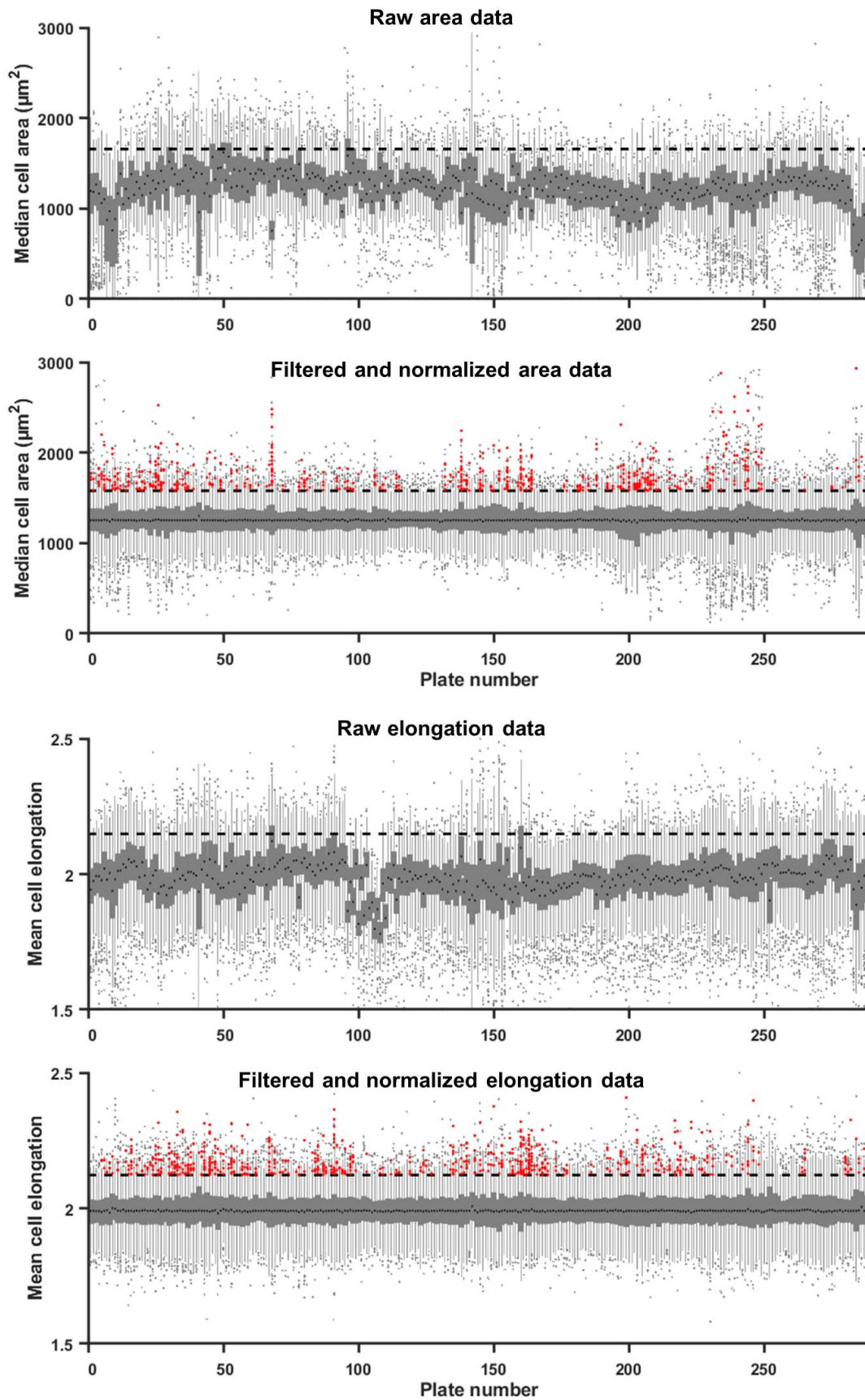


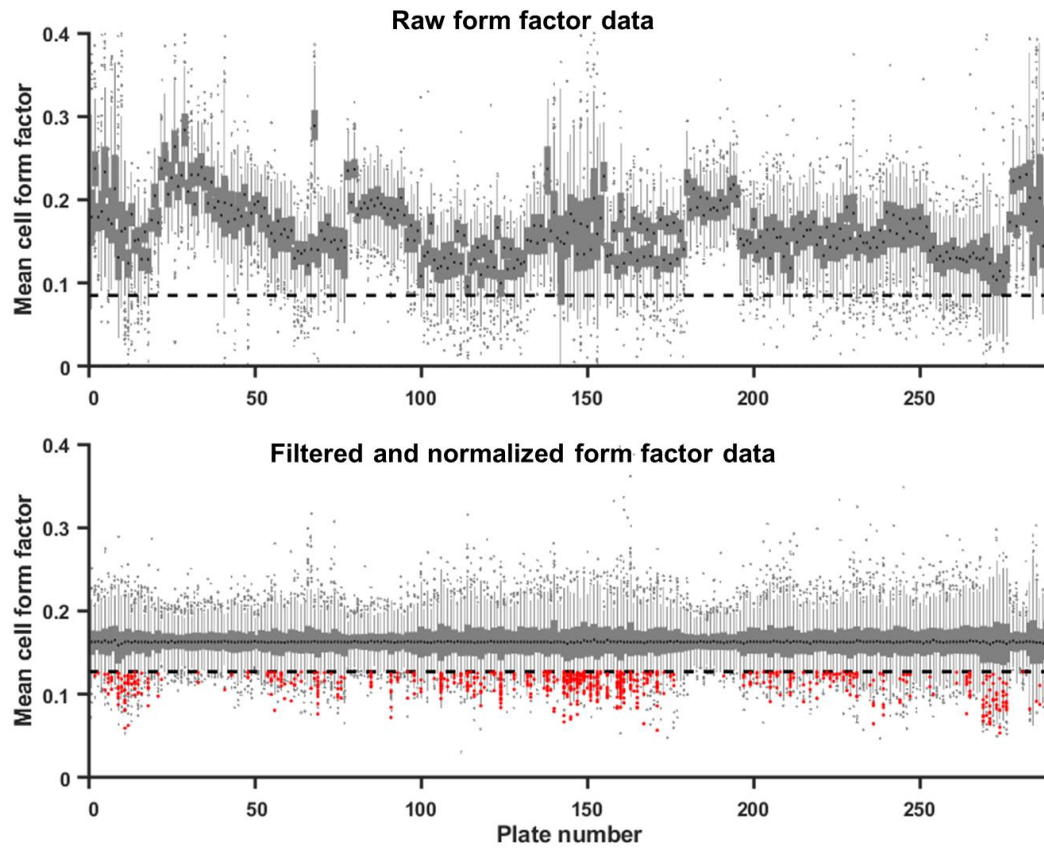
Figure 4.4. Two-step normalization corrects for plate-level variation and eliminates regional artifacts. In step 1, each plate is multiplied by a constant so that the median of all the wells on that plate is identical to the overall screen median. In step 2, for each batch of plates, each well is normalized against the median of all other wells within the batch occupying the same position on the plate in order to correct for regional variation. Simulated data used to facilitate comparison.

Figure 4.5. Two-step normalization stabilizes area values across screen. The 289 shRNA plates from the screen are ordered by plate ID. For each 384-well plate, box plots show 25th, 50th, and 75th percentile values of median cell area for wells within the plate, along with whiskers extending up to 1.5 times beyond the width of the interquartile range, and outliers. Dashed line indicates the 95th percentile for the overall screen, the threshold for identifying shRNAs as hits. Red markers indicate wells from genes with two or more shRNAs above threshold ($1,579 \mu\text{m}^2$ after normalization). Plate medians in lower plot vary slightly from each other due to presence of control wells, which were ignored during normalization.

Figure 4.6. Two-step normalization stabilizes elongation values across screen. Mean elongation within wells is displayed. Dashed line indicates the 95th percentile threshold (2.12 after normalization).

Figure 4.7. Two-step normalization stabilizes form factor values across screen. Mean form factor within wells is displayed. Dashed line indicates the 5th percentile threshold (0.127 after normalization, equivalent to a spikiness of 7.86).





occurred, we averaged the morphological values for those replicates before determining which shRNAs were above threshold.

4.4.4. Multiple shRNAs above threshold per gene are necessary to identify hits

A major concern when using RNA interference is the possibility of off-target effects [171]. It is highly common for the majority of the top hits in a screen to act not by knocking down their intended targets, but rather by nonspecific targeting of other mRNAs, including those already known to be regulating the phenotype of interest [172], [173]. Indeed, when this screen was evaluated for its original purpose—identifying regulators of proliferations—the shRNA causing the highest rates of EdU⁺ myocytes was found to be achieving this through nonspecific targeting (unpublished data, Molkenin lab). Moreover, since a certain level of heterogeneity in myocyte morphology between conditions will occur

even without any perturbations, it is possible that the top hits from a screen could represent nothing more than natural variability without any biological significance.

These concerns prompted us to assess whether the lists of top shRNAs for each morphology displayed any differences from those expected from an equivalent but randomly structured data set. If a specific gene negatively regulates hypertrophy, for example, we would expect each of the shRNAs targeting that gene to produce myocytes with higher area. In contrast, in the case of a single gene having nothing to do with hypertrophy, it would be highly unlikely for multiple distinct shRNAs from this gene to all have off-target effects producing higher area. In other words, if our screen has identified true regulators of hypertrophy, we expect a higher number of genes to have multiple shRNAs above threshold than if the results observed were solely due to natural variation or to off-target effects. As hoped, upon randomly shuffling the identifying shRNA labels among all the wells in the screen, we find significantly fewer genes with 2 or more shRNAs above threshold for area than were actually observed in the screen (Fig. 4.8A). This enrichment of replicating shRNAs is even more pronounced when evaluating the results for elongation or for spikiness (data not shown). These comparisons lend confidence that for many of the genes with multiple clones above threshold, the exaggerated morphologies observed are actually due to on-target effects.

To obtain an alternative estimate of the true positive rates in our screen, we adapted a previously published binomial model by Sigoillot and King that calculates the frequency of on-target and off-target genes that would be discovered in a screen [169]. Our model included the following parameters: N , the total number of genes in the screen; A , the number of distinct shRNAs per gene; M , the number of off-target mRNAs per shRNA, and K , the actual number of genes in the pathway of interest. We also added a new variable E , the likelihood that the desired shRNA is actually produced in the first place, to account for less-than-perfect efficiency in shRNA expression. Among these variables, M (the off-target rate) and K (the pathway size) are the hardest to directly measure. Sigoillot and King test several values for K , and estimate $M = 50$ based on several prior studies that observed values between 30 and 100 [174]–[178]. In

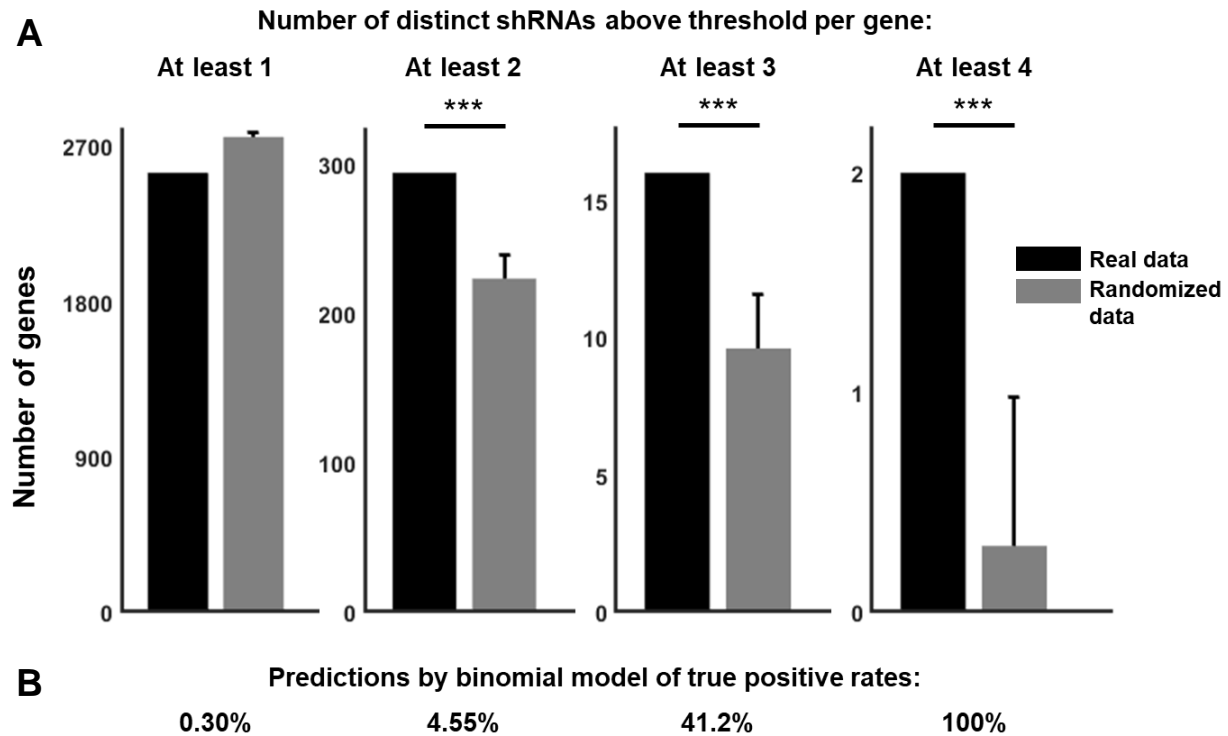


Figure 4.8. Significantly high numbers of genes have multiple shRNAs above threshold. (A) Screen contains more genes with multiple shRNAs above area threshold than would be expected in a screen with equivalent data but with shRNA IDs randomly shuffled among the wells. Bars for randomized data show mean and standard deviation of 10 iterations of random shuffling; ***, *t*-test gives $p < 0.0001$. (B) Predictions by the binomial model of what percentage of genes in each category are true positives, as opposed to the result of off-target effects.

our model, we set constant values for N , A , and E , and tested a broad range of values for K and M against our observed results (Fig. 4.9). Although parameter fitting narrowed the possible range of values for K and M , there was not a unique optimum for K and M , as a high number of pairs produced a good fit. Ultimately, we used Sigoillot and King's estimate of $M = 50$ off-target mRNAs per shRNA, and selected the corresponding value of $K = 32$ genes in the pathway that best minimized the error.

The model's prediction of the occurrence of true versus false positives in our screen confirmed that multiple distinct shRNAs above threshold are necessary to obtain confidence in a reported hit (Fig. 4.8B). When a gene has at least two shRNAs above threshold, the model predicts a 5% likelihood of its being a true positive; this probability rises to close to 50% when there are at least three shRNAs, and becomes

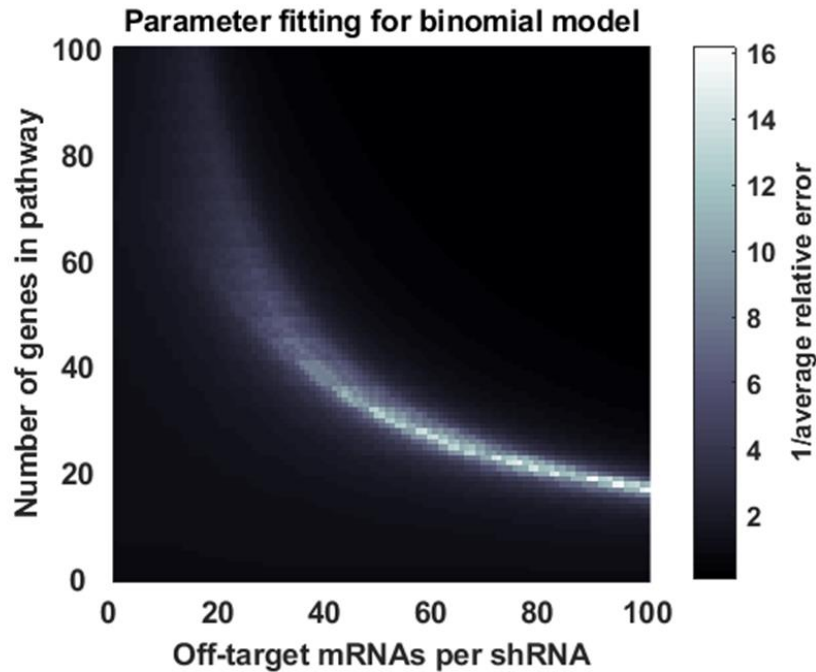


Figure 4.9. Parameter fitting for off-target rate and pathway size in binomial model. Model predictions of how many genes with 0 to 5 shRNAs above area threshold were compared with actual results from screen. Band with low error continues indefinitely off the right side of the plot. Red box indicates values used in final model (off-target rate = 50; pathway size = 32 genes).

virtually certain with four or five clones. In contrast, when only one shRNA scores above threshold, the model predicts the likelihood of a true positive being less than one-third of one percent. Testing a broader range of K and M values did not change this overall pattern (data not shown). Thus, for each morphological characteristic under consideration, we narrowed all subsequent analysis to consider only those genes with at least 2 out of 5 shRNAs above the 95th percentile threshold.

4.4.5. Manual verification confirms identification of distinct hypertrophic morphologies

After narrowing the lists of candidate genes to those with multiple shRNAs above threshold, the resulting gene sets represented a manageable 10–15% of the full list of hits: 294 out of 2,547 genes for high area, 360 out of 3,035 genes for high elongation, and 345 out of 2,391 genes for high spikiness. Several genes scored positively for more than one metric (Fig. 4.10): 10 for area and elongation, 11 for

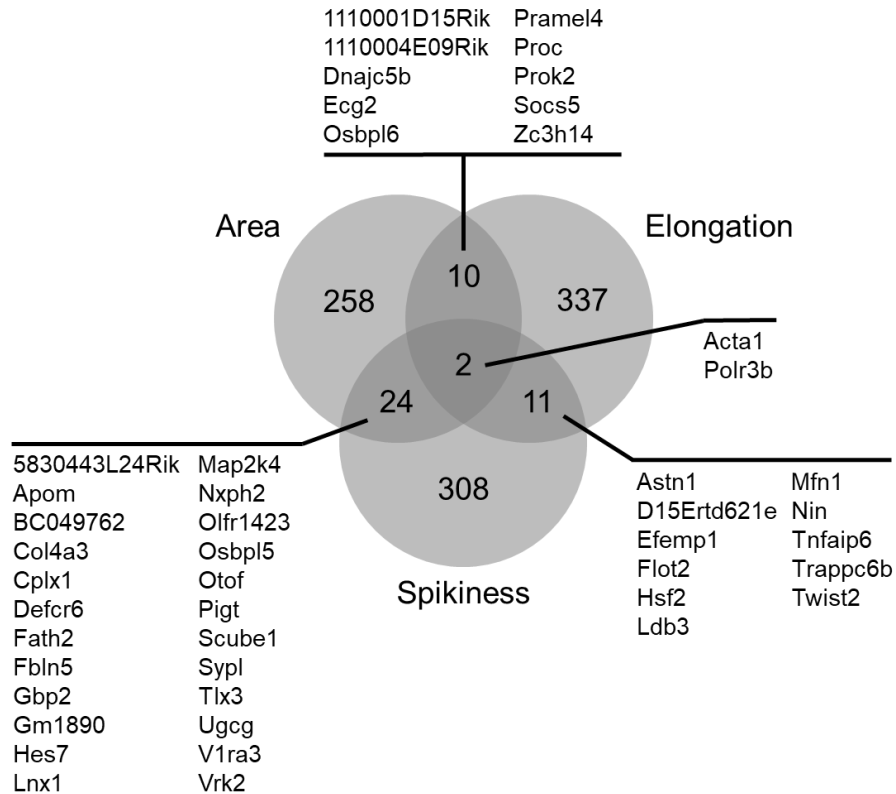


Figure 4.10. Overlap between top genes for area, elongation, and spikiness. Number of genes with two or more distinct shRNAs above threshold for one or more morphological metrics are listed.

elongation and spikiness, and 24 for area and spikiness. In addition, two genes, *Acta1* and *Polr3b*, scored positive for all three metrics. Though not extremely large, this overlap is more than would be expected from a random distribution of hits, which would be expected to produce 5–7 overlapping genes between each pair of categories. The complete gene sets for area, elongation, and spikiness are reported in Appendices E, F, and G, respectively.

Manual inspection of images from shRNA treatments confirmed the expected morphological phenotypes (Fig. 4.11). For all three categories, individual cells often displayed morphologies many times more extreme than the 95th percentile threshold or even than the mean or median for their well. For example, none of the *Ttn* clones produced wells with median cell areas greater than 2,000 μm^2 , but

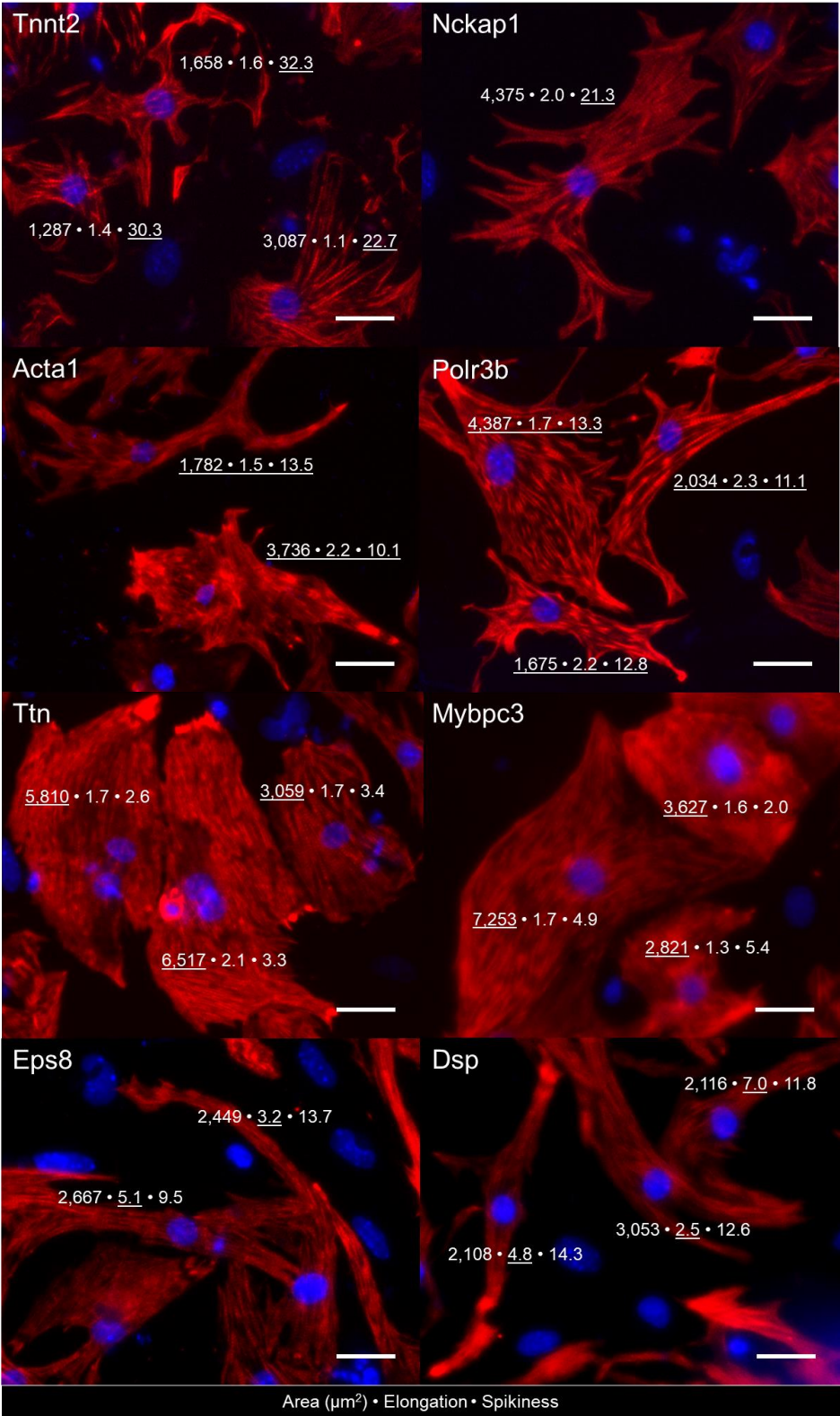


Figure 4.11. Hits identified display expected morphologies. Representative images are shown for conditions with high area (*Ttn* and *Mybpc3*), high elongation (*Eps8* and *Dsp*), high spikiness (*Tnnt2* and *Nckap1*), or all three (*Acta1* and *Polr3b*). Morphological values are listed for individual cells, with the morphologies of interest underlined; customized versions of the analysis pipeline were used to ensure high accuracy. Cells are stained for DAPI (blue) and troponin T (red). Scale bar = 25 μ m. Original image locations: *Ttn*—Plate 93, well A15, site 4. *Mybpc3*—Plate 145, well C22, site 17. *Eps8*—Plate 233, well F10, site 4. *Dsp*—Plate 249, well N21, site 7. *Tnnt2*—Plate 165, well E13, site 4. *Nckap1*—Plate 153, well E03, site 7. *Acta1*—Plate 229, well A23, site 18. *Polr3b*—Plate 150, well F04, site 5.

several individual cells were over 5,000 μm^2 in size, more than three times above the screen-wide threshold. Likewise, although the mean cell elongation for a well rarely exceeded 2.2 even among the hits, individual cells displayed dramatic major to minor axis ratios exceeding 12. Perimeter to area ratios were just as extreme, with cells possessing spikiness values in excess of 30, four times greater than the screen-wide threshold.

Within the genes identified as hits for each morphology, the actual phenotypes were by no means uniform. For example, although the *Ttn* and *Mybpc3* knockdowns produced comparably high cell area, the *Ttn* shRNA-treated myocytes display unusually prominent focal adhesions that are absent from *Mybpc3*, where the cells have much less pronounced ends. Among the *Ttn* myocytes are also an unusually high number of binucleated cells, which is not the case with *Mybpc3*. Similar variation appears among highly elongated cells: Some appear to be long due to concentrated growth at the poles, while others seem merely emaciated. When considering genes inducing high spikiness, it is evident that completely different processes are at work even in cells with very similar morphological scores. In the case of *Nckap1*, for instance, the increased perimeter is clearly due to intense lamellipodium formation on all sides of the cell. Sarcomeres are highly organized and are oriented perpendicularly within each individual projection. With the *Tnnt2* cells, on the other hand, the spikiness seems to be caused not by growth, but rather due to a general collapse of the cytoskeleton. Rows of sarcomeres appear jumbled, often crossing each other at right angles.

4.4.6. Enrichment analysis identifies overrepresented signaling pathways

Gene set enrichment analysis is a powerful tool for extracting biological insight from lists of genes [179]. Having manually confirmed the presence of high area, elongation, and spikiness in response to knockdown of individual genes, we pursued a systems-level perspective on our finding using Enrichr, a comprehensive search engine encompassing signaling pathways, gene ontologies, and diseases, among other gene set libraries [180], [181]. The top ten enriched terms from five databases were investigated: KEGG, WikiPathways, GO Biological Process, Human Phenotype Ontology, and OMIM Disease. Gene sets for all three morphologies were highly enriched for multiple terms associated with cardiac development, structure, and disease (Tables 4.1–4.3).

Area				ADCY8	PRKACA	ITGB8	MYBPC3	DES	TTN	ACTA1	MYL1	ANKRD2
Database	Enriched term	-log(p value)										
KEGG	dilated cardiomyopathy, <i>H. sapiens</i>	2.7										
	hypertrophic cardiomyopathy, <i>H. sapiens</i>	1.5										
WikiPathways	striated muscle contraction, <i>M. musculus</i>	3.5										
	striated muscle contraction, <i>H. sapiens</i>	3.7										
GO Biological Process	muscle filament sliding	3.7										
	muscle contraction	2.1										
Human Phenotype Ontology	EMG: myopathic abnormalities	2.2										
	centrally nucleated skeletal muscle fibers	2.0										
	dilated cardiomyopathy	1.8										
OMIM Disease	dilated cardiomyopathy	1.9										
	cardiomyopathy	1.6										
	myopathy	1.6										
	hypertrophic cardiomyopathy	1.6										
	muscular dystrophy	0.4										

Table 4.1. Cardiac function and disease are highly enriched in conditions with high area. The set of genes with two or more distinct shRNAs above threshold for area was compared against five databases in Enrichr. Terms from the top 10 results from each database related to heart, muscle, or cytoskeleton are listed along with significance and the overlapping genes.

Table 4.2. Cardiac function and disease are highly enriched in conditions with high elongation. Enriched terms from the set of genes with two or more distinct shRNAs above threshold for elongation.

Table 4.3. Cardiac function and disease are highly enriched in conditions with high spikiness. Enriched terms from the set of genes with two or more distinct shRNAs above threshold for spikiness.

Elongation

Database	Enriched term	$-\log(p \text{ value})$
KEGG	arrhythmogenic right ventricular cardiomyopathy, <i>H. sapiens</i>	0.8
GO Biological Process	regulation of ventricular cardiac muscle cell action potential	1.8
	barbed-end actin filament capping	2.2
	actin filament bundle assembly	1.9
H. Phen. Ont.	congestive heart failure	2.1
OMIM Disease	myopathy	1.4
	dilated cardiomyopathy	0.9
	cardiomyopathy	0.8

Spikiness

Database	Enriched term	$-\log(p \text{ value})$
KEGG	adrenergic signaling in cardiomyocytes, <i>H. sapiens</i>	2.4
	dilated cardiomyopathy, <i>H. sapiens</i>	2.3
	cardiac muscle contraction, <i>H. sapiens</i>	1.9
	hypertrophic cardiomyopathy, <i>H. sapiens</i>	1.8
	regulation of actin cytoskeleton, <i>H. sapiens</i>	1.5
WikiPathways	regulation of actin cytoskeleton, <i>H. sapiens</i>	2.3
	regulation of actin cytoskeleton, <i>M. musculus</i>	2.4
	striated muscle contraction, <i>H. sapiens</i>	2.4
	striated muscle contraction, <i>M. musculus</i>	2.3
GO Biological Process	ventricular cardiac muscle tissue morphogenesis	4.8
	muscle contraction	3.2
	regulation of heart contraction	3.0
	cardiac muscle contraction	2.6
H. Phen. Ont.	congestive heart failure	4.1
OMIM Disease	hypertrophic cardiomyopathy	3.8
	cardiomyopathy	3.1
	dilated cardiomyopathy	2.6
	myopathy	2.2

Some terms, such as “myopathy”, “cardiomyopathy”, and “dilated cardiomyopathy” appeared for all three morphologies and across multiple databases, though in each case thanks to different genes. Other terms were only associated at high significance with a single phenotype, such as “centrally nucleated skeletal muscle fibers” (area), “regulation of ventricular cardiac muscle cell action potential” (elongation), or “adrenergic signaling in cardiomyocytes” (spikiness). Of the three morphologies, elongation received fewer cardiac-related matching terms, which generally appeared with a lower significance. This may be due to the lower overall variation in elongation as a metric, as was previously noted.

4.5. Discussion

4.5.1. *A genome-wide index of myocyte morphologies*

Our analysis pipeline successfully characterizes genetic influence on myocyte shape across the entire genome. The prevalence of terms related to heart failure in the gene set enrichment analysis, such as congestive heart failure, hypertrophic cardiomyopathy, and dilated cardiomyopathy, confirms that the heightened phenotypes observed bear clinical relevance. Importantly, enrichment of gene lists from slightly varying analysis workflows indicated that many other relevant genes are just below the 95th percentile threshold chosen. For example, if the median elongation per well is examined instead of the mean elongation, or if elongation is calculated at the well level instead of at the cell level—that is, dividing the mean major axis by the mean minor axis for the well—a host of other genes appears with membership in the same enriched categories.

Importantly, we observed that when performing gene enrichment with the full sets of genes with as few as one shRNA above threshold, dramatically fewer terms appeared relevant to the myocardium or cytoskeleton. This difference provided a qualitative validation of our model prediction that multiple distinct shRNAs are necessary to achieve a high true positive rate among the selected genes. Likewise, performing gene enrichment without the indicated filtering and normalization procedures produced similarly desultory enrichment results, highlighting the importance of these steps to proper analysis.

4.5.2. *Clinical significance of genes influencing myocyte remodeling*

Many of the morphological patterns observed concord with the published literature on individual genes. *Nckap1* (also known as *Nap1*), for instance, encodes Nck-associated protein 1, a regulatory component of the WAVE complex mediating actin remodeling and particularly formation of lamellipodia [182], [183]. *Nckap1* mutants have been linked to specific cardiac morphogenetic defects such as cardia bifida, the failure to form a single heart tube [184]. Curiously, although each of these studies have indicated that lamellipodia activity requires *Nckap1*, here we observe its knockdown to produce the same result. *Tnnt2*, which encodes cardiac troponin T, is crucial for muscle contraction, and *Tnnt2* mutations are a frequent cause of dilated or hypertrophic cardiomyopathies [185], [186]. As an integral component of the thin filament, its disruption is disastrous to sarcomere maintenance [187]. Of course, since we used troponin T as our cytoskeletal stain in this screen in the first place, it is unsurprising that its deletion would stand out—though the presence of some staining may indicate that the knockdown was partial. Although both *Nckap1* and *Tnnt2* stood out because of high spikiness, the underlying cellular processes driving their phenotypes are obviously quite different. Integrating algorithms for measuring sarcomere organization could enable automated differentiation of whether the spikiness is being caused by organized growth or by cytoskeletal collapse [188].

Among the genes identified regulating cellular elongation, *Dsp*, encoding the protein desmoplakin, has been found to play an important role in linking the cytoskeletal network to the plasma membrane in the heart [189]. In transgenic mice with subjected to exercise, desmoplakin mutants displayed disruption of the intercalated disks, intermediate filaments, and microtubules, and wall thinning and dilation of the right ventricles was observed [190]. *Eps8*, which encodes epidermal growth factor receptor pathway substrate 8, is known as an actin bundling and capping protein that mediates bleb formation [191]. The protein, which interacts with the ankyrin repeat protein VAB-19, has been shown to be essential for *C. elegans* epidermal elongation [192]. As with *Nckap1*, so with *Eps8* we note paradoxical activity in which gene knockdown accomplishes the phenotype for which the gene is previously reported to be essential.

Similarly, *Ttn* (titin) and *Mybpc3* (cardiac myosin-binding protein C), which were associated with dramatic area changes in our screen, are both known as critical players in cardiac pathophysiology [193], [194]. Mutations truncating titin are the most frequent genetic cause of dilated cardiomyopathy [195], and mutant titin produces cardiomyocytes with impaired contractile performance and disrupted responses to mechanical and β -adrenergic stress [196]. In response to transverse aortic constriction, mice with a heterozygous *Mybpc3* mutation showed increased hypertrophy and reduced ejection fraction compared to wild-type mice [197]. In fact, *Mybpc3* mutations are responsible for about 40% of cases of hypertrophic cardiomyopathy [198]. The ability of our pipeline to isolate these genes with a known role in cardiac disease lends confidence that the others identified may have similar clinical relevance.

4.5.3. Advantages and shortcomings of segmentation-based image analysis

Recent years have witnessed impressive performance by machine learning approaches to analysis of microscopy data [199]. However, their algorithms often constitute a “black box”, as opposed to the more easily interpretable steps used here to isolate myocytes and quantify their morphological metrics [200]. When the algorithms described here fail, it is generally simple to determine what went wrong and what needs to be changed, whether by adjusting the expected size of nuclei, or by raising the troponin T threshold for classifying cells as myocytes. Interestingly, in the first round of analysis, a random forest algorithm applied to this screen failed to capture any conditions of interest (personal communication). Such strategies could ultimately prove fruitful, but they require more than blind execution.

Nonetheless, our algorithm possesses many disadvantages that a machine learning approach could help overcome. For example, while Otsu segmentation does a reasonably good job of defining cell boundaries, the watershed algorithm struggles to accurately determine borders between abutting cells (Fig. 4.2). This is not problematic when examining cell area, as the results of certain cells claiming too much or too little area tend to average out. However, when measuring elongation, this tendency can be deleterious, since this metric has a much smaller range of variation. When one elongated cell appropriates

cytoplasm from a cell alongside its long border during segmentation, it will raise the calculated minor axis, diminishing the apparent elongation.

Another weakness in the current algorithm is its inability to discriminate between myocyte nuclei and fibroblast nuclei that lie directly behind myocytes, given that it is classifying solely based on the lower quartile intensity of the troponin T stain behind each nucleus. In general, the cytoskeleton appears slightly more intense in the circular region surrounding true nuclei, while in the region behind the nucleus itself, the cytoskeleton should appear fainter. In contrast, a fibroblast nucleus causes no visible changes in the cytoskeletal staining pattern of a myocyte above or underneath it. A more sophisticated algorithm could use this information to eliminate fibroblast nuclei falsely identified as myocytes.

4.5.4. Principles for optimal design of phenotypic screens

The strengths and limitations of our workflow suggest several design principles for maximizing the effectiveness of future large-scale screens. Spatial arrangement of conditions within and across plates is key to reducing and correcting for artifacts. For example, the wells along the edges of plates are particularly susceptible to abnormal cell growth. Although techniques for reducing edge effects have been proposed [201], it is safest to avoid using the edges altogether for test conditions, simply filling them with water or medium instead.

Another important feature of special arrangement is to disperse control wells across the plate, rather than grouping them all in one region, especially a region near the edge. Likewise, there are several benefits of dispersing the several shRNAs targeting a given gene across multiple plates, rather than grouping them on a single plate (or worse yet, in the same region of a single plate). For one thing, if a plate or a portion of a plate has cells with a particularly high area (for instance), a gene with all its shRNAs there will be given an unfair amplification compared with the overall screen. For another thing, if a plate or a portion of a plate yields low-quality data due to poor cell health, poor antibody staining, or microscopy artifacts, you lose all data for a gene whose shRNAs are clustered there.

Finally, we note that consistent naming and formatting practices during data collection are critical to ease of processing. Although the methodology for generating file names, for instance, is rarely if ever apparent at the point of publication, deciding in advance on a schema that integrates well with an automated pipeline can save countless hours of frustration while preparing data for analysis.

4.5.5. Limitations and future directions

Although our normalization method performed well overall, it is unable to correct for artifacts causing regional variation within a single plate. Moreover, as noted above, our measurements are somewhat biased by the nonrandom special locations of genes within and across plates. Given that shRNAs for a given gene were generally spaced in every other well along a single row of a single plate, the myocyte morphologies induced by each shRNA were not truly independent. Our normalization method could also be enhanced by standardizing variance of wells within each plate, in addition to ensuring equal median values of wells within a plate. One simple method of achieving this would be to scale values linearly on either side of the median such that the first and third quartiles of the wells within a plate, in addition to the median, were equal.

In this work, we examined shRNAs from the top percentiles for each morphology, which would presumably identify genes that negatively regulate those phenotypes. We considered the possibility of identify positive regulators for each morphology by looking at the corresponding bottom percentiles. In the case of area, however, this strategy is infeasible because conditions with the smallest cells are dominated simply by apoptosis or general poor cell health, which is difficult to differentiate from cells that are small specifically because of knockdown of a pro-hypertrophic gene. This strategy could be worth pursuing in the case of elongation and spikiness, as long as a minimum threshold for area was established.

More testing is needed to validate the roles of the genes identified in this work. Although we have reduced the false positive rate by restricting our focus to genes with multiple shRNAs scoring above threshold, a significant fraction of the remaining genes is likely still the result of non-specific targeting.

We plan a first round of validation in the near future that repurposes images from a genome-wide screen originally designed to measure aggregate accumulations in cardiomyocytes [165]. Using the same workflow presented here on that dataset and comparing results will enable higher confidence in our predictions. Further work will need to extend testing to other cell types and to *in vivo* experiments.

A final limitation of this screen is the high false negative rate. Given our estimate of 40% efficiency in expression of each of the 5 shRNAs of a given gene, we calculate that $(1 - 0.4)^5 = 7.8\%$ of the 15,000 genes in the screen were not knocked down a single time. An even larger percentage of genes was only knocked down once, eliminating their chances of producing two clones above threshold by specific targeting. Moreover, some gene knockdowns may be more effective in a neonatal or adult (rather than embryonic) context. Thus, the absence of a gene from the final lists of hits should not imply a lack of involvement in mediating myocyte size and shape.

4.5.6. Conclusions

In this chapter, we define a workflow for processing image-based phenotypic screens, extending from image interpretation through filtering and normalization to interpretation. The majority of these steps are highly generalizable to other screens outside the context of cardiac studies or immunofluorescence assays. We especially emphasize the importance of statistical evaluation to determine the minimum number of shRNAs per gene necessary for a desired false positive level. Among the hundreds of genes identified regulating area, elongation, and spikiness, several have already been implicated in cytoskeletal remodeling and cardiac disease, while many others pose ideal candidates for future study *in vivo*. In addition, we delineate principles for designing future screens with the goal of minimal data loss and maximal interpretability. As data generation continues its exponential acceleration over the coming years, expanding and refining techniques for automated analysis will grow increasingly vital.

Chapter 5

Summary and outlook

5.1. Novel contributions

The overall goal of this project was to develop and apply systems-level techniques for the purpose of reconstructing cardiomyocyte growth and remodeling networks. In this work, we harnessed computational modeling and automated image analysis to further existing knowledge of the molecular networks driving heart function and failure. Specifically, we have:

- Developed and validated a comprehensive literature-based predictive model of the cardiac mechano-signaling network.
- Used the model to identify key regulators of mechanical cues, to illuminate the mechanism of action of a combination therapy, and to predict further pairs of drug targets with maximum effects on mechano-signaling.
- Identified clusters correlating with differential forms of hypertrophy from RPPA and phenotypic screens.
- Pioneered and implemented a complete pipeline for analysis, filtering, normalization, and interpretation of genome-scale imaging screens.
- Discovered hundreds of novel regulators of cardiomyocyte morphology.

While previous studies have used RPPA data, high-content imaging, and protein–protein interaction networks, this is the first to combine them with computational modeling to study cardiac remodeling. In addition, this is the first study to identify novel drivers of cardiac growth in a genome-wide imaging screen. Our data-driven modeling framework has revealed novel signaling mechanisms and generated testable predictions for how myocytes control growth and remodeling in the heart.

5.2. Future directions

Although this work has identified several proteins, genes, and control structures central to cardiac remodeling, much work remains in order to develop a comprehensive understanding of the hypertrophy

signaling network. Ideally, we want to obtain a complete vision of how cardiomyocytes grow, one that encompasses neurohormonal and biochemical stimuli, protein activation, gene expression, cellular morphologies, and clinical outcomes. The methods and insights generated in this work suggest several potential routes toward this goal.

One promising direction involves applying methods inspired by work from chapter 2 to the genes and network structures identified in chapters 3 and 4. Recently, we developed a logic-based gene regulatory network that extended the mechano-signaling model in chapter 2 to incorporate whole genomic gene expression changes in response to acute myocyte stretch [202]. Network analysis predicted that the transcription factor SRF is critical to regulating gene changes in response to stretch in the longitudinal (as opposed to transverse) direction. Upstream Regulator Analysis using Ingenuity Pathway Analysis identified additional transcription factors, including PPAR-alpha, Klf15, and E2F1, with a potential role in governing stretch-induced gene changes. In short, this work demonstrated the ability to use transcription factor binding information to connect models of protein regulatory networks to downstream gene sets.

We propose a similar approach to integrating the signaling cascades modulating myocyte elongation, identified in chapter 3, with the individual genes identified in chapter 4 that also influence elongation and likely operate further downstream. Currently, the mechanistic links connecting these processes are lacking. Such an approach would begin by expanding the nascent myocyte elongation network (Fig. 1.1) into a full-fledged logic-based ODE model, including the pathways identified in chapter 3. The model would begin with ligand and receptors and proceed through individual signaling cascades down to transcription factors.

Next, for each transcription factor, a list of target genes and the direction of expression by that transcription factor would be compiled based on the genes identified in chapter 4. Reactions would be substantiated both by co-expression evidence and by DNA binding evidence. After assembling this list, reactions would be added to the model, enabling prediction of gene transcription. Fitting the model to the

observed data would enable matching of individual pathways and transcription factors with distinct genes. Furthermore, sensitivity analyses would help illuminate the control structures governing the elongation network. At the detailed level of modeling the effector machinery producing elongation of actual sarcomeres, such as PKC ϵ and PIP regulation of actin capping by CapZ, smaller-scale approaches might be more beneficial. Ultimately, the reconstructed networks would be integrated back into the master cardiac hypertrophy signaling model.

5.3. Conclusions and ongoing challenges

The prognosis for patients with heart failure is grave, and the diverse pathobiology of individual heart failure patients requires an equally diverse array of personalized therapeutic strategies. In order to incorporate the burgeoning wealth of individual genetic and environmental data into treatment decisions, a systems pharmacology approach toward drug evaluation is crucial. To strengthen the clinical relevance of the models developed in this work, drug–protein interaction data should be incorporated with the novel molecular targets identified. Computational network analysis on global drug–protein datasets would enable rapid prediction of the context-dependent actions and side effects of novel drugs and drug combinations.

Another outstanding challenge to the field is predicting and explaining the varying forms of remodeling of the ventricular chambers. Here, we identified multiple proteins and genes governing remodeling of individual myocytes. Do these regulatory patterns extend to the whole-organ level? More work is needed to assess the clinical importance of these potential therapeutic targets. One initial step would be to mine previously published proteomic and genetic data from heart failure patients to assess correlations between the targets identified in this work and differential clinical outcomes. As noted earlier, many of the molecular regulators uncovered in the RPPA and shRNA screens already have known *in vivo* significance.

The signaling pathways governing heart failure display complex and often seemingly contradictory behavior. In this work, we demonstrate that combining computational tools and a systems perspective can contribute to untangling these complex networks. Often, the most revealing contribution from a model is not in direct identification of a novel mechanism, but rather in pinpointing what is unknown and which experiments need to be performed most urgently, or in highlighting conflicts between existing studies. Continued innovation in modeling methods is necessary to integrating diverse datasets and making their interpretation more tractable.

Appendix A

Experimental parameters

This database summarizes parameters for the cell stretching experiments from the literature used for model construction or validation.

Papers used for model construction:

PMID	author	species	stretch method	stretch mode	stretch direction	stretch intensity	stretch frequency	stretch duration
18332106	Backs Mol Cell Bio 2008	COS						
22427904	Barnabei Plos One 2012	Mouse adult heart	Balloon ex vivo	Static	Equibiaxial	200 mmHg		
9072970	Beals Science 1997	Purified						
10662546	Bespalova Genomics 2000	Purified						
20026769	Bian Hyperten 2010	NRVM						
24850911	Bogomolovas Open Biol 2014	Mouse cell line						
8108121	Brown Oncogene 1994	Purified						
7478553	Buday Oncogene 1995	Purified						
9466976	Calderone JCI 1998	NRVM						
11243782	Centner J Mol Bio 2001	Human Cardiac						
10884684	Chin Trends Cell Bio 2000							
17339567	Cingolani Circ 2007							
9776724	Cingolani Circ Res 1998	Feline papillary muscle	Force transducer	Static	Uniaxial	9%		10 min
21301862	Cingolani Pflugers Arch 2011	NRVM, Mammal papillary muscles						
22056317	Clemente JMCC 2012	Mouse adult heart						
11948406	Coles Oncogene 2002	HEK293						
11448959	Craig JBC 2001	NRVM						
12663674	Davis JBC 2003	NRVM						
7839144	Dérjard Science 1995	Purified						
10376603	Dimmeler Nature 1999	HUVEC						
11788403	Domingos Am J Phys HCP 2002	Rat adult heart	Balloon in vivo	Static	Equibiaxial	15 mmHg		10 min
9612209	Eble Am J Phys 1998	NRVM						
15155564	El Jamali FASEB 2004	NRVM						
1913804	Ervasti Cell 1991	Purified rabbit skeletal muscle						

PMID	author	species	stretch method	stretch mode	stretch direction	stretch intensity	stretch frequency	stretch duration
8349731	Ervasti JBC 1993	Purified rabbit skeletal muscle						
12177418	Fielder PNAS 2002	NRVM						
11062067	Fleming Biochem J 2000	Purified						
11009560	Franchini Circ Res 2000	Rat adult heart	Transverse aortic constriction	Static	Equibiaxial	10–60 mmHg		3–60 min
17720185	Freire JMCC 2007	Rat adult heart						
22921230	Gao JMCC 2012	NRVM						
26483453	Garbincius PNAS 2015	AMVM	Flexcell	Cyclic	Equibiaxial	15%	1 Hz	0–60 min
15205937	Gehmlich Cell Tissue Res 2004	Human cell line						
9079650	Gerwins JBC 1997	Human cell line						
20610383	Gingras JBC 2010	3T3						
25246556	Granzier PNAS 2014	Mouse adult heart, Mouse adult cardiomyocyte	Force transducer	Cyclic	Uniaxial	5%	0.1-100 Hz	
21572419	Guilluy Nat Cell Bio 2011	Mouse embryonic fibroblast						
8654373	Gupta EMBO J 1996	Human cell line						
15001529	Hardt Circ Res 2004	NRVM						
9641916	Hart Science 1998	COS						
12829427	Heidkamp Am J Phys HCP 2003	NRVM						
20585009	Hilfiker-Kleiner Circ 2010	Mouse adult heart						
10219240	Hirota Cell 1999	Mouse adult heart	Transverse aortic constriction	Static	Equibiaxial			3 hr–7 d
9930701	Hofmann Nature 1999	CHO						
22851699	Hojayev Mol Cell Bio 2012	Mouse adult heart						
11172039	Ikuta PNAS 2001	Human cell line						
11777939	Innocenti J Cell Bio 2002	Purified						
8326007	Ito J Clin Inv 1993	NRVM						
15795322	Jeong Circ 2005	NRVM						
18258855	Jeong Circ Res 2008	NRVM	Transverse aortic constriction	Static	Equibiaxial			2 w
26303226	Jiang Cell Physiol Biochem 2015	COS	Custom device with silicone membrane	Static	Uniaxial	20%		10 min
7592992	Jung JBC 1995	Purified rabbit skeletal muscle						
24874017	Katanosaka Nat Commun 2014	NMVM	STREX	Static	Uniaxial	20%		3 s
10849446	Kato JBC 2000	HeLa, CHO						
18830417	Kerkela J Clin Inv 2008	Mouse adult heart						
23000580	Kim J Vet Sci 2012	Adult rat heart	Balloon ex vivo, Aorto-caval shunt	Static	Equibiaxial	40 mmHg		5 min
10864901	Kimura Brit J Pharm 2000	Canine basilar arterial myocyte	Hypotonic cell swelling	Static				
9593662	Klee JBC 1998							
12507422	Knöll Cell 2002	NMVM	Custom device with silicone membrane	Static	Equibiaxial	10%		24 hr
2567995	Knowles PNAS 1989	Rat forebrain						
18466959	Kocksämper PBMB 2008	Human ventricular muscle						
19961855	Koitaishi JMCC 2010	NRVM						
10531040	Kolodziejczyk Curr Bio 1999	Mouse adult heart						

PMID	author	species	stretch method	stretch mode	stretch direction	stretch intensity	stretch frequency	stretch duration
11701614	Kulke Circ Res 2001	Purified, Rabbit cardiac muscle	Force transducer	Static	Uniaxial			10–20 s
8921810	Kunisada Circ 1996	NRVM						
9020175	Kuppuswamy JBC 1997	Cat adult heart	Pulmonary artery constriction, Balloon in vivo					4 hr–5 w
15798203	Kuwahara Mol Cell Bio 2005	Mouse cell line						
14983059	Kwan PNAS 2004	Human coronary endothelial cell line						
12432079	Lange J Cell Sci 2002	Rat papillary muscle						
25336613	Lauriol Sci Sig 2014	Mouse adult heart						
20566642	Leenders JBC 2010	NRVM						
18317936	Lemaire-Ewing Cell Biol Toxicol 2009	Human cell line						
9507010	Leopoldt JBC 1998	Purified						
9525975	Leri J Clin Inv 1998	ARVM	Custom device with silicone membrane	Static	Equibiaxial	9%		10 min–24 hr
8978330	Leskinin Circ Res 1997	Rat adult heart	Right atrial saline injection	Static	Equibiaxial			5–21 min
11585926	Liang Mol Cell Bio 2001	NRVM						
22403241	Liu Circ Res 2012	Mouse adult heart						
20605796	Loukin JBC 2010	Xenopus oocyte	Hypotonic cell swelling	Static				
1577864	Lu J Cell Bio 1992	Chick embryonic cardiomyocyte						
10737771	Lu PNAS 2000	NRVM						
12176756	Lyford Am J Phys CP 2002	CHO	Bath perfusion, Pipette pressure	Static				
23266827	Manso JBC 2013	Mouse adult heart	Transverse aortic constriction	Static	Equibiaxial			10 min–1 w
15522277	Markou JBCC 2004	ARVM						
7746328	Marrero Nature 1995	Rat aortic myocyte						
9576927	Mascareno PNAS 1998	Rat adult heart						
20876535	Masuda JBC 2010	COS						
8635223	Matsuda Circ Res 1996	Rabbit cardiomyocyte	Hypotonic cell swelling	Static				
9299374	McWhinney JMCC 1997	NRVM	Custom device with silicone membrane	Static	Uniaxial	20%		90 min
9891086	Mercurio Mol Cell Bio 1999	Human cell line						
2174351	Mignery EMBO J 1990	COS						
8831108	Miyata Eur J Pharm 1996	NRVM	Custom device with silicone membrane	Static	Uniaxial	15%		10 min–4 d
9568714	Molkentin Cell 1998	Mouse adult heart						
18718528	Moon Cell Signal 2008	Mouse cell line						
12881422	Morton EMBO J 2003	Mouse cell line						
18776042	Nakamura Circ Res 2008	Mouse adult heart						
15950986	Nelson JMCC 2005	NRVM, Mouse adult heart						
11387209	Nicol EMBO J 2001	NRVM						
15743761	Nishida JBC 2005	NRVM						
16880823	Nishimoto EMBO Rep 2006	Human cell line						
12604610	Nojima JBC 2003	Human cell line						
9814702	Oancea Cell 1998	Rat cell line						
23271052	Okamoto FASEB 2013	Mouse adult heart						

PMID	author	species	stretch method	stretch mode	stretch direction	stretch intensity	stretch frequency	stretch duration
11799083	Omura Hyperten 2002	NRVM						
10485710	Ozes Nature 1999	HEK293						
26847743	Paudyal J Phys 2016	NRVM	Flexcell	Cyclic	Equibiaxial	10%	1Hz	48 hr
15910769	Peng Brain Res 2005	HEK293	Bath perfusion	Static				
18448675	Peng PNAS 2008	Mouse adult heart						
20041152	Pereira Plos One 2009	Mouse adult heart, NRVM	Transverse aortic constriction	Static	Equibiaxial			1–15 d
11087248	Pham Am J Phys HCP 2000	NRVM						
15610731	Philippar Mol Cell 2004	Human cell line						
10652349	Porter JBC 2000	COS						
26259779	Qi JMCC 2015	Human ESC-CM	STREX	Cyclic	Uniaxial	10-30%	1Hz	0–20 min
20530803	Rakesh Sci Sig 2010	HEK293	Flexcell, Hypotonic cell swelling, In vivo balloon	Both	Both	10%	1Hz	0–30 min
15483225	Rauch Am J Phys CP 2005	C2C12	Flexcell	Static	Equibiaxial	9%		5 min–3 hr
11923478	Ray Mol End 2002	HepG2						
11015615	Rebecchi Physiol Rev 2000	Purified						
11715022	Rommel Nat Cell Bio 2001	C2C12						
23357406	Rosa Cell Calc 2013	HEK293	Pressure-flow pulses					
7744823	Russell JBC 1995	Human cell line						
8909541	Rybakova J Cell Bio 1996	Purified rabbit skeletal muscle						
10974007	Rybakova J Cell Bio 2000	Mouse skeletal muscle	Mechanical peeling					
8348686	Sadoshima 1993 Circ Res	NRVM						
8001266	Sadoshima Circ Res 1995	NRVM						
19719782	Salameh Br J Pharm 2009	NRVM						
17376402	Salazar BBA 2007							
15657416	Sanna Mol Cell Bio 2005	NRVM						
12167717	Scheid Mol Cell Bio 2002	Human cell line						
9566877	Schlaepfer Mol Cell Bio 1998							
10724174	Schlossmann Nature 2000	Bovine tracheal smooth muscle						
9478959	Schmidt JBC 1998	Osteosarcoma cell line	Microbeads	Both	Uniaxial	10 dyne/cm ²	1 Hz	30 min
12767723	Shah Trends Pharm Sci 2003							
19033658	Sheikh J Clin Inv 2008	Mouse adult heart	Force transducer, Transverse aortic constriction	Static	Equibiaxial	20 kPa		5 hr–5 d
21284984	Shimizu Cell Metab 2011	Rat cell line						
2173712	Shubeita JBC 1990	NRVM						
15781459	Skurk JBC 2005	NRVM						
17056714	Spassova PNAS 2006	CHO and HEK293	Hypotonic cell swelling	Static				
1447296	Straub J Cell Bio 1992	Human skeletal muscle						
11073940	Sun JBC 2001	Human cell line						
19652361	Sundaresan J Clin Inv 2009	Mouse adult heart						
22972902	Takefuji Circ 2012	Mouse adult heart						
9305639	Takekawa EMBO J 1997	Human cell line						
21108934	Tang Biochem Pharm 2011	NRVM						
25170081	Tang JBC 2014	HEK293	Hypotonic cell swelling	Static				

PMID	author	species	stretch method	stretch mode	stretch direction	stretch intensity	stretch frequency	stretch duration
24637628	Teng JOVE 2013	Yeast, Xenopus oocyte	Hypotonic cell swelling	Static				
16873723	Tenhunen Circ Res 2006	Rat adult heart						
12570982	Torsoni Am J Phys CP 2003	Rat adult heart	Transverse aortic constriction	Static	Equibiaxial	40 mmHg		5–60 min
9207092	Tournier PNAS 1997	Hamster cell line						
11262406	Uozumi JBC 2001	Mouse adult heart	Transverse aortic constriction	Static	Equibiaxial			4 w
21746915	van Berlo PNAS 2011	Mouse adult heart						
15367659	Vega Mol Cell Bio 2004	NRVM						
12650883	von Lewinski Cardiovasc Res 2003	Rabbit ventricular muscle	Force transducer	Static	Uniaxial	10%		
15105296	von Lewinski Circ Res 2004	Human ventricular muscle	Force transducer	Static	Uniaxial	10%		0–15 min
18612045	Waddell Am J Phys EM 2008	Human cell line						
16376520	Wang Cell Sig 2006							
7684161	Wang Science 1993	Capillary endothelial cells	Microbeads	Static	Uniaxial	0–68 dyne/cm ²		
8332195	Warne Nature 1993	Bacteria cell line						
8557975	Whitehurst J Immunol 1996	Cell line						
12370307	Wilkins Mol Cell Bio 2002	Mouse adult heart						
17272810	Willis Circ Res 2007	Monkey cell line	Transverse aortic constriction	Static	Equibiaxial			1–2 w
11799084	Wollert Hyperten 2002	NRVM						
20382852	Wu Am J Phys HCP 2010	Mouse adult cardiomyocyte						
21750914	Xu Mol Bio Res 2012	Mouse adult heart						
16172266	Xuan Circ 2005	Mouse adult heart						
16037569	Yamada Circ Res 2005	NRVM	Custom device with silicone membrane	Cyclic	Uniaxial	10%	3–Hz	1 hr
8621724	Yamazaki JBC 1996	NRVM	Custom device with silicone membrane	Static	Uniaxial	20%		1 min–24 hr
8974057	Yamazaki Mol Cell Biochem 1996	NRVM	Custom device with silicone membrane	Static	Uniaxial	20%		1–60 min
7997270	Yan Nature 1994	Monkey cell line						
11739382	Yanazume JBC 2002	NRVM						
10330143	Yang Mol Cell Bio 1999	COS						
17267546	Zhang Am J Phys CP 2007	C2C12	Flexcell	Cyclic	Equibiaxial	10%	0.5 Hz	2–4 d
12202037	Zhang Cell 2002	Mouse adult heart						
8610126	Zhu PNAS 1996	Monkey cell line						
15146194	Zou Nat Cell Bio 2004	NRVM	Custom device with silicone membrane	Static	Uniaxial	20%		8 min

Papers used for model validation:

PMID	author	species	stretch method	stretch mode	stretch direction	stretch intensity	stretch frequency	stretch duration
10066681	Aikawa Circ Res 1999	NRVM	Custom device with silicone membrane	Static	Uniaxial	20%		9 min
11847190	Aikawa Hyperten 2002	NRVM	Custom device with silicone membrane	Static	Uniaxial	10–30%		5 min–24 hr
14645255	Anderson JBC 2004	NRVM	Flexcell	Cyclic	Equibiaxial	20%	1 Hz	5 min–48 hr
12909322	Baba Cardiovasc Res 2003	NRVM	Flexcell	Cyclic	Equibiaxial	10%	1 Hz	5–60 min
16963613	Boateng Am J Phys HCP 2007	NRVM	Flexcell	Cyclic	Equibiaxial	10%	1 Hz	48 hr
19376126	Boateng JMCC 2009	NRVM	Flexcell	Cyclic	Both	10%	1 Hz	48 hr
9925362	Cadre JMCC 1998	NRVM	Flexcell	Cyclic	Equibiaxial	20%	1 Hz	48–72 hr
19673940	Cheng Clin Exp Pharm Phys 2009	NRVM	Flexcell	Cyclic	Equibiaxial	20%	1 Hz	30 min–24 hr
18854312	Del Re JBC 2008	NRVM	Custom device with silicone membrane	Static	Equibiaxial	10%		5 min–2 hr
19015044	Duquesnes Int J Biochem Cell Biol 2009	NRVM	Flexcell	Static	Equibiaxial	15%		1–60 min
26512830	Feng Int J Cardiol 2016	NRVM	Flexcell	Static	Equibiaxial	20%		15 min–2 hr
18158353	Frank Hyperten 2008	NRVM	Custom device with silicone membrane	Static	Equibiaxial	12%		24 hr
20600098	Frank JMCC 2010	NRVM	Custom device with silicone membrane	Static	Equibiaxial	12%		24 hr
15665106	Heineke PNAS 2005	NRVM	Flexcell	Cyclic	Equibiaxial	15%	0.5Hz	24 hr
12777392	Kawamura JBC 2003	NRVM	Custom device with silicone membrane	Static	Equibiaxial	20%		1–15 min
8621062	Komuro FASEB 1996	NRVM	Custom device with silicone membrane	Static	Uniaxial	10–30%		1 min–2 hr
2105950	Komuro JBC 1990	NRVM	Custom device with silicone membrane	Static	Uniaxial	5–20%		30 min
20606005	Kuwahara Mol Cell Bio 2010	NRVM	Custom device with silicone membrane			20%		5 min–4 hr
17583725	Lal JMCC 2007	NRVM	Flexcell	Static	Equibiaxial	20%		2–15 min
18926830	Lal JMCC 2008	NRVM	Flexcell	Static	Equibiaxial	20%		2min–24 hr
15802564	Lange Science 2005	NRVM	Arrest of beating					
22174951	Leychenko Plos One 2011	ARVM	Flexcell	Cyclic	Equibiaxial	10%	0.5Hz	24–48 hr
9603978	Liang JBC 1999	NRVM	Flexcell	Cyclic	Equibiaxial	20%	1Hz	2–48 hr
14521925	Liao BBRC 2003	NRVM	Flexcell	Static	Equibiaxial	20%		90 min
18757826	Marin Circ Res 2008	NRVM	Flexcell	Cyclic	Equibiaxial	15%	1Hz	10–60 min
15961069	Nadruz Cardiovasc Res 2005	NRVM	Flexcell	Cyclic	Equibiaxial	15%	1Hz	10 min–2 hr
9588217	Nyui BBRC 1998	NRVM	Ikemoto	Static	Uniaxial	20%		10 min
10347087	Pan Circ Res 1999	NRVM	Custom device with silicone membrane	Static	Uniaxial	20%		2–30 min
12704188	Pikkarainen JBC 2003	NRVM	Flexcell	Cyclic	Equibiaxial	10–25%	0.5Hz	15 min–24 hr
17965285	Rana Am J Phys HCP 2007	NRAM	Custom device with Flexcell plates	Static	Equibiaxial	3–21%		48 hr
11162845	Ruwhof Cell Calc 2001	NRVM	Flexcell, Custom device with silicone membrane, Prodding with microelectrode	Cyclic	Equibiaxial	15–25%	1Hz	15 s–2 hr
25696767	Ruwhof Neth Heart 2001	NRVM	Flexcell	Cyclic	Equibiaxial	20%	1Hz	5–30 min
8252633	Sadoshima Cell 1993	NRVM	Custom device with silicone membrane	Static	Uniaxial	20%		10 min–24 hr
8385610	Sadoshima EMBO 1993	NRVM	Custom device with silicone membrane	Static	Uniaxial	20%		1 min–2 hr
1534087	Sadoshima JBC 1992	NRVM	Custom device with silicone membrane	Static	Uniaxial	20%		30 min–48 hr
20378856	Salameh Circ Res 2010	NRVM	Flexcell	Cyclic	Uniaxial	5–20%	1Hz	24–48 hr
20705136	Salameh Pharm Res 2010	NRVM	Flexcell	Cyclic	Uniaxial	10%	1Hz	24 hr
10334907	Seko BBRC 1999 b	NRVM	Flexcell	Cyclic	Equibiaxial	15%	1Hz	2–30 min
11273722	Shyu JMCC 2001	NRVM	Flexcell	Cyclic	Equibiaxial	20%	1Hz	2–48 hr

PMID	author	species	stretch method	stretch mode	stretch direction	stretch intensity	stretch frequency	stretch duration
15532707	Sil Mol Cell Biochem 1999	NRVM	Flexcell	Cyclic	Equibiaxial	24%	1Hz	30 min–2 hr
23530122	Takefuji J Exp Med 2013	NRVM	Flexcell	Cyclic	Equibiaxial	10%	1Hz	3 min–24 hr
9688953	Tamura Am J Phys RICP 1998	NRVM	Ikemoto	Static	Uniaxial	20%		1–24 hr
15923313	Torsoni Am J Phys HCP 2005	NRVM	Flexcell	Cyclic	Equibiaxial	15%	1Hz	10 min–4 hr
12805241	Torsoni Circ Res 2003	NRVM	Flexcell	Cyclic	Equibiaxial	5-20%	1Hz	10 min–2 hr
11330825	van Wamel Mol Cell Biochem 2001	NRVM	Flexcell	Static	Equibiaxial	15%		30–60 min
11584267	Vila Petroff Nat Cell Bio 2001	ARVM	Custom device with agarose	Static	Uniaxial	0-20%		0–15 min
24120154	Wang JFMA 2013	NRVM	Flexcell	Cyclic	Equibiaxial	20%	1Hz	4–24 hr
15350851	Wang JMCC 2004	NRVM	Flexcell	Cyclic	Equibiaxial	20%	1Hz	6–24 hr
10419503	Yamamoto Circ 2001	NRVM	Custom device with silicone membrane	Cyclic	Equibiaxial	4%	1.2Hz	1–60 min
10419504	Yamamoto JBC 1999	NRVM	Custom device with silicone membrane	Static	Equibiaxial	1-14%		1–24 hr
17207463	Yamane BBRC 2007	NRVM	STREX	Cyclic	Uniaxial	20%	0.5Hz	5 min–20 hr
9506703	Yamazaki Circ Res 1998	NRVM	Custom device with silicone membrane	Static	Uniaxial	20%		2 min–24 hr
7615816	Yamazaki J Clin Inv 1995	NRVM	Custom device with silicone membrane	Static	Uniaxial	20%		1–60 min
17264507	Zobel Cardiol 2007	NRVM	Flexcell	Static	Equibiaxial			48hr

Appendix B

Mechano-signaling network model

This database includes information about each species in the cardiac mechano-signaling network.

module	ID	name	Y_{init}	Y_{max}	τ	type	alternate names
integrin	aActinin	alpha-actinin	0	1	1	protein	
integrin	Actin	Actin	0	1	1	protein	
PI3K	Akt	Protein kinase B	0	1	1	protein	PKB
outputs	aMHC	Alpha-myosin heavy chain	1	1	1	geneExpr	
g-coupled	AngII	Angiotensin II	0	1	1	protein	
outputs	ANP	Atrial natriuretic protein	0	1	1	geneExpr	ANF
outputs	Ao	Angiotensinogen	0	1	1	geneExpr	
transcription	AP1	Activator protein 1	0	1	1	protein	
g-coupled	AT1R	Antiotensin type 1 receptor	0	1	1	protein	
outputs	bMHC	Beta-myosin heavy chain	0	1	1	geneExpr	
outputs	BNP	Brain natriuretic protein	0	1	1	geneExpr	
calcium	Ca	Calcium	0	1	1	smallMolecule	Ca ²⁺
calcium	CaM	Calmodulin	0	1	1	protein	
calcium	CaMK	CaM kinase	0	1	1	protein	
calcium	CaN	Calcineurin	0	1	1	protein	
outputs	CellArea	Cell area	0	1	1	phenotype	
transcription	cFos	Proto-oncogene c-Fos	0	1	1	protein	
PI3K	cGMP	Cyclic guanosine monophosphate	0	1	1	smallMolecule	
transcription	cJun	Proto-oncogene c-Jun	0	1	1	protein	
transcription	cMyc	Proto-oncogene c-Myc	0	1	1	protein	
transcription	CREB	cAMP response element binding	0	1	1	protein	
outputs	Cx43	Connexin 43	0	1	1	geneExpr	
g-coupled	DAG	Diacylglycerol	0	1	1	phospholipid	

module	ID	name	Y_{init}	Y_{max}	τ	type	alternate names
integrin	Dysgl	Dystroglycans	0	1	1	protein	
integrin	Dysph	Dystrophin	0	1	1	protein	
growth factor	EGFR	Epidermal growth factor receptor	0	1	1	protein	
PI3K	eIF4E	Eukaryotic translation initiation factor 4E	0	1	1	protein	
PI3K	eIF2B	Eukaryotic translation initiation factor 2B	0	1	1	protein	
MAPK	ERK12	Extracellular signal-related kinases 1 or 2	0	1	1	protein	p42/p44 MAPK
MAPK	ERK5	Extracellular signal-related kinase 5	0	1	1	protein	BMK1
g-coupled	ET1	Endothelin-1	0	1	1	protein	
g-coupled	ET1R	Endothelin-1 receptor	0	1	1	protein	
integrin	FAK	Focal adhesion kinase	0	1	1	protein	
integrin	FHL1	Four-and-a-half LIM domains protein 1	0	1	1	protein	
integrin	FHL2	Four-and-a-half LIM domains protein 2	1	1	1	protein	
transcription	FoxO	Forkhead box O	1	1	1	protein	
g-coupled	Ga1213	G 12/13 alpha subunit	0	1	1	protein	
g-coupled	Gaq11	G q/11 alpha subunit	0	1	1	protein	
transcription	GATA4	GATA-binding protein 4	0	1	1	protein	
g-coupled	Gbg	G beta/gamma subunit	0	1	1	protein	
cytokine	gp130	Glycoprotein 130	0	1	1	protein	
PI3K	GSK3b	Glycogen synthase kinase 3 beta	1	1	1	protein	
transcription	HDAC	Histone deacetylase	1	1	1	protein	
PI3K	IkB	Nuclear factor of kappa light polypeptide gene enhancer in B-cells inhibitor, alpha	1	1	1	protein	
PI3K	IKK	Inhibitor of kappa light polypeptide gene enhancer in B-cells, kinase beta	0	1	1	protein	
integrin	Integrin	Integrin	0	1	1	protein	
g-coupled	IP3	Inositol triphosphate	0	1	1	phospholipid	
cytokine	JAK	Janus kinase 1 or 2	0	1	1	protein	
MAPK	JNK	c-Jun N-terminal kinase	0	1	1	protein	SAPK
MAPK	Lmcd1	LIM and cystein-rich domains 1	0	1	1	protein	Dyxin
calcium	LTCC	L-type calcium channel	0	1	1	protein	
transcription	MEF2	Myocyte enhancer factor 2	0	1	1	protein	
MAPK	MEK12	MAPK/ERK kinase 1 or 2	0	1	1	protein	MAPKK12
MAPK	MEK36	MAPK/ERK kinase 3 or 6	0	1	1	protein	MAPKK36
MAPK	MEK47	MAPK/ERK kinase 4 or 7	0	1	1	protein	MAPKK4 or MAPKK7, TAK1, SEK1
MAPK	MEK5	MAPK/ERK kinase 5	0	1	1	protein	

module	ID	name	Y_{init}	Y_{max}	τ	type	alternate names
MAPK	MEKK1	MAPK/ERK kinase kinase 1	0	1	1	protein	MAP3K1
MAPK	MEKK23	MAPK kinase kinase 2 or 3	0	1	1	protein	MAP3K23
MAPK	MEKK4	MAPK kinase kinase 4	0	1	1	protein	MAP3K4, MTK1
integrin	MLP	Muscle LIM protein	0	1	1	protein	
outputs	MRTF	Myocardin-related transcription factor	0	1	1	protein	
PI3K	mTor	Mechanistic target of rapamycin	0	1	1	protein	
integrin	MuRF	Muscle ring finger protein	1	1	1	protein	
calcium	Na	Sodium	0	1	1	smallMolecule	Na ⁺
calcium	NCX	Sodium-calcium exchanger	0	1	1	protein	
transcription	NFAT	Nuclear factor of activated T-cells	0	1	1	protein	
transcription	NFkB	Nuclear factor kappa-light-chain-enhancer of activated B cells	0	1	1	protein	
calcium	NHE	Sodium-hydrogen exchanger	0	1	1	protein	
PI3K	NOS	Endothelial nitric oxide synthase	0	1	1	protein	
MAPK	p38	p38 mitogen-activated protein kinase	0	1	1	protein	
PI3K	p70s6k	70 kDa ribosomal protein S6 kinase 1	0	1	1	protein	
PI3K	PDK1	3-phosphoinositide dependent protein kinase 1	0	1	1	protein	
PI3K	PI3K	Phosphatidylinositol 3 kinase	0	1	1	protein	
g-coupled	PKC	Protein kinase C	0	1	1	protein	
PI3K	PKG1	cGMP-dependent protein kinase 1	0	1	1	protein	
g-coupled	PLC	Phospholipase C	0	1	1	protein	
outputs	PrSynth	Protein synthesis	0	1	1	phenotype	
MAPK	Rac1	Ras-related C3 botulinum toxin substrate 1	0	1	1	protein	
MAPK	Raf1	Proto-oncogene c-Raf	0	1	1	protein	
MAPK	Ras	Rat sarcoma viral oncogene homolog	0	1	1	protein	p21ras
MAPK	RhoA	Ras homolog gene family, member A	0	1	1	protein	
MAPK	RhoGEF	Rho guanine nucleotide exchange factor 12	0	1	1	protein	
MAPK	ROCK	Rho-associated protein kinase	0	1	1	protein	
outputs	sACT	skeletal alpha-actin	0	1	1	geneExpr	
outputs	SERCA	Sarcoplasmic reticulum Ca ²⁺ ATPase	1	1	1	geneExpr	
PI3K	sGC	Soluble guanylyl cyclase	0	1	1	protein	
integrin	Src	Proto-oncogene c-Src	0	1	1	protein	
MAPK	SRF	Serum response factor	0	1	1	protein	
transcription	STAT	Signal transducers and activators of transcription	0	1	1	protein	
input	Stretch	Stretch	0	1	1	perturbation	
integrin	Talin	Talin	0	1	1	protein	

module	ID	name	Y_{init}	Y_{max}	τ	type	alternate names
integrin	Titin	Titin	0	1	1	protein	
calcium	TRP	Transient receptor potential channel	0	1	1	protein	
integrin	Vinculin	Vinculin	0	1	1	protein	

Appendix C

Mechano-signaling network model reactions

This database includes information about each reaction in the cardiac mechano-signaling network. For references for each reaction, see S1 Table in Tan *PLoS Comput. Biol.* 13(11), 2017.

module	ID	rule	w	n	EC ₅₀	notes
input	i1	=> Stretch	0	1.4	0.5	Stretch input
input	i2	=> AngII	0	1.4	0.5	AngII addition
input	i3	=> AT1R	0	1.4	0.5	AT1R activation (without AngII)
input	i4	=> Dysgl	0	1.4	0.5	Dysgl activation
input	i5	=> ET1	0	1.4	0.5	ET1 addition
input	i6	=> gp130	0	1.4	0.5	gp130 activation
input	i7	=> Integrin	0	1.4	0.5	Integrin activation
input	i8	=> LTCC	0	1.4	0.5	LTCC activation
input	i9	=> NHE	0	1.4	0.5	NHE activation
input	i10	=> TRP	0	1.4	0.5	TRP activation
input	i11	=> sGC	0	1.4	0.5	sGC activation
middle	r1	Stretch => AngII	0.9	1.4	0.5	Stretch induces AngII secretion
middle	r2	Stretch => AT1R	0.9	1.4	0.5	Stretch activates AT1R
middle	r3	Stretch => Dysgl	0.9	1.4	0.5	Stretch exerts force on Dysgl
middle	r4	Stretch => ET1	0.9	1.4	0.5	Stretch induces ET1 secretion
middle	r5	Stretch => gp130	0.9	1.4	0.5	Stretch activates gp130
middle	r6	Stretch => Integrin	0.9	1.4	0.5	Stretch activates Integrin
middle	r7	!PKG1 & Stretch => LTCC	0.9	1.4	0.5	Stretch activates L-type Ca channel PKG1 inhibits LTCC
middle	r8	Stretch => NHE	0.9	1.4	0.5	Stretch activates NHE
middle	r9	!PKG1 & Stretch => TRP	0.9	1.4	0.5	Stretch activates Trp

module	ID	rule	w	n	EC ₅₀	notes
						PKG1 phosphorylates and inhibits TRP
middle	r10	Actin => aActinin	0.9	1.4	0.5	Actin links to aActinin
middle	r11	Actin => Lmcd1	0.9	1.4	0.5	Actin activates Lmcd1
middle	r12	Actin => Titin	0.9	1.4	0.5	Actin links to Titin
middle	r13	!Akt => FoxO	0.9	1.4	0.5	Akt phosphorylates and inactivates FoxO
middle	r14	!Akt => GSK3b	0.9	1.4	0.5	Akt phosphorylates and inactivates GSK3B
middle	r15	Akt => IKK	0.9	1.4	0.5	Akt activates IKK
middle	r16	Akt => mTor	0.9	1.4	0.5	Akt activates mTor
middle	r17	Akt => NOS	0.9	1.4	0.5	Akt activates NOS
middle	r18	AngII => AT1R	0.9	1.4	0.5	AngII binds to AT1R
middle	r19	AP1 & CREB & GATA4 & MEF2 & NFAT & SRF => ANP	0.9	1.4	0.5	AP1 is necessary for ANP transcription CREB is necessary for ANP transcription GATA4 is necessary for ANP transcription MEF2 is necessary for ANP transcription NFAT is necessary for ANP transcription SRF is necessary for ANP transcription
middle	r20	AP1 & CREB & GATA4 & NFAT & SRF => bMHC	0.9	1.4	0.5	AP1 is necessary for bMHC transcription CREB is necessary for bMHC transcription GATA4 is necessary for bMHC transcription NFAT is necessary for bMHC transcription SRF is necessary for bMHC transcription
middle	r21	AP1 & CREB & GATA4 & NFAT & SRF => BNP	0.9	1.4	0.5	AP1 is necessary for BNP transcription CREB is necessary for BNP transcription GATA4 is necessary for BNP transcription NFAT is necessary for BNP transcription SRF is necessary for BNP transcription
middle	r22	AP1 & CREB & GATA4 & MEF2 & NFAT => CellArea	0.9	1.4	0.5	AP1 is necessary for CellArea increase CREB is necessary for CellArea increase GATA4 is necessary for CellArea increase MEF2 is necessary for CellArea increase NFAT is necessary for CellArea increase
middle	r23	AP1 & CREB & GATA4 & NFAT & SRF => sACT	0.9	1.4	0.5	AP1 is necessary for sACT transcription CREB is necessary for sACT transcription GATA4 is necessary for sACT transcription NFAT is necessary for sACT transcription SRF is necessary for sACT transcription
middle	r24	AP1 & CREB => Cx43	0.9	1.4	0.5	AP1 is necessary for Cx43 transcription CREB is necessary for Cx43 transcription
middle	r25	!AP1 => aMHC	0.9	1.4	0.5	AP1 inhibits aMHC transcription
middle	r26	!AP1 => SERCA	0.9	1.4	0.5	AP1 inhibits SERCA transcription
middle	r27	AT1R => ET1	0.9	1.4	0.5	AT1R induces autocrine ET1 release
middle	r28	AT1R => Ga1213	0.9	1.4	0.5	AT1R activates Ga1213

module	ID	rule	w	n	EC ₅₀	notes
middle	r29	AT1R => Gaq11	0.9	1.4	0.5	AT1R is coupled to Gaq11
middle	r30	AT1R => JAK	0.9	1.4	0.5	AT1R activates JAK
middle	r31	Ca & DAG => PKC	0.9	1.4	0.5	Calcium and DAG cooperate to activate PKC
middle	r32	Ca => CaM	0.9	1.4	0.5	Ca binds to CaM
middle	r33	CaM & Lmcd1 & MLP => CaN	0.9	1.4	0.5	CaM binds to CaN; MLP is required for CaN activation Lmcd1 is necessary for NFAT nuclear translocation MLP is necessary for CaN activation
middle	r34	CaM => CaMK	0.9	1.4	0.5	CaM binds CaMK
middle	r35	!CaMK & !PKC => HDAC	0.9	1.4	0.5	CaMK phosphorylates HDAC causing its nuclear export PKC phosphorylates HDAC causing its nuclear export
middle	r36	cFos & cJun => AP1	0.9	1.4	0.5	cFos and cJun form heterodimer AP1 complex
middle	r37	cJun => AP1	0.9	1.4	0.5	cJun forms homodimer AP1 complex
middle	r38	cGMP => PKG1	0.9	1.4	0.5	cGMP binds to and activates PKG1
middle	r39	CREB & STAT => Ao	0.9	1.4	0.5	CREB is necessary for Ao transcription STAT is necessary for Ao transcription
middle	r40	Dysgl => Dysph	0.9	1.4	0.5	Dysgl links to Dysph
middle	r41	Dysph => Actin	0.9	1.4	0.5	Dysph links to Actin
middle	r42	EGFR & JAK => Ras	0.9	1.4	0.5	EGFR is required for Ras activation JAK is required for Ras activation
middle	r43	Src => Ras	0.9	1.4	0.5	Src activates Ras
middle	r44	eIF2B & eIF4E & p70s6k => PrSynth	0.9	1.4	0.5	eIF2B is required for increased protein expression eIF4E is required for increased protein expression p70s6k is required for increased protein expression
middle	r45	ERK12 => cFos	0.9	1.4	0.5	ERK12 phosphorylates cFos
middle	r46	ERK12 => cJun	0.9	1.4	0.5	ERK12 phosphorylates cJun
middle	r47	ERK12 => cMyc	0.9	1.4	0.5	ERK12 phosphorylates cMyc
middle	r48	ERK12 => NFkB	0.9	1.4	0.5	ERK12 phosphorylates NFkB; Ikb binds to and inhibits NFkB
middle	r49	ERK5 => cMyc	0.9	1.4	0.5	ERK5 phosphorylates cMyc
middle	r50	ET1 => ET1R	0.9	1.4	0.5	ET1 binds to ET1R
middle	r51	ET1R => EGFR	0.9	1.4	0.5	ET1R transactivates EGFR through NADPH
middle	r52	ET1R => Gaq11	0.9	1.4	0.5	ET1R activates Gaq11
middle	r53	FAK => PI3K	0.9	1.4	0.5	FAK activates PI3K
middle	r54	FAK => Src	0.9	1.4	0.5	FAK activates Src
middle	r55	FHL1 & MEK12 => ERK12	0.9	1.4	0.5	MEK12 phosphorylates ERK12 FHL1 activates phospho-ERK12
middle	r56	!FHL2 & CaN => NFAT	0.9	1.4	0.5	FHL2 binds CaN preventing NFAT activation CaN dephosphorylates NFAT

module	ID	rule	w	n	EC ₅₀	notes
middle	r57	!FHL2 & CaN & ERK12 => NFAT	0.9	1.4	0.5	ERK12 phosphorylates CaN NFAT complex, increasing NFAT DNA binding in the nucleus
middle	r58	!FHL2 & !HDAC & !MuRF & MRTF => SRF	0.9	1.4	0.5	FHL2 binds promoters of SRF-responsive genes HDAC dissociates from SRF ending its inhibition MuRF reduces nuclear SRF MRTF co-activates with SRF
middle	r59	gp130 => JAK	0.9	1.4	0.5	gp130 phosphorylates JAK
middle	r60	Ga1213 => RhoGEF	0.9	1.4	0.5	Ga1213 activates RhoGEF
middle	r61	Gaq11 => FHL1	0.9	1.4	0.5	Gaq11 activates FHL1
middle	r62	Gaq11 => Gbg	0.9	1.4	0.5	GPCR dissociates into alpha and beta gamma subunits
middle	r63	Gaq11 => PLC	0.9	1.4	0.5	Gaq11 binds PLC
middle	r64	Gbg => PI3K	0.9	1.4	0.5	Gbg activates PI3K
middle	r65	!GSK3b & !JNK & !p38 & NFkB => NFAT	0.9	1.4	0.5	GSK3b phosphorylates NFAT to prevent nuclear translocation JNK phosphorylates NFAT to prevent nuclear translocation p38 phosphorylates NFAT to prevent nuclear translocation NFkB binds NFAT and promotes its activation
middle	r66	!GSK3b & ERK12 => GATA4	0.9	1.4	0.5	GSK3b prevents expression and nuclear localization of GATA4 ERK12 phosphorylates GATA4
middle	r67	!GSK3b & p38 => GATA4	0.9	1.4	0.5	p38 phosphorylates GATA4
middle	r68	!GSK3b & ROCK => GATA4	0.9	1.4	0.5	ROCK contributes to GATA4 activation
middle	r69	!GSK3b & p38 => CREB	0.9	1.4	0.5	GSK3b inhibits CREB by phosphorylation at a secondary site p38 phosphorylates and activates CREB
middle	r70	!GSK3b => eIF2B	0.9	1.4	0.5	GSK3b phosphorylates and inhibits eIF2B
middle	r71	!HDAC & aActinin => MLP	0.9	1.4	0.5	HDAC blocks MLP nuclear accumulation aActinin binds to MLP
middle	r72	!HDAC & ERK5 => MEF2	0.9	1.4	0.5	HDAC dissociates from MEF2 ending its inhibition ERK5 phosphorylates MEF2
middle	r73	!HDAC & p38 => MEF2	0.9	1.4	0.5	p38 phosphorylates MEF2
middle	r74	!IkB => NFkB	0.9	1.4	0.5	IKK phosphorylates IkB targeting it for degradation
middle	r75	!IKK => IkB	0.9	1.4	0.5	IKK phosphorylates IkB targeting it for degradation
middle	r76	Integrin & RhoA => FAK	0.9	1.4	0.5	Integrins activate FAK RhoA is necessary for FAK activation
middle	r77	Integrin => RhoGEF	0.9	1.4	0.5	Integrin activates RhoGEF
middle	r78	Integrin => Talin	0.9	1.4	0.5	Talin and Vcl link Integrin to Actin
middle	r79	IP3 => Ca	0.9	1.4	0.5	IP3 binds to IP3 receptors on the endoplasmic reticulum which release Ca ions
middle	r80	JAK => STAT	0.9	1.4	0.5	JAK phosphorylates STAT

module	ID	rule	w	n	EC ₅₀	notes
middle	r81	JNK => cJun	0.9	1.4	0.5	JNK phosphorylates cJun
middle	r82	LTCC => Ca	0.9	1.4	0.5	L-type Ca channel increases Ca
middle	r83	MEF2 => mTor	0.9	1.4	0.5	MEF2 activates mTor
middle	r84	MEK36 => p38	0.9	1.4	0.5	MEK36 phosphorylates p38
middle	r85	MEK47 => JNK	0.9	1.4	0.5	MEK47 phosphorylates JNK
middle	r86	MEK47 => p38	0.9	1.4	0.5	MEK47 phosphorylates p38
middle	r87	MEK5 => ERK5	0.9	1.4	0.5	MEK5 phosphorylates ERK5
middle	r88	MEKK1 => MEK47	0.9	1.4	0.5	MEKK1 phosphorylates MEK4
middle	r89	MEKK23 => MEK5	0.9	1.4	0.5	MAP3K2 and MAP3K3 both phosphorylate MEK5
middle	r90	MEKK4 => MEK36	0.9	1.4	0.5	MEKK4 (MTK1) activates MEK3 and MEK6
middle	r91	MEKK4 => MEK47	0.9	1.4	0.5	MEKK4 phosphorylates MEK4
middle	r92	mTor => eIF4E	0.9	1.4	0.5	mTor phosphorylates a binding protein of eIF4E
middle	r93	mTor => p70s6k	0.9	1.4	0.5	mTor phosphorylates p70s6k
middle	r94	Na => NCX	0.9	1.4	0.5	Na leaves through NCX
middle	r95	NCX => Ca	0.9	1.4	0.5	NCX increases Ca
middle	r96	!NFAT => aMHC	0.9	1.4	0.5	NFAT inhibits aMHC transcription
middle	r97	!NFAT => SERCA	0.9	1.4	0.5	NFAT inhibits SERCA transcription
middle	r98	NHE => Na	0.9	1.4	0.5	NHE increases Na
middle	r99	NOS => sGC	0.9	1.4	0.5	NOS produces NO which activates sGC
middle	r101	p38 => IKK	0.9	1.4	0.5	p38 activates IKK
middle	r102	p38 => Lmcd1	0.9	1.4	0.5	p38 MAPK induces Lmcd1 expression
middle	r103	PDK1 => Akt	0.9	1.4	0.5	PDK1 activates Akt
middle	r104	PI3K => PDK1	0.9	1.4	0.5	PI3K activates PDK1
middle	r105	PKC => Raf1	0.9	1.4	0.5	PKC activates Raf1
middle	r106	!PKG1 & DAG => TRP	0.9	1.4	0.5	PKG1 inhibits IP3 DAG activates TRP
middle	r107	!PKG1 & PLC => IP3	0.9	1.4	0.5	PLC cleaves PIP2 to form IP3 and DAG
middle	r108	PLC => DAG	0.9	1.4	0.5	PLC cleaves PIP2 to form IP3 and DAG
middle	r109	Rac1 => MEKK4	0.9	1.4	0.5	Rac1 binds MEKK4
middle	r110	Raf1 => MEK12	0.9	1.4	0.5	Raf1 activates MEK12
middle	r111	Ras => MEKK1	0.9	1.4	0.5	Ras activates MEKK1
middle	r112	Ras => MEKK23	0.9	1.4	0.5	Ras activates MAP3K2 and MAP3K3
middle	r113	Ras => Rac1	0.9	1.4	0.5	Ras activates Rac1
middle	r114	Ras => Raf1	0.9	1.4	0.5	Ras activates Raf1
middle	r115	RhoA => MRTF	0.9	1.4	0.5	STARS and RhoA enhance actin polymerization, which allows for nuclear translocation of MRTF
middle	r116	RhoA => ROCK	0.9	1.4	0.5	RhoA binds to ROCK
middle	r117	RhoGEF => RhoA	0.9	1.4	0.5	RhoGEF activates RhoA
middle	r118	!ROCK & !Titin => FHL2	0.9	1.4	0.5	ROCK inhibits FHL2 Titin inhibits FHL2
middle	r119	sGC => cGMP	0.9	1.4	0.5	sGC converts GTP to cGMP

module	ID	rule	w	n	EC₅₀	notes
middle	r120	Talin => Actin	0.9	1.4	0.5	Talin links to Actin
middle	r121	Talin => Vinculin	0.9	1.4	0.5	Talin links to Vinculin
middle	r122	Titin => FHL1	0.9	1.4	0.5	Titin activates FHL1
middle	r123	!Titin & FoxO => MuRF	0.9	1.4	0.5	Titin inhibits MuRF FoxO transcriptionally regulates MuRF
middle	r124	TRP => Ca	0.9	1.4	0.5	Trp increases Ca
middle	r125	Vinculin => Actin	0.9	1.4	0.5	Vcl links to Actin

Appendix D

Validation relationships

This database includes a list of activity changes predicted by the model, as well as the corresponding observed changes from the experimental literature used for validation. For references for each reaction, see S1 Table in Tan *PLoS Comput. Biol.* 13(11), 2017.

ID	Input	Input 2	Input Code	Output	Valid	Measurement	Category
Akt_	Stretch		w(1)=0.7;	Akt		Increase	In-Int
AngII_	Stretch		w(1)=0.7;	AngII		Increase	In-Int
AP1_	Stretch		w(1)=0.7;	AP1		Increase	In-Int
Ca_	Stretch		w(1)=0.7;	Ca		Increase	In-Int
CaN_	Stretch		w(1)=0.7;	CaN		Increase	In-Int
cFos_	Stretch		w(1)=0.7;	cFos		Increase	In-Int
cJun_	Stretch		w(1)=0.7;	cJun		Increase	In-Int
cMyc_	Stretch		w(1)=0.7;	cMyc		Increase	In-Int
CREB_	Stretch		w(1)=0.7;	CREB		Increase	In-Int
Cx43_	Stretch		w(1)=0.7;	Cx43		Increase	In-Int
DAG_	Stretch		w(1)=0.7;	DAG		Increase	In-Int
EGFR_	Stretch		w(1)=0.7;	EGFR		Increase	In-Int
ERK12_	Stretch		w(1)=0.7;	ERK12		Increase	In-Int
FAK_	Stretch		w(1)=0.7;	FAK		Increase	In-Int
FHL1_	Stretch		w(1)=0.7;	FHL1		Increase	In-Int
GATA4_	Stretch		w(1)=0.7;	GATA4		Increase	In-Int
gp130_	Stretch		w(1)=0.7;	gp130		Increase	In-Int
GSK3b_	Stretch		w(1)=0.7;	GSK3b		Decrease	In-Int
IP3_	Stretch		w(1)=0.7;	IP3		Increase	In-Int
JAK_	Stretch		w(1)=0.7;	JAK		Increase	In-Int
JNK_	Stretch		w(1)=0.7;	JNK		Increase	In-Int
Lmcd1_	Stretch		w(1)=0.7;	Lmcd1		Increase	In-Int

ID	Input	Input 2	Input Code	Output	Valid	Measurement	Category
MEF2_	Stretch		w(1)=0.7;	MEF2		Increase	In-Int
MEK12_	Stretch		w(1)=0.7;	MEK12		Increase	In-Int
MLP_	Stretch		w(1)=0.7;	MLP		Increase	In-Int
MRTF_	Stretch		w(1)=0.7;	MRTF		Increase	In-Int
mTor_	Stretch		w(1)=0.7;	mTor		Increase	In-Int
MuRF_	Stretch		w(1)=0.7;	MuRF		Decrease	In-Int
NFAT_	Stretch		w(1)=0.7;	NFAT		Increase	In-Int
NFkB_	Stretch		w(1)=0.7;	NFkB		Increase	In-Int
NOS_	Stretch		w(1)=0.7;	NOS		Increase	In-Int
p38_	Stretch		w(1)=0.7;	p38		Increase	In-Int
p70s6k_	Stretch		w(1)=0.7;	p70s6k		Increase	In-Int
PI3K_	Stretch		w(1)=0.7;	PI3K		Increase	In-Int
PKC_	Stretch		w(1)=0.7;	PKC		Increase	In-Int
Rac1_	Stretch		w(1)=0.7;	Rac1		Increase	In-Int
Raf1_	Stretch		w(1)=0.7;	Raf1		Increase	In-Int
Ras_	Stretch		w(1)=0.7;	Ras		Increase	In-Int
RhoA_	Stretch		w(1)=0.7;	RhoA		Increase	In-Int
RhoGEF_	Stretch		w(1)=0.7;	RhoGEF		Increase	In-Int
Src_	Stretch		w(1)=0.7;	Src		Increase	In-Int
SRF_	Stretch		w(1)=0.7;	SRF		Increase	In-Int
STAT_	Stretch		w(1)=0.7;	STAT		Increase	In-Int
aMHC_	Stretch		w(1)=0.7;	aMHC		Decrease	In-Out
ANP_	Stretch		w(1)=0.7;	ANP		Increase	In-Out
Ao_	Stretch		w(1)=0.7;	Ao		Increase	In-Out
bMHC_	Stretch		w(1)=0.7;	bMHC		Increase	In-Out
BNP_	Stretch		w(1)=0.7;	BNP		Increase	In-Out
CellArea_	Stretch		w(1)=0.7;	CellArea		Increase	In-Out
PrSynth_	Stretch		w(1)=0.7;	PrSynth		Increase	In-Out
sACT_	Stretch		w(1)=0.7;	sACT		Increase	In-Out
SERCA_	Stretch		w(1)=0.7;	SERCA		Decrease	In-Out
ERK12_Akti	Stretch	Akti	w(1)=0.7; ymax(Akt)=0;	ERK12	ERK12_	Decrease	KO-Int
BNP_AP1i	Stretch	AP1i	w(1)=0.7; ymax(AP1)=0;	BNP	BNP_	No Change	KO-Int
ANP_AT1Ri	Stretch	AT1Ri	w(1)=0.7; ymax(AT1R)=0;	ANP	ANP_	Decrease	KO-Int
Ao_AT1Ri	Stretch	AT1Ri	w(1)=0.7; ymax(AT1R)=0;	Ao	Ao_	Decrease	KO-Int
BNP_AT1Ri	Stretch	AT1Ri	w(1)=0.7; ymax(AT1R)=0;	BNP	BNP_	Decrease	KO-Int
CellArea_AT1Ri	Stretch	AT1Ri	w(1)=0.7; ymax(AT1R)=0;	CellArea	CellArea_	Decrease	KO-Int
cFos_AT1Ri	Stretch	AT1Ri	w(1)=0.7; ymax(AT1R)=0;	cFos	cFos_	Decrease	KO-Int
cJun_AT1Ri	Stretch	AT1Ri	w(1)=0.7; ymax(AT1R)=0;	cJun	cJun_	No Change	KO-Int
Cx43_AT1Ri	Stretch	AT1Ri	w(1)=0.7; ymax(AT1R)=0;	Cx43	Cx43_	Decrease	KO-Int
ERK12_AT1Ri	Stretch	AT1Ri	w(1)=0.7; ymax(AT1R)=0;	ERK12	ERK12_	Decrease	KO-Int
JNK_AT1Ri	Stretch	AT1Ri	w(1)=0.7; ymax(AT1R)=0;	JNK	JNK_	Increase	KO-Int
Raf1_AT1Ri	Stretch	AT1Ri	w(1)=0.7; ymax(AT1R)=0;	Raf1	Raf1_	Decrease	KO-Int

ID	Input	Input 2	Input Code	Output	Valid	Measurement	Category
skAct_AT1Ri	Stretch	AT1Ri	w(1)=0.7; ymax(AT1R)=0;	sACT	sACT_	Decrease	KO-Int
STAT_AT1Ri	Stretch	AT1Ri	w(1)=0.7; ymax(AT1R)=0;	STAT	STAT_	Decrease	KO-Int
cFos_Cai	Stretch	Cai	w(1)=0.7; ymax(Ca)=0;	cFos	cFos_	Decrease	KO-Int
cJun_Cai	Stretch	Cai	w(1)=0.7; ymax(Ca)=0;	cJun	cJun_	No Change	KO-Int
STAT_Cai	Stretch	Cai	w(1)=0.7; ymax(Ca)=0;	STAT	STAT_	Decrease	KO-Int
ANP_CaNi	Stretch	CaNi	w(1)=0.7; ymax(CaN)=0;	ANP	ANP_	Decrease	KO-Int
BNP_EGFRi	Stretch	EGFRi	w(1)=0.7; ymax(EGFR)=0;	BNP	BNP_	Decrease	KO-Int
ERK12_EGFRi	Stretch	EGFRi	w(1)=0.7; ymax(EGFR)=0;	ERK12	ERK12_	Decrease	KO-Int
JNK_EGFRi	Stretch	EGFRi	w(1)=0.7; ymax(EGFR)=0;	JNK	JNK_	No Change	KO-Int
MEK12_EGFRi	Stretch	EGFRi	w(1)=0.7; ymax(EGFR)=0;	MEK12	MEK12_	Decrease	KO-Int
Ras_EGFRi	Stretch	EGFRi	w(1)=0.7; ymax(EGFR)=0;	Ras	Ras_	Decrease	KO-Int
ANP_ET1Ri	Stretch	ET1Ri	w(1)=0.7; ymax(ET1R)=0;	ANP	ANP_	Decrease	KO-Int
BNP_ET1Ri	Stretch	ET1Ri	w(1)=0.7; ymax(ET1R)=0;	BNP	BNP_	Decrease	KO-Int
cFos_ET1Ri	Stretch	ET1Ri	w(1)=0.7; ymax(ET1R)=0;	cFos	cFos_	Decrease	KO-Int
STAT_ET1Ri	Stretch	ET1Ri	w(1)=0.7; ymax(ET1R)=0;	STAT	STAT_	No Change	KO-Int
Akt_FAKi	Stretch	FAKi	w(1)=0.7; ymax(FAK)=0;	Akt	Akt_	Decrease	KO-Int
ANP_FAKi	Stretch	FAKi	w(1)=0.7; ymax(FAK)=0;	ANP	ANP_	Decrease	KO-Int
bMHC_FAKi	Stretch	FAKi	w(1)=0.7; ymax(FAK)=0;	bMHC	bMHC_	Decrease	KO-Int
CellArea_FAKi	Stretch	FAKi	w(1)=0.7; ymax(FAK)=0;	CellArea	CellArea_	Decrease	KO-Int
cJun_FAKi	Stretch	FAKi	w(1)=0.7; ymax(FAK)=0;	cJun	cJun_	Decrease	KO-Int
cMyc_FAKi	Stretch	FAKi	w(1)=0.7; ymax(FAK)=0;	cMyc	cMyc_	Decrease	KO-Int
ERK12_FAKi	Stretch	FAKi	w(1)=0.7; ymax(FAK)=0;	ERK12	ERK12_	Decrease	KO-Int
JNK_FAKi	Stretch	FAKi	w(1)=0.7; ymax(FAK)=0;	JNK	JNK_	Increase	KO-Int
MEF2_FAKi	Stretch	FAKi	w(1)=0.7; ymax(FAK)=0;	MEF2	MEF2_	Decrease	KO-Int
mTor_FAKi	Stretch	FAKi	w(1)=0.7; ymax(FAK)=0;	mTor	mTor	Decrease	KO-Int
p70s6K_FAKi	Stretch	FAKi	w(1)=0.7; ymax(FAK)=0;	p70s6k	p70s6k	Decrease	KO-Int
Src_FAKi	Stretch	FAKi	w(1)=0.7; ymax(FAK)=0;	Src	Src_	Decrease	KO-Int
RhoA_Ga1213i	Stretch	Ga1213i	w(1)=0.7; ymax(Ga1213)=0;	RhoA	RhoA_	Decrease	KO-Int
RhoGEF_Ga1213i	Stretch	Ga1213i	w(1)=0.7; ymax(Ga1213)=0;	RhoGEF	RhoGEF	Decrease	KO-Int
BNP_GATA4	Stretch	GATA4i	w(1)=0.7; ymax(GATA4)=0;	BNP	BNP_	Decrease	KO-Int
STAT_gp130i	Stretch	gp130i	w(1)=0.7; ymax(gp130)=0;	STAT	STAT_	Decrease	KO-Int
ERK12_Integrini	Stretch	Integrini	w(1)=0.7; ymax(Integrin)=0;	ERK12	ERK12_	Decrease	KO-Int
FAK_Integrini	Stretch	Integrini	w(1)=0.7; ymax(Integrin)=0;	FAK	FAK_	Decrease	KO-Int
JNK_Integrini	Stretch	Integrini	w(1)=0.7; ymax(Integrin)=0;	JNK	JNK_	Decrease	KO-Int
p38_Integrini	Stretch	Integrini	w(1)=0.7; ymax(Integrin)=0;	p38	p38_	Decrease	KO-Int
RhoA_Integrini	Stretch	Integrini	w(1)=0.7; ymax(Integrin)=0;	RhoA	RhoA_	Decrease	KO-Int
RhoGEF_Integrini	Stretch	Integrini	w(1)=0.7; ymax(Integrin)=0;	RhoGEF	RhoGEF	Decrease	KO-Int
STAT_JAKi	Stretch	JAKi	w(1)=0.7; ymax(JAK)=0;	STAT	STAT_	Decrease	KO-Int
ANP_JNKi	Stretch	JNKi	w(1)=0.7; ymax(JNK)=0;	ANP	ANP_	Decrease	KO-Int
Ao_JNKi	Stretch	JNKi	w(1)=0.7; ymax(JNK)=0;	Ao	Ao_	Increase	KO-Int
cJun_JNKi	Stretch	JNKi	w(1)=0.7; ymax(JNK)=0;	cJun	cJun_	Decrease	KO-Int
ERK12_JNKi	Stretch	JNKi	w(1)=0.7; ymax(JNK)=0;	ERK12	ERK12_	Decrease	KO-Int

ID	Input	Input 2	Input Code	Output	Valid	Measurement	Category
CellArea_Lmcd1i	Stretch	Lmcd1i	w(1)=0.7; ymax(Lmcd1)=0;	CellArea	CellArea_	Decrease	KO-Int
aMHC_LTCCi	Stretch	LTCCi	w(1)=0.7; ymax(LTCC)=0;	aMHC	aMHC_	Decrease	KO-Int
ANP_LTCCi	Stretch	LTCCi	w(1)=0.7; ymax(LTCC)=0;	ANP	ANP_	Decrease	KO-Int
bMHC_LTCCi	Stretch	LTCCi	w(1)=0.7; ymax(LTCC)=0;	bMHC	bMHC_	Decrease	KO-Int
Ca_LTCCi	Stretch	LTCCi	w(1)=0.7; ymax(LTCC)=0;	Ca	Ca_	Decrease	KO-Int
CaN_LTCCi	Stretch	LTCCi	w(1)=0.7; ymax(LTCC)=0;	CaN	CaN_	Decrease	KO-Int
PrSynth_LTCCi	Stretch	LTCCi	w(1)=0.7; ymax(LTCC)=0;	PrSynth	PrSynth_	Decrease	KO-Int
SERCA_LTCCi	Stretch	LTCCi	w(1)=0.7; ymax(LTCC)=0;	SERCA	SERCA_	No Change	KO-Int
BNP_MEK12	Stretch	MEK12i	w(1)=0.7; ymax(MEK12)=0;	BNP	BNP_	Decrease	KO-Int
Cx43_MEK13	Stretch	MEK12i	w(1)=0.7; ymax(MEK12)=0;	Cx43	Cx43_	Decrease	KO-Int
ERK12_MEK14	Stretch	MEK12i	w(1)=0.7; ymax(MEK12)=0;	ERK12	ERK12_	Decrease	KO-Int
BNP_MLPi	Stretch	MLPi	w(1)=0.7; ymax(MLP)=0;	BNP	BNP_	Decrease	KO-Int
NFAT_MLPi	Stretch	MLPi	w(1)=0.7; ymax(MLP)=0;	NFAT	NFAT_	Decrease	KO-Int
PrSynth_MLPi	Stretch	MLPi	w(1)=0.7; ymax(MLP)=0;	PrSynth	PrSynth_	Decrease	KO-Int
bMHC_MRTFi	Stretch	MRTFi	w(1)=0.7; ymax(MRTF)=0;	bMHC	bMHC_	Decrease	KO-Int
BNP_MRTFi	Stretch	MRTFi	w(1)=0.7; ymax(MRTF)=0;	BNP	BNP_	Decrease	KO-Int
ANP_NCXi	Stretch	NCXi	w(1)=0.7; ymax(NCX)=0;	ANP	ANP_	Decrease	KO-Int
CaN_NCXi	Stretch	NCXi	w(1)=0.7; ymax(NCX)=0;	CaN	CaN_	Decrease	KO-Int
PrSynth_NCXi	Stretch	NCXi	w(1)=0.7; ymax(NCX)=0;	PrSynth	PrSynth_	Decrease	KO-Int
ANP_NHEi	Stretch	NHEi	w(1)=0.7; ymax(NHE)=0;	ANP	ANP_	Decrease	KO-Int
CaN_NHEi	Stretch	NHEi	w(1)=0.7; ymax(NHE)=0;	CaN	CaN_	Decrease	KO-Int
ERK12_NHEi	Stretch	NHEi	w(1)=0.7; ymax(NHE)=0;	ERK12	ERK12_	Decrease	KO-Int
PrSynth_NHEi	Stretch	NHEi	w(1)=0.7; ymax(NHE)=0;	PrSynth	PrSynth_	Decrease	KO-Int
Raf1_NHEi	Stretch	NHEi	w(1)=0.7; ymax(NHE)=0;	Raf1	Raf1_	Decrease	KO-Int
STAT_NHEi	Stretch	NHEi	w(1)=0.7; ymax(NHE)=0;	STAT	STAT_	Decrease	KO-Int
Ao_p38i	Stretch	p38i	w(1)=0.7; ymax(p38)=0;	Ao	Ao_	Decrease	KO-Int
PrSynth_p38i	Stretch	p38i	w(1)=0.7; ymax(p38)=0;	PrSynth	PrSynth_	Decrease	KO-Int
Akt_PI3Ki	Stretch	PI3Ki	w(1)=0.7; ymax(PI3K)=0;	Akt	Akt_	Decrease	KO-Int
BNP_PI3Ki	Stretch	PI3Ki	w(1)=0.7; ymax(PI3K)=0;	BNP	BNP_	Decrease	KO-Int
ERK12_PI3Ki	Stretch	PI3Ki	w(1)=0.7; ymax(PI3K)=0;	ERK12	ERK12_	Decrease	KO-Int
JNK_PI3Ki	Stretch	PI3Ki	w(1)=0.7; ymax(PI3K)=0;	JNK	JNK_	No Change	KO-Int
NOS_PI3Ki	Stretch	PI3Ki	w(1)=0.7; ymax(PI3K)=0;	NOS	NOS_	Decrease	KO-Int
Ras_PI3Ki	Stretch	PI3Ki	w(1)=0.7; ymax(PI3K)=0;	Ras	Ras_	Decrease	KO-Int
cFos_PKCi	Stretch	PKCi	w(1)=0.7; ymax(PKC)=0;	cFos	cFos_	Decrease	KO-Int
Cx43_PKCi	Stretch	PKCi	w(1)=0.7; ymax(PKC)=0;	Cx43	Cx43_	No Change	KO-Int
ERK12_PKCi	Stretch	PKCi	w(1)=0.7; ymax(PKC)=0;	ERK12	ERK12_	Decrease	KO-Int
Raf1_PKCi	Stretch	PKCi	w(1)=0.7; ymax(PKC)=0;	Raf1	Raf1_	Decrease	KO-Int
STAT_PKCi	Stretch	PKCi	w(1)=0.7; ymax(PKC)=0;	STAT	STAT_	Decrease	KO-Int
Ca_PLCi	Stretch	PLCi	w(1)=0.7; ymax(PLC)=0;	Ca	Ca_	Decrease	KO-Int
cFos_PLCi	Stretch	PLCi	w(1)=0.7; ymax(PLC)=0;	cFos	cFos_	Decrease	KO-Int
IP3_PLCi	Stretch	PLCi	w(1)=0.7; ymax(PLC)=0;	IP3	IP3_	Decrease	KO-Int
ERK12_Rac1i	Stretch	Rac1i	w(1)=0.7; ymax(Rac1)=0;	ERK12	ERK12_	Decrease	KO-Int

ID	Input	Input 2	Input Code	Output	Valid	Measurement	Category
ERK12_Raf1i	Stretch	Raf1i	w(1)=0.7; ymax(Raf1)=0;	ERK12	ERK12_	Decrease	KO-Int
ERK12_Rasi	Stretch	Rasi	w(1)=0.7; ymax(Ras)=0;	ERK12	ERK12_	No Change	KO-Int
JNK_Rasi	Stretch	Rasi	w(1)=0.7; ymax(Ras)=0;	JNK	JNK_	No Change	KO-Int
MEK12_Rasi	Stretch	Rasi	w(1)=0.7; ymax(Ras)=0;	MEK12	MEK12_	Decrease	KO-Int
p38_Rasi	Stretch	Rasi	w(1)=0.7; ymax(Ras)=0;	p38	p38_	Decrease	KO-Int
Akt_RhoAi	Stretch	RhoAi	w(1)=0.7; ymax(RhoA)=0;	Akt	Akt_	Decrease	KO-Int
ANP_RhoAi	Stretch	RhoAi	w(1)=0.7; ymax(RhoA)=0;	ANP	ANP_	Decrease	KO-Int
bMHC_RhoAi	Stretch	RhoAi	w(1)=0.7; ymax(RhoA)=0;	bMHC	bMHC_	Decrease	KO-Int
BNP_RhoAi	Stretch	RhoAi	w(1)=0.7; ymax(RhoA)=0;	BNP	BNP_	Decrease	KO-Int
cFos_RhoAi	Stretch	RhoAi	w(1)=0.7; ymax(RhoA)=0;	cFos	cFos_	Decrease	KO-Int
ERK12_RhoAi	Stretch	RhoAi	w(1)=0.7; ymax(RhoA)=0;	ERK12	ERK12_	Decrease	KO-Int
FAK_RhoAi	Stretch	RhoAi	w(1)=0.7; ymax(RhoA)=0;	FAK	FAK_	Decrease	KO-Int
MRTF_RhoAi	Stretch	RhoAi	w(1)=0.7; ymax(RhoA)=0;	MRTF	MRTF_	Decrease	KO-Int
PrSynth_RhoAi	Stretch	RhoAi	w(1)=0.7; ymax(RhoA)=0;	PrSynth	PrSynth_	Decrease	KO-Int
sACT_RhoAi	Stretch	RhoAi	w(1)=0.7; ymax(RhoA)=0;	sACT	sACT_	Decrease	KO-Int
ANP_RhoGEFi	Stretch	RhoGEFi	w(1)=0.7; ymax(RhoGEF)=0;	ANP	ANP_	Decrease	KO-Int
bMHC_RhoGEFi	Stretch	RhoGEFi	w(1)=0.7; ymax(RhoGEF)=0;	bMHC	bMHC_	Decrease	KO-Int
CellArea_RhoGEFi	Stretch	RhoGEFi	w(1)=0.7; ymax(RhoGEF)=0;	CellArea	CellArea_	Decrease	KO-Int
MRTF_RhoGEFi	Stretch	RhoGEFi	w(1)=0.7; ymax(RhoGEF)=0;	MRTF	MRTF_	Decrease	KO-Int
RhoA_RhoGEFi	Stretch	RhoGEFi	w(1)=0.7; ymax(RhoGEF)=0;	RhoA	RhoA_	Decrease	KO-Int
ANP_Srci	Stretch	Srci	w(1)=0.7; ymax(Src)=0;	ANP	ANP_	Decrease	KO-Int
FAK_Srci	Stretch	Srci	w(1)=0.7; ymax(Src)=0;	FAK	FAK_	Decrease	KO-Int
p38_Srci	Stretch	Srci	w(1)=0.7; ymax(Src)=0;	p38	p38_	Decrease	KO-Int
MuRF_Titini	Stretch	Titini	w(1)=0.7; ymax(Titin)=0;	MuRF	MuRF_	Increase	KO-Int

Appendix E

Genes with multiple shRNAs above threshold for area

Genes with 2, 3, 4, or 5 distinct shRNAs displaying a median cell area above 95th percentile (1,579 μm^2) are indicated, using the following key:

2 shRNAs above; **3 shRNAs above**; 4 shRNAs above; 5 shRNAs above

1110001D15Rik	9030224M15Rik	Ahnak	B3galt5
1110004E09Rik	9130022K13Rik	Akr1c6	B630005N14Rik
1110032A04Rik	9830123M21Rik	Alk	BC002163
1700016G05Rik	9830147P19Rik	Ankfy1	BC048546
2310014L17Rik	A330008L17Rik	Ankrd2	BC049762
2510005D08Rik	A830031A19Rik	Anp32e	Bag5
2610034B18Rik	AW491445	Ap1g1	Bak1
2610204M08Rik	Abcc10	Ap1s3	Bcl9l
2810401C16Rik	Abcc3	Apom	Birc4
4921509E07Rik	Abtb1	Aqp11	Bmi1
4930542C12Rik	Acadvl	Aqp7	Btc
4930578I06Rik	Acox3	Arhgap12	C030002J06Rik
4930595M18Rik	Acta1	Arid5b	C330023M02Rik
4931414P19Rik	Adam10	Atf4	C330049O21Rik
4933421I07Rik	Adcy8	Atg4c	C6
5830443L24Rik	Ahctf1	Aven	Carhsp1

Carm1	Ecel1	Hes7	Mmp15
Cbx6-Nptxr	Ecg2	Hexdc	Mmp25
Ccbl2	Edf1	Hif1an	Mtfmt
Cd33	Efhc2	Hnrpab	Mybpc3
Cd40	Efs	Hsp90ab1	My11
Cdv3	Eomes	Htr3b	Myst2
Chd6	Epo	Ibtk	<u>Ndufaf4</u>
Cldn11	F8	Ier3	Nhlrc3
Clec2d	Fabp3	Ifit3	Nkx2-9
Clec4a4	Fam110b	Il2	Nlrc4
Cnga3	Fam123a	Insl6	Nova2
Cnr2	Fath2	Irak3	Npl
Col18a1	Fbln5	Itgb8	Nudcd1
Col4a3	Fbx14	Kenk9	Nup155
Col9a1	Fgd4	Kctd4	Nxph2
Cops6	Fkbp8	Kifc2	Olfr1009
Coro6	Fmn1	Klk1b8	Olfr1226
Cox17	Frrs1	Krt222	Olfr1231
Cplx1	Fuca2	Lass2	Olfr1423
Cxcl12	Gabrp	Limk2	Olfr1484
D330012D11Rik	Galnt13	Lims1	Olfr181
Dapk1	Gbp2	Lmf1	Olfr199
Dclre1c	Ghrhr	Lnx1	Olfr266
Defcr6	Gm1280	Lrrc57	Olfr403
Des	Gm1890	Ltbp1	Olfr491
Dffa	Gm270	Ltbp2	Olfr605
Dhx29	Gm443	Magea4	Olfr677
Dhx30	Gm4876	Magi3	Olfr984
Dhx33	Gm711	Map2k4	Omg
Dnajc5b	Gnb211	Map3k9	Oosp1
Doc2b	Gnl2	Mbd3	Osbpl5
Dock3	Gpbp1	Med22	Osbpl6
Dub1a	Gpr158	Mesp2	Osgpl1
Dync11i2	Gpx3	Mib2	Otof
E430002G05Rik	Hc	Mid1ip1	Otub1

P2ry1	Psmb5	Slc39a8	Trib3
Pard6g	Psmb6	Slc6a15	Ttn
Pbk	Psmb7	Sltn	Ttyh1
Pcdhga1	Psors1c2	Smtn	Ugcg
Pde4dip	Ptger3	Socs5	Usp16
Pebp1	Ptk9	Sorcs3	Usp32
Perp	Raet1c	Spock2	Usp38
Pgr	Rap2a	Spp2	V1ra3
Phactr3	Rbp2	Stk40	Vmn1r203
Pigb	Ren1	Suv420h2	Vmn2r23
Pigf	Rffl	Svs3b	Vrk2
Pigt	Rpa2	Syn2	Wdr25
Plekhg2	Rpgrip1	Sypl	Wnk1
Pllp	Rph3al	Tcf12	Xbp1
Polr3b	Rslcan24	Tgm3	Zc3h14
Pou4f3	Scube1	Timm8b	Zfp101
Ppp2r4	Sdf2	Tlx3	Zfp277
Pramel4	Sept11	Tmed6	Zfp286
Prkaca	Serinc1	Tmem116	Zfp316
Prlpb	Serpina3n	Tmem149	Zfp329
Proc	Sertad1	Tmem177	Znrd1
Prok2	Slc27a3	Tmem2	
Prss8	Slc35b3	Tnfsf9	

Appendix F

Genes with multiple shRNAs above threshold for elongation

Genes with 2, 3, 4, or 5 distinct shRNAs displaying a mean elongation above 95th percentile (2.12) are indicated, using the following key:

2 shRNAs above; **3 shRNAs above**; 4 shRNAs above; 5 shRNAs above

0610010D20Rik	4931419K03Rik	Aldh9a1	Bace2
0610042E07Rik	4932411N23Rik	Angptl4	Bdh1
1110001D15Rik	4933424A10Rik	Ap1m1	Bet1
1110004E09Rik	4933425M15Rik	Armex1	Bivm
1300007L22Rik	4933430I17Rik	Asb12	Brms1
1700001J03Rik	6230409E13Rik	Ascl3	Bscl2
1700001P01Rik	6330403K07Rik	Asphd2	C130022K22Rik
1700016D06Rik	9130023D20Rik	Astn1	Cab39l
1700021F05Rik	9230119C12Rik	Atp11b	Car5a
1810014F10Rik	AU021034	Attp	Cav1
2310056P07Rik	Acly	B3gat2	Ccdc28b
2310057N15Rik	Acta1	BC010787	Ccdc85a
2810046M22Rik	Adam1a	BC030476	Ccl11
4833420G17Rik	Adam1b	BC036313	Cct5
4921507P07Rik	Add2	BC089491	Cd109
4930532D21Rik	Aif1l	BC089597	Cd80

Cdadc1	Dennd1b	Gdpd4	Llg1
Cdc14a	Diras1	Gm4884	Lrrc24
Cdc14b	Dnaje5b	Gm5084	Lrrc46
Cdc5l	Dnmt1	Gm5388	Lrrtm3
Ceacam1	Dsp	Gm608	Ly6a
Cfp	Dusp7	Gng12	Lyplal1
Chchd7	Dvl2	Golga7	Lysmd4
Chic1	E330009J07Rik	Gpr157	Mapre2
Clcf1	E330039K12Rik	Gpr82	March6
Cldn19	Eaf2	Gsn	March8
Clec2e	Ear2	Gzmc	Matn2
Clgn	Ear4	Hdlbp	Mbl2
Col1a1	Ece2	Helb	Med8
Cops8	Ecg2	Herpud1	Mfn1
Cox7b2	Edaradd	Hkdc1	Mipep
Cpsf3l	Eed	Hsd17b12	Mlf2
Cryz11	Efemp1	Hsf2	Mmp17
Csf1r	Eif3s3	Hydin	Mrfap1
Ctdspl2	Emcn	Ifi204	Mrs2
Ctnna1	Emr4	Ifna12	Msx1
Cul2	Entpd1	Igfbp7	Mthfd2
Cutc	Eprs	Impact	Mtmr11
Cyb561d2	Eps8	Irak1	Mtmr6
Cyb5r4	Ethe1	Irf8	Mucedhl
Cyp1a2	Etnk2	Itga11	Mypop
Cyp3a44	Exoc7	Jmjd4	Naca
Cyp7a1	F10	Klk1b1	Nap112
D0H4S114	F12	Klrb1c	Nckipsd
D15Ertd621e	F3	Kptn	Nek4
D230025D16Rik	Fam114a1	Krtap12-1	Nin
D430018E03Rik	Fam20a	LOC239191	Nol12
D830046C22Rik	Fermt1	LOC547343	Npr3
D8Ertd354e	Fgl1	Ldb3	Ntn1
Dazap1	Flot2	Leprot	Nudt7
Dbnnd1	Gale	Lgi2	Numbl

Nup35	Pam	Rg9mtd2	Sprr2j-ps
ORF28	Pcdhb11	Rgmb	Srcin1
Olfr1031	Pcdhb3	Rgs2	Srebf2
Olfr1040	Pcdhga3	Rhod	St6galnac6
Olfr1101	Pde1a	Rhox5	Stam2
Olfr1121	Pde1c	Rmnd5a	Sv2a
Olfr1123	Pdim3	Rnaseh2c	Sytl5
Olfr1124	Pfpl	Rnf152	Taar5
Olfr1213	Phb2	Rpia	Taf10
Olfr1242	Phf17	Rpl36	Tagap
Olfr1289	Pknox1	Rps19	Tas2r118
Olfr1305	Plekho1	Rps24	Tcfe2a
Olfr1333	Plin4	Rpusd2	Tekt1
Olfr1408	Plxna4	Rrad	Tex13
Olfr1451	Podnl1	Rras2	Tex15
Olfr196	Polr3b	Rrh	Tfip11
Olfr2	Pramel4	Rtcd1	Tgfb2
Olfr209	Prkcbp1	Rtp4	Thap3
Olfr314	Proc	Scg5	Thoc4
Olfr441	Prok2	Scn3a	Tlm
Olfr470	Prpf19	Scn4b	Tmc4
Olfr554	Psmc3	Scube2	Tmem108
Olfr582	Ptafr	Serpib6a	Tmem33
Olfr694	Ptprk	Sh3glb1	Tmem63c
Olfr697	Pus1	Siglecf	Tnfaip6
Olfr715	Pus3	Skint2	Tnn
Olfr768	Rab11fip1	Skint4	Tnnc2
Olfr871	Rabep1	Slc22a5	Tom112
Olfr900	Raet1a	Slc25a14	Trappc6b
Olfr904	Raet1d	Slc25a46	Twist2
Olfr924	Ralgds	Slmap	Ubl4b
Olfr945	Rassf1	Snap29	Ugt1a6b
Olfr978	Rb1	Snx4	Ubp1
Osbp16	Rbbp9	Socs5	Umps
Pah	Rbm4b	Spata16	Unc13a

Usp46	Whrn	Zc3h14	Zfp535
V1rc10	X83328	Zdhhc12	Zfp654
V1rc28	X99384	Zfp143	Zfp7
V1rg11	Zbtb40	Zfp422-rs1	Znrf1

Appendix G

Genes with multiple shRNAs above threshold for spikiness

Genes with 2, 3, 4, or 5 distinct shRNAs displaying a mean spikiness above 95th percentile (7.86) are indicated, using the following key:

2 shRNAs above; **3 shRNAs above**; 4 shRNAs above; 5 shRNAs above

1200009I06Rik	<u>Abcg5</u>	BC049762	Cd300e
<u>1700081D17Rik</u>	Acpp	BC061237	Cdx1
1700128F08Rik	Acta1	BC066135	Chx10
1810022C23Rik	Acvr1b	Bcas2	Clec16a
2210012G02Rik	Acvr1l	Bcl2a1b	Clec1a
2310002J15Rik	Aig1	Birc1b	Clec4b1
2610109H07Rik	Aipl1	Bmper	Clm3
4921511C20Rik	<u>Alg5</u>	C920008G01Rik	Cnn3
4921524J06Rik	Aph1a	Cab39	Cnot8
4930417M19Rik	Aph1b	Cacna1s	Cntfr
4930563M21Rik	Apoc1	Cacnb2	Col4a3
4930566A11Rik	Apom	Camkk1	Coro7
4932701A20Rik	Arhgef3	Camp	Cplx1
<u>5830443L24Rik</u>	Art3	Cap2	Cpne2
5930416I19Rik	Art4	Casq2	Creb3l4
9430015G10Rik	Astn1	Cav3	Crtc2
9830147J24Rik	B230359F08Rik	Ccdc18	Cryab
<u>A4galt</u>	B3gnt9	Ccdc99	Csk
A730008L03Rik	BC020535	Ccin	Csn1s1
Abca16	BC048599	Ccn1l	Ctnna2

Ctnn	Fanci	Hdc	Lman2
D10Wsu52e	Fath2	Hemgn	Lmod3
D15Ert621e	Fbln5	Hes7	<u>Lnx1</u>
D830007F02Rik	Fbn1	Hist1h1c	<u>Ly9</u>
Dak	Fbxo5	Hist1h2ab	Mageb17
Dapk3	Fgd1	Hist1h2ae	Manba
Dbc1	Fgf12	Hnrph2	Map2k4
Dbi	Fgfr2	Hnrpl1	Mapkapk2
Dbil5	Fhdc1	Hsf2	Mbd6
Dbt	Fign	Hyi	Mcoln1
<u>Ddx20</u>	Fliih	Igfbp2	Mea1
Ddx6	Flot2	Igfbp5	Mfn1
Defb9	Fn3k	Iigp2	Mip
Defcr22	Fras1	Ik	Mras
Defcr6	Galnt1	Ing1	Mrps17
Disc1	Galnt5	Itm2a	Ms4a6b
Dnaja3	Gatm	Jph4	Ms4a7
Dnajib11	Gbp2	Jub	Mta1
Dnaje9	Gga3	Kcne1	Mtl5
Doc2a	Glt8d1	Kcnj12	<u>Nadsyn1</u>
Dppa2	Gltp	Kctd13	Nanos1
Dscr1	Gm1890	Kdelr3	<u>Nckap1</u>
Dusp28	Gm5308	Kif9	Nek9
E130304F04Rik	Gmfb	Klhl5	Nid1
Efcab4a	Gnas	Klrc2	Nin
Efemp1	Gnat2	Kpna3	Nol9
Efemp2	Gpc1	Krtap21-1	Npas3
Enpp6	Gpr160	LOC236413	Nr2f2
Erc3	Gpre6a	LOC381806	Nr4a3
Etnk1	Grm3	LOC434782	Nxph2
Eva1	Gstm5	<u>LOC546214</u>	Odam
<u>Exoc3</u>	Gypa	Ldb3	Olfr1110
Exoc4	Gys3	Lhx5	Olfr1423
Exoc6	Hand1	Lin54	Olfr1453
F630003A18Rik	Havcr2	Lin9	Olfr169

Olfr228	Pxmp2	Srr	Tshr
Olfr25	Rab3il1	Ssbp4	Tspan11
Olfr371	Rbl1	St6galnac4	Tssk6
Olfr521	Rbm7	Stab2	Ttpal
Olfr774	Rgl2	Stag2	Tubal3
Olfr993	Rgma	Stk39	Tubgcp2
Osbp15	Rgr	Stx5a	Twist2
Otof	Rhag	Sult2b1	Ugcg
Pank3	Rin3	Surb7	Ugt1a2
Pccb	Rnf145	Sybl1	Ugt2b37
Pctp	Rock1	Syne1	Ugt2b5
Pdcd4	Rock2	Sypl	Ugt3a1
Pdgfr1	Rpgr	Taok2	Ugt8a
Pdzd4	Rsad2	Tbce	Usf1
Phlpp1	Rsrc1	Tceb1	Usp-ps
Pigo	Ryr3	Timd4	V1ra3
Pigt	Scube1	Tkt	V1rg3
Pik4ca	Sec1	Tle6	Vipr1
Pkd211	Sec61a2	Tlx3	Vps4b
Plekhh2	Sema4b	Tmed10	Vrk2
Pnkp	Sergef	Tmem24	Vrk3
Pold2	Sf4	Tnfaip2	Vsnl1
Polr3b	Sgta	Tnfaip6	Vti1b
Polr3h	Slc12a7	Tnnc1	Wdr57
Pqbp1	Slc29a3	Tnnt2	Xpa
Prdx2	Slc2a12	Tpm1	Zdhhc2
Prlpn	Slc35d3	Trappc6b	Zfp64
Prm3	Slc40a1	Triap1	Zfpm2
Pscd3	Slc5a6	Trim38	Zmym1
Pten	Sphk2	Trim45	
Ptx3	Src	Trip6	
Pvr11	Srprb	Tscot	

References

- [1] A. P. Ambrosy *et al.*, “The global health and economic burden of hospitalizations for heart failure: lessons learned from hospitalized heart failure registries,” *J. Am. Coll. Cardiol.*, vol. 63, no. 12, pp. 1123–1133, Apr. 2014.
- [2] D. Mozaffarian *et al.*, “Heart Disease and Stroke Statistics-2016 Update: A Report From the American Heart Association,” *Circulation*, vol. 133, no. 4, pp. e38–60, Jan. 2016.
- [3] P. A. Heidenreich *et al.*, “Forecasting the future of cardiovascular disease in the United States: a policy statement from the American Heart Association,” *Circulation*, vol. 123, no. 8, pp. 933–944, Mar. 2011.
- [4] J. Heineke and J. D. Molkentin, “Regulation of cardiac hypertrophy by intracellular signalling pathways,” *Nat. Rev. Mol. Cell Biol.*, vol. 7, no. 8, pp. 589–600, Aug. 2006.
- [5] D. G. Kramer, T. A. Trikalinos, D. M. Kent, G. V. Antonopoulos, M. A. Konstam, and J. E. Udelson, “Quantitative evaluation of drug or device effects on ventricular remodeling as predictors of therapeutic effects on mortality in patients with heart failure and reduced ejection fraction: a meta-analytic approach,” *J. Am. Coll. Cardiol.*, vol. 56, no. 5, pp. 392–406, Jul. 2010.
- [6] J. L. Hellawell and K. B. Margulies, “Myocardial reverse remodeling,” *Cardiovasc. Ther.*, vol. 30, no. 3, pp. 172–181, Jun. 2012.
- [7] J. Lindenfeld *et al.*, “HFSA 2010 Comprehensive Heart Failure Practice Guideline,” *J. Card. Fail.*, vol. 16, no. 6, pp. e1–194, Jun. 2010.
- [8] D. L. Mann and M. R. Bristow, “Mechanisms and models in heart failure: the biomechanical model and beyond,” *Circulation*, vol. 111, no. 21, pp. 2837–2849, May 2005.
- [9] M. Dandel *et al.*, “Prediction of cardiac stability after weaning from left ventricular assist devices in patients with idiopathic dilated cardiomyopathy,” *Circulation*, vol. 118, no. 14 Suppl, pp. S94–105, Sep. 2008.
- [10] C. K. McIlvennan, K. H. Magid, A. V. Ambardekar, J. S. Thompson, D. D. Matlock, and L. A. Allen, “Clinical outcomes after continuous-flow left ventricular assist device: a systematic review,” *Circ. Heart Fail.*, vol. 7, no. 6, pp. 1003–1013, Nov. 2014.
- [11] E. J. Birks *et al.*, “Left ventricular assist device and drug therapy for the reversal of heart failure,” *N. Engl. J. Med.*, vol. 355, no. 18, pp. 1873–1884, Nov. 2006.
- [12] E. Braunwald, “The war against heart failure: the Lancet lecture,” *Lancet Lond. Engl.*, vol. 385, no. 9970, pp. 812–824, Feb. 2015.
- [13] J. J. V. McMurray *et al.*, “Angiotensin-neprilysin inhibition versus enalapril in heart failure,” *N. Engl. J. Med.*, vol. 371, no. 11, pp. 993–1004, Sep. 2014.
- [14] P. S. Jhund *et al.*, “Independence of the blood pressure lowering effect and efficacy of the angiotensin receptor neprilysin inhibitor, LCZ696, in patients with heart failure with preserved ejection fraction: an analysis of the PARAMOUNT trial,” *Eur. J. Heart Fail.*, vol. 16, no. 6, pp. 671–677, Jun. 2014.
- [15] W. Grossman, D. Jones, and L. P. McLaurin, “Wall stress and patterns of hypertrophy in the human left ventricle,” *J. Clin. Invest.*, vol. 56, no. 1, pp. 56–64, Jul. 1975.
- [16] K. Berenji, M. H. Drazner, B. A. Rothermel, and J. A. Hill, “Does load-induced ventricular hypertrophy progress to systolic heart failure?,” *Am. J. Physiol. Heart Circ. Physiol.*, vol. 289, no. 1, pp. H8–H16, Jul. 2005.

- [17] K. A. Ryall, V. J. Bezzerides, A. Rosenzweig, and J. J. Saucerman, "Phenotypic screen quantifying differential regulation of cardiac myocyte hypertrophy identifies CITED4 regulation of myocyte elongation," *J. Mol. Cell. Cardiol.*, vol. 72, pp. 74–84, Jul. 2014.
- [18] H. Lal, S. K. Verma, H. B. Golden, D. M. Foster, A. M. Holt, and D. E. Dostal, "Molecular signaling mechanisms of myocardial stretch: Implications for heart disease," in *Mechanosensitivity of the Heart*, Book, Section vols., A. Kamkin and I. Kiseleva, Eds. Springer, Berlin, 2010, pp. 55–81.
- [19] D. Zablocki and J. Sadoshima, "Solving the cardiac hypertrophy riddle: The angiotensin II-mechanical stress connection," *Circ. Res.*, vol. 113, no. 11, pp. 1192–1195, Nov. 2013.
- [20] J. D. Molkentin and G. W. Dorn, "Cytoplasmic signaling pathways that regulate cardiac hypertrophy," *Annu. Rev. Physiol.*, vol. 63, pp. 391–426, 2001.
- [21] B. Fiedler and K. C. Wollert, "Interference of antihypertrophic molecules and signaling pathways with the Ca²⁺-calcineurin-NFAT cascade in cardiac myocytes," *Cardiovasc. Res.*, vol. 63, no. 3, pp. 450–457, Aug. 2004.
- [22] T. Aoyagi and T. Matsui, "Phosphoinositide-3 kinase signaling in cardiac hypertrophy and heart failure," *Curr. Pharm. Des.*, vol. 17, no. 18, pp. 1818–1824, 2011.
- [23] I. Kehat and J. D. Molkentin, "Extracellular signal-regulated kinase 1/2 (ERK1/2) signaling in cardiac hypertrophy," *Ann. N. Y. Acad. Sci.*, vol. 1188, pp. 96–102, Feb. 2010.
- [24] M. S. Marber, B. Rose, and Y. Wang, "The p38 mitogen-activated protein kinase pathway—a potential target for intervention in infarction, hypertrophy, and heart failure," *J. Mol. Cell. Cardiol.*, vol. 51, no. 4, pp. 485–490, Oct. 2011.
- [25] Q. Liang and J. D. Molkentin, "Redefining the roles of p38 and JNK signaling in cardiac hypertrophy: dichotomy between cultured myocytes and animal models," *J. Mol. Cell. Cardiol.*, vol. 35, no. 12, pp. 1385–1394, Dec. 2003.
- [26] H. Taegtmeyer, S. Sen, and D. Vela, "Return to the fetal gene program: a suggested metabolic link to gene expression in the heart," *Ann. N. Y. Acad. Sci.*, vol. 1188, pp. 191–198, Feb. 2010.
- [27] K. A. Ryall, D. O. Holland, K. A. Delaney, M. J. Kraeutler, A. J. Parker, and J. J. Saucerman, "Network reconstruction and systems analysis of cardiac myocyte hypertrophy signaling," *J. Biol. Chem.*, vol. 287, no. 50, pp. 42259–42268, Dec. 2012.
- [28] S. Sciarretta and J. Sadoshima, "New insights into the molecular phenotype of eccentric hypertrophy," *J. Mol. Cell. Cardiol.*, vol. 49, no. 2, pp. 153–156, Aug. 2010.
- [29] N. Takahashi *et al.*, "Hypertrophic responses to cardiotrophin-1 are not mediated by STAT3, but via a MEK5-ERK5 pathway in cultured cardiomyocytes," *J. Mol. Cell. Cardiol.*, vol. 38, no. 1, pp. 185–192, Jan. 2005.
- [30] R. L. Nicol, N. Frey, G. Pearson, M. Cobb, J. Richardson, and E. N. Olson, "Activated MEK5 induces serial assembly of sarcomeres and eccentric cardiac hypertrophy," *EMBO J.*, vol. 20, no. 11, pp. 2757–2767, Jun. 2001.
- [31] Y. Nakaoka *et al.*, "SHP2 mediates gp130-dependent cardiomyocyte hypertrophy via negative regulation of skeletal alpha-actin gene," *J. Mol. Cell. Cardiol.*, vol. 49, no. 2, pp. 157–164, Aug. 2010.
- [32] R. Kimura *et al.*, "Identification of cardiac myocytes as the target of interleukin 11, a cardioprotective cytokine," *Cytokine*, vol. 38, no. 2, pp. 107–115, May 2007.
- [33] N. López, J. Díez, and M. A. Fortuño, "Differential hypertrophic effects of cardiotrophin-1 on adult cardiomyocytes from normotensive and spontaneously hypertensive rats," *J. Mol. Cell. Cardiol.*, vol. 41, no. 5, pp. 902–913, Nov. 2006.
- [34] Y. Abe *et al.*, "Leptin induces elongation of cardiac myocytes and causes eccentric left ventricular dilatation with compensation," *Am. J. Physiol. Heart Circ. Physiol.*, vol. 292, no. 5, pp. H2387–2396, May 2007.
- [35] Y. Kuramochi, X. Guo, and D. B. Sawyer, "Neuregulin activates erbB2-dependent src/FAK signaling and cytoskeletal remodeling in isolated adult rat cardiac myocytes," *J. Mol. Cell. Cardiol.*, vol. 41, no. 2, pp. 228–235, Aug. 2006.

- [36] J. B. Strait, J. L. Martin, A. Bayer, R. Mestril, D. M. Eble, and A. M. Samarel, "Role of protein kinase C-epsilon in hypertrophy of cultured neonatal rat ventricular myocytes," *Am. J. Physiol. Heart Circ. Physiol.*, vol. 280, no. 2, pp. H756-766, Feb. 2001.
- [37] B. Russell, M. W. Curtis, Y. E. Koshman, and A. M. Samarel, "Mechanical stress-induced sarcomere assembly for cardiac muscle growth in length and width," *J. Mol. Cell. Cardiol.*, vol. 48, no. 5, pp. 817-823, May 2010.
- [38] T. Lecuit and P.-F. Lenne, "Cell surface mechanics and the control of cell shape, tissue patterns and morphogenesis," *Nat. Rev. Mol. Cell Biol.*, vol. 8, no. 8, pp. 633-644, Aug. 2007.
- [39] G. R. X. Hickson, A. Echard, and P. H. O'Farrell, "Rho-kinase controls cell shape changes during cytokinesis," *Curr. Biol. CB*, vol. 16, no. 4, pp. 359-370, Feb. 2006.
- [40] T. Nagai *et al.*, "Cdc42 plays a critical role in assembly of sarcomere units in series of cardiac myocytes," *Biochem. Biophys. Res. Commun.*, vol. 305, no. 4, pp. 806-810, Jun. 2003.
- [41] J. J. Dowling, A. P. Vreede, S. Kim, J. Golden, and E. L. Feldman, "Kindlin-2 is required for myocyte elongation and is essential for myogenesis," *BMC Cell Biol.*, vol. 9, p. 36, Jul. 2008.
- [42] M. J. McGrath, C. A. Mitchell, I. D. Coghill, P. A. Robinson, and S. Brown, "Skeletal muscle LIM protein 1 (SLIM1/FHL1) induces alpha 5 beta 1-integrin-dependent myocyte elongation," *Am. J. Physiol. Cell Physiol.*, vol. 285, no. 6, pp. C1513-1526, Dec. 2003.
- [43] D. D. Hall *et al.*, "Ectopic expression of Cdk8 induces eccentric hypertrophy and heart failure," *JCI Insight*, vol. 2, no. 15, Aug. 2017.
- [44] H. T. H. Au, I. Cheng, M. F. Chowdhury, and M. Radisic, "Interactive effects of surface topography and pulsatile electrical field stimulation on orientation and elongation of fibroblasts and cardiomyocytes," *Biomaterials*, vol. 28, no. 29, pp. 4277-4293, Oct. 2007.
- [45] G. Földes *et al.*, "Modulation of human embryonic stem cell-derived cardiomyocyte growth: a testbed for studying human cardiac hypertrophy?," *J. Mol. Cell. Cardiol.*, vol. 50, no. 2, pp. 367-376, Feb. 2011.
- [46] I. Kehat *et al.*, "Extracellular signal-regulated kinases 1 and 2 regulate the balance between eccentric and concentric cardiac growth," *Circ. Res.*, vol. 108, no. 2, pp. 176-183, Jan. 2011.
- [47] I. Komuro *et al.*, "Stretching cardiac myocytes stimulates protooncogene expression," *J. Biol. Chem.*, vol. 265, no. 7, pp. 3595-3598, Mar. 1990.
- [48] A. M. Gerdes, "The use of isolated myocytes to evaluate myocardial remodeling," *Trends Cardiovasc. Med.*, vol. 2, no. 4, pp. 152-155, Aug. 1992.
- [49] A. W. Orr, B. P. Helmke, B. R. Blackman, and M. A. Schwartz, "Mechanisms of mechanotransduction," *Dev. Cell*, vol. 10, no. 1, pp. 11-20, Jan. 2006.
- [50] D. E. Jaalouk and J. Lammerding, "Mechanotransduction gone awry," *Nat. Rev. Mol. Cell Biol.*, vol. 10, no. 1, pp. 63-73, Jan. 2009.
- [51] D. E. Dostal *et al.*, "Mechanosensing and Regulation of Cardiac Function," *J. Clin. Exp. Cardiol.*, vol. 5, no. 6, p. 314, Jun. 2014.
- [52] J. Sadoshima, Y. Xu, H. S. Slayter, and S. Izumo, "Autocrine release of angiotensin II mediates stretch-induced hypertrophy of cardiac myocytes in vitro," *Cell*, vol. 75, no. 5, pp. 977-984, Dec. 1993.
- [53] S. Miyata, T. Haneda, J. Osaki, and K. Kikuchi, "Renin-angiotensin system in stretch-induced hypertrophy of cultured neonatal rat heart cells," *Eur. J. Pharmacol.*, vol. 307, no. 1, pp. 81-88, Jun. 1996.
- [54] T. Yamazaki, I. Komuro, and Y. Yazaki, "Molecular aspects of mechanical stress-induced cardiac hypertrophy," *Mol. Cell. Biochem.*, vol. 163-164, pp. 197-201, Nov. 1996.
- [55] R. Aikawa *et al.*, "Rho family small G proteins play critical roles in mechanical stress-induced hypertrophic responses in cardiac myocytes," *Circ. Res.*, vol. 84, no. 4, pp. 458-466, Mar. 1999.
- [56] C. D. McWhinney, R. A. Hunt, K. M. Conrad, D. E. Dostal, and K. M. Baker, "The type I angiotensin II receptor couples to Stat1 and Stat3 activation through Jak2 kinase in neonatal rat cardiac myocytes," *J. Mol. Cell. Cardiol.*, vol. 29, no. 9, pp. 2513-2524, Sep. 1997.

- [57] J. Pan *et al.*, “Mechanical stretch activates the JAK/STAT pathway in rat cardiomyocytes,” *Circ. Res.*, vol. 84, no. 10, pp. 1127–1136, May 1999.
- [58] A. J. van Wamel, C. Ruwhof, L. E. van der Valk-Kokshoom, P. I. Schrier, and A. van der Laarse, “The role of angiotensin II, endothelin-1 and transforming growth factor-beta as autocrine/paracrine mediators of stretch-induced cardiomyocyte hypertrophy,” *Mol. Cell. Biochem.*, vol. 218, no. 1–2, pp. 113–124, Feb. 2001.
- [59] Y. Zou *et al.*, “Mechanical stress activates angiotensin II type 1 receptor without the involvement of angiotensin II,” *Nat. Cell Biol.*, vol. 6, no. 6, pp. 499–506, Jun. 2004.
- [60] K. Rakesh, B. Yoo, I.-M. Kim, N. Salazar, K.-S. Kim, and H. A. Rockman, “beta-Arrestin-biased agonism of the angiotensin receptor induced by mechanical stress,” *Sci. Signal.*, vol. 3, no. 125, p. ra46, 2010.
- [61] W. Tang, R. T. Strachan, R. J. Lefkowitz, and H. A. Rockman, “Allosteric modulation of β -arrestin-biased angiotensin II type 1 receptor signaling by membrane stretch,” *J. Biol. Chem.*, vol. 289, no. 41, pp. 28271–28283, Oct. 2014.
- [62] G. Jiang *et al.*, “Identification of Amino Acid Residues in Angiotensin II Type 1 Receptor Sensing Mechanical Stretch and Function in Cardiomyocyte Hypertrophy,” *Cell. Physiol. Biochem. Int. J. Exp. Cell. Physiol. Biochem. Pharmacol.*, vol. 37, no. 1, pp. 105–116, 2015.
- [63] D. M. Abraham *et al.*, “ β -Arrestin mediates the Frank-Starling mechanism of cardiac contractility,” *Proc. Natl. Acad. Sci. U. S. A.*, Nov. 2016.
- [64] K. G. Shyu, C. C. Chen, B. W. Wang, and P. Kuan, “Angiotensin II receptor antagonist blocks the expression of connexin43 induced by cyclical mechanical stretch in cultured neonatal rat cardiac myocytes,” *J. Mol. Cell. Cardiol.*, vol. 33, no. 4, pp. 691–698, Apr. 2001.
- [65] A. Leri *et al.*, “Stretch-mediated release of angiotensin II induces myocyte apoptosis by activating p53 that enhances the local renin-angiotensin system and decreases the Bcl-2-to-Bax protein ratio in the cell,” *J. Clin. Invest.*, vol. 101, no. 7, pp. 1326–1342, Apr. 1998.
- [66] T. G. von Lueder and H. Krum, “RAAS inhibitors and cardiovascular protection in large scale trials,” *Cardiovasc. Drugs Ther.*, vol. 27, no. 2, pp. 171–179, Apr. 2013.
- [67] W. Sigurdson, A. Ruknudin, and F. Sachs, “Calcium imaging of mechanically induced fluxes in tissue-cultured chick heart: role of stretch-activated ion channels,” *Am. J. Physiol.*, vol. 262, no. 4 Pt 2, pp. H1110–1115, Apr. 1992.
- [68] J. Sadoshima and S. Izumo, “Mechanical stretch rapidly activates multiple signal transduction pathways in cardiac myocytes: potential involvement of an autocrine/paracrine mechanism,” *EMBO J.*, vol. 12, no. 4, pp. 1681–1692, Apr. 1993.
- [69] I. Komuro, S. Kudo, T. Yamazaki, Y. Zou, I. Shiojima, and Y. Yazaki, “Mechanical stretch activates the stress-activated protein kinases in cardiac myocytes,” *FASEB J. Off. Publ. Fed. Am. Soc. Exp. Biol.*, vol. 10, no. 5, pp. 631–636, Apr. 1996.
- [70] G. L. Lyford *et al.*, “alpha(1C) (Ca(V)1.2) L-type calcium channel mediates mechanosensitive calcium regulation,” *Am. J. Physiol. Cell Physiol.*, vol. 283, no. 3, pp. C1001–1008, Sep. 2002.
- [71] N. Matsuda, N. Hagiwara, M. Shoda, H. Kasanuki, and S. Hosoda, “Enhancement of the L-type Ca²⁺ current by mechanical stimulation in single rabbit cardiac myocytes,” *Circ. Res.*, vol. 78, no. 4, pp. 650–659, Apr. 1996.
- [72] C. Ruwhof, J. T. van Wamel, L. A. Noordzij, S. Aydin, J. C. Harper, and A. van der Laarse, “Mechanical stress stimulates phospholipase C activity and intracellular calcium ion levels in neonatal rat cardiomyocytes,” *Cell Calcium*, vol. 29, no. 2, pp. 73–83, Feb. 2001.
- [73] S.-Q. Peng, R. K. Hajela, and W. D. Atchison, “Fluid flow-induced increase in inward Ba²⁺ current expressed in HEK293 cells transiently transfected with human neuronal L-type Ca²⁺ channels,” *Brain Res.*, vol. 1045, no. 1–2, pp. 116–123, May 2005.
- [74] C. Zobel *et al.*, “Mechanisms of Ca²⁺-dependent calcineurin activation in mechanical stretch-induced hypertrophy,” *Cardiology*, vol. 107, no. 4, pp. 281–290, 2007.
- [75] A. O. Rosa, N. Yamaguchi, and M. Morad, “Mechanical regulation of native and the recombinant calcium channel,” *Cell Calcium*, vol. 53, no. 4, pp. 264–274, Apr. 2013.

- [76] Y. Katanosaka *et al.*, “TRPV2 is critical for the maintenance of cardiac structure and function in mice,” *Nat. Commun.*, vol. 5, p. 3932, 2014.
- [77] M. A. Spassova, T. Hewavitharana, W. Xu, J. Soboloff, and D. L. Gill, “A common mechanism underlies stretch activation and receptor activation of TRPC6 channels,” *Proc. Natl. Acad. Sci. U. S. A.*, vol. 103, no. 44, pp. 16586–16591, Oct. 2006.
- [78] S. Loukin, X. Zhou, Z. Su, Y. Saimi, and C. Kung, “Wild-type and brachyolmia-causing mutant TRPV4 channels respond directly to stretch force,” *J. Biol. Chem.*, vol. 285, no. 35, pp. 27176–27181, Aug. 2010.
- [79] J. Teng, S. Loukin, X. Zhou, and C. Kung, “Yeast luminometric and *Xenopus* oocyte electrophysiological examinations of the molecular mechanosensitivity of TRPV4,” *J. Vis. Exp. JoVE*, no. 82, Dec. 2013.
- [80] Y. Qi *et al.*, “Uniaxial cyclic stretch stimulates TRPV4 to induce realignment of human embryonic stem cell-derived cardiomyocytes,” *J. Mol. Cell. Cardiol.*, vol. 87, pp. 65–73, Oct. 2015.
- [81] B. M. Cadre, M. Qi, D. M. Eble, T. R. Shannon, D. M. Bers, and A. M. Samarel, “Cyclic stretch down-regulates calcium transporter gene expression in neonatal rat ventricular myocytes,” *J. Mol. Cell. Cardiol.*, vol. 30, no. 11, pp. 2247–2259, Nov. 1998.
- [82] J. Heineke *et al.*, “Attenuation of cardiac remodeling after myocardial infarction by muscle LIM protein-calcineurin signaling at the sarcomeric Z-disc,” *Proc. Natl. Acad. Sci. U. S. A.*, vol. 102, no. 5, pp. 1655–1660, Feb. 2005.
- [83] D. Jeong *et al.*, “PICOT attenuates cardiac hypertrophy by disrupting calcineurin-NFAT signaling,” *Circ. Res.*, vol. 102, no. 6, pp. 711–719, Mar. 2008.
- [84] A. V. Finsen *et al.*, “Syndecan-4 is essential for development of concentric myocardial hypertrophy via stretch-induced activation of the calcineurin-NFAT pathway,” *PloS One*, vol. 6, no. 12, p. e28302, 2011.
- [85] R. Peyronnet, J. M. Nerbonne, and P. Kohl, “Cardiac Mechano-Gated Ion Channels and Arrhythmias,” *Circ. Res.*, vol. 118, no. 2, pp. 311–329, Jan. 2016.
- [86] J. Striessnig, N. J. Ortner, and A. Pinggera, “Pharmacology of L-type Calcium Channels: Novel Drugs for Old Targets?,” *Curr. Mol. Pharmacol.*, vol. 8, no. 2, pp. 110–122, 2015.
- [87] P. Eder and J. D. Molkentin, “TRPC channels as effectors of cardiac hypertrophy,” *Circ. Res.*, vol. 108, no. 2, pp. 265–272, Jan. 2011.
- [88] N. Wang, J. P. Butler, and D. E. Ingber, “Mechanotransduction across the cell surface and through the cytoskeleton,” *Science*, vol. 260, no. 5111, pp. 1124–1127, May 1993.
- [89] M. L. McCain and K. K. Parker, “Mechanotransduction: the role of mechanical stress, myocyte shape, and cytoskeletal architecture on cardiac function,” *Pflug. Arch. Eur. J. Physiol.*, vol. 462, no. 1, pp. 89–104, Jul. 2011.
- [90] D. Kuppuswamy, C. Kerr, T. Narishige, V. S. Kasi, D. R. Menick, and G. Cooper, “Association of tyrosine-phosphorylated c-Src with the cytoskeleton of hypertrophying myocardium,” *J. Biol. Chem.*, vol. 272, no. 7, pp. 4500–4508, Feb. 1997.
- [91] S. J. Zhang, G. A. Truskey, and W. E. Kraus, “Effect of cyclic stretch on beta1D-integrin expression and activation of FAK and RhoA,” *Am. J. Physiol. Cell Physiol.*, vol. 292, no. 6, pp. C2057–2069, Jun. 2007.
- [92] J. M. Ervasti and K. P. Campbell, “A role for the dystrophin-glycoprotein complex as a transmembrane linker between laminin and actin,” *J. Cell Biol.*, vol. 122, no. 4, pp. 809–823, Aug. 1993.
- [93] J. F. Garbincius and D. E. Michele, “Dystrophin-glycoprotein complex regulates muscle nitric oxide production through mechanoregulation of AMPK signaling,” *Proc. Natl. Acad. Sci. U. S. A.*, vol. 112, no. 44, pp. 13663–13668, Nov. 2015.
- [94] M. S. Barnabei and J. M. Metzger, “Ex vivo stretch reveals altered mechanical properties of isolated dystrophin-deficient hearts,” *PloS One*, vol. 7, no. 3, p. e32880, 2012.

- [95] M. Yamane, T. Matsuda, T. Ito, Y. Fujio, K. Takahashi, and J. Azuma, "Rac1 activity is required for cardiac myocyte alignment in response to mechanical stress," *Biochem. Biophys. Res. Commun.*, vol. 353, no. 4, pp. 1023–1027, Feb. 2007.
- [96] A. Salameh *et al.*, "Cyclic mechanical stretch induces cardiomyocyte orientation and polarization of the gap junction protein connexin43," *Circ. Res.*, vol. 106, no. 10, pp. 1592–1602, May 2010.
- [97] A. Kumar, I. Chaudhry, M. B. Reid, and A. M. Boriek, "Distinct signaling pathways are activated in response to mechanical stress applied axially and transversely to skeletal muscle fibers," *J. Biol. Chem.*, vol. 277, no. 48, pp. 46493–46503, Nov. 2002.
- [98] S. E. Senyo, Y. E. Koshman, and B. Russell, "Stimulus interval, rate and direction differentially regulate phosphorylation for mechanotransduction in neonatal cardiac myocytes," *FEBS Lett.*, vol. 581, no. 22, pp. 4241–4247, Sep. 2007.
- [99] F. Liang and D. G. Gardner, "Autocrine/paracrine determinants of strain-activated brain natriuretic peptide gene expression in cultured cardiac myocytes," *J. Biol. Chem.*, vol. 273, no. 23, pp. 14612–14619, Jun. 1998.
- [100] M. Harada *et al.*, "Interaction of myocytes and nonmyocytes is necessary for mechanical stretch to induce ANP/BNP production in cardiocyte culture," *J. Cardiovasc. Pharmacol.*, vol. 31 Suppl 1, pp. S357–359, 1998.
- [101] C. Ruwhof, A. E. van Wamel, J. M. Egas, and A. van der Laarse, "Cyclic stretch induces the release of growth promoting factors from cultured neonatal cardiomyocytes and cardiac fibroblasts," *Mol. Cell. Biochem.*, vol. 208, no. 1–2, pp. 89–98, May 2000.
- [102] S. Honscho *et al.*, "Pressure-mediated hypertrophy and mechanical stretch induces IL-1 release and subsequent IGF-1 generation to maintain compensative hypertrophy by affecting Akt and JNK pathways," *Circ. Res.*, vol. 105, no. 11, pp. 1149–1158, Nov. 2009.
- [103] K. A. Janes *et al.*, "An engineering design approach to systems biology," *Integr. Biol. Quant. Biosci. Nano Macro*, Jun. 2017.
- [104] J. H. Yang and J. J. Saucerman, "Computational models reduce complexity and accelerate insight into cardiac signaling networks," *Circ. Res.*, vol. 108, no. 1, pp. 85–97, Jan. 2011.
- [105] M. J. Kraeutler, A. R. Soltis, and J. J. Saucerman, "Modeling cardiac β -adrenergic signaling with normalized-Hill differential equations: comparison with a biochemical model," *BMC Syst. Biol.*, vol. 4, p. 157, 2010.
- [106] B. T. Grys *et al.*, "Machine learning and computer vision approaches for phenotypic profiling," *J. Cell Biol.*, vol. 216, no. 1, pp. 65–71, Jan. 2017.
- [107] G. T. Bass *et al.*, "Automated image analysis identifies signaling pathways regulating distinct signatures of cardiac myocyte hypertrophy," *J. Mol. Cell. Cardiol.*, vol. 52, no. 5, pp. 923–930, May 2012.
- [108] J. Lammerding, R. D. Kamm, and R. T. Lee, "Mechanotransduction in cardiac myocytes," *Ann. N. Y. Acad. Sci.*, vol. 1015, pp. 53–70, May 2004.
- [109] J. H. Omens, A. D. McCulloch, and I. Lorenzen-Schmidt, "Mechanotransduction in cardiac remodeling and heart failure," in *Cardiac Mechanotransduction*, Book, Section vols., M. Weckström and P. Tavi, Eds. New York: Springer, 2007, pp. 78–92.
- [110] B. Nadal-Ginard, J. Kajstura, P. Anversa, and A. Leri, "A matter of life and death: cardiac myocyte apoptosis and regeneration," *J. Clin. Invest.*, vol. 111, no. 10, pp. 1457–1459, May 2003.
- [111] R. C. Lyon, F. Zanella, J. H. Omens, and F. Sheikh, "Mechanotransduction in cardiac hypertrophy and failure," *Circ. Res.*, vol. 116, no. 8, pp. 1462–1476, Apr. 2015.
- [112] A. C. Zeigler, W. J. Richardson, J. W. Holmes, and J. J. Saucerman, "A computational model of cardiac fibroblast signaling predicts context-dependent drivers of myofibroblast differentiation," *J. Mol. Cell. Cardiol.*, vol. 94, pp. 72–81, May 2016.
- [113] R. C. P. Kerckhoffs, J. Omens, and A. D. McCulloch, "A single strain-based growth law predicts concentric and eccentric cardiac growth during pressure and volume overload," *Mech. Res. Commun.*, vol. 42, pp. 40–50, Jun. 2012.

- [114] K. K. Chiou *et al.*, “Mechanical signaling coordinates the embryonic heartbeat,” *Proc. Natl. Acad. Sci. U. S. A.*, Jul. 2016.
- [115] O. Cohen and S. A. Safran, “Elastic interactions synchronize beating in cardiomyocytes,” *Soft Matter*, vol. 12, no. 28, pp. 6088–6095, Jul. 2016.
- [116] Y. Aratyn-Schaus *et al.*, “Coupling primary and stem cell-derived cardiomyocytes in an in vitro model of cardiac cell therapy,” *J. Cell Biol.*, vol. 212, no. 4, pp. 389–397, Feb. 2016.
- [117] E. Pueyo, M. Orini, J. F. Rodríguez, and P. Taggart, “Interactive effect of beta-adrenergic stimulation and mechanical stretch on low-frequency oscillations of ventricular action potential duration in humans,” *J. Mol. Cell. Cardiol.*, vol. 97, pp. 93–105, May 2016.
- [118] M. Cockerill, M. K. Rigozzi, and E. M. Terentjev, “Mechanosensitivity of the 2nd Kind: TGF- β Mechanism of Cell Sensing the Substrate Stiffness,” *PLoS One*, vol. 10, no. 10, p. e0139959, 2015.
- [119] C. Schmidt, H. Pommerenke, F. Dürr, B. Nebe, and J. Rychly, “Mechanical stressing of integrin receptors induces enhanced tyrosine phosphorylation of cytoskeletally anchored proteins,” *J. Biol. Chem.*, vol. 273, no. 9, pp. 5081–5085, Feb. 1998.
- [120] V. Straub, R. E. Bittner, J. J. Léger, and T. Voit, “Direct visualization of the dystrophin network on skeletal muscle fiber membrane,” *J. Cell Biol.*, vol. 119, no. 5, pp. 1183–1191, Dec. 1992.
- [121] H. E. Cingolani and I. L. Ennis, “Sodium-hydrogen exchanger, cardiac overload, and myocardial hypertrophy,” *Circulation*, vol. 115, no. 9, pp. 1090–1100, Mar. 2007.
- [122] T. Yamazaki *et al.*, “Endothelin-1 is involved in mechanical stress-induced cardiomyocyte hypertrophy,” *J. Biol. Chem.*, vol. 271, no. 6, pp. 3221–3228, Feb. 1996.
- [123] E. J. Cox and S. A. Marsh, “A systematic review of fetal genes as biomarkers of cardiac hypertrophy in rodent models of diabetes,” *PLoS One*, vol. 9, no. 3, p. e92903, 2014.
- [124] A. R. Soltis and J. J. Saucerman, “Robustness portraits of diverse biological networks conserved despite order-of-magnitude parameter uncertainty,” *Bioinforma. Oxf. Engl.*, vol. 27, no. 20, pp. 2888–2894, Oct. 2011.
- [125] E. C. Greenwald, J. M. Redden, K. L. Dodge-Kafka, and J. J. Saucerman, “Scaffold state switching amplifies, accelerates, and insulates protein kinase C signaling,” *J. Biol. Chem.*, vol. 289, no. 4, pp. 2353–2360, Jan. 2014.
- [126] K. Tamura *et al.*, “Activation of angiotensinogen gene in cardiac myocytes by angiotensin II and mechanical stretch,” *Am. J. Physiol.*, vol. 275, no. 1 Pt 2, pp. R1-9, Jul. 1998.
- [127] D. Frank *et al.*, “Gene expression pattern in biomechanically stretched cardiomyocytes: evidence for a stretch-specific gene program,” *Hypertension*, vol. 51, no. 2, pp. 309–318, Feb. 2008.
- [128] E. Dirkx, P. A. da Costa Martins, and L. J. De Windt, “Regulation of fetal gene expression in heart failure,” *Biochim. Biophys. Acta*, vol. 1832, no. 12, pp. 2414–2424, Dec. 2013.
- [129] J. B. Fitzgerald, B. Schoeberl, U. B. Nielsen, and P. K. Sorger, “Systems biology and combination therapy in the quest for clinical efficacy,” *Nat. Chem. Biol.*, vol. 2, no. 9, pp. 458–466, Sep. 2006.
- [130] P. J. Yeh, M. J. Hegreness, A. P. Aiden, and R. Kishony, “Drug interactions and the evolution of antibiotic resistance,” *Nat. Rev. Microbiol.*, vol. 7, no. 6, pp. 460–466, Jun. 2009.
- [131] H. Hasegawa, H. Takano, and Y. Zou, “Second messenger systems involved in heart mechanotransduction,” in *Cardiac Mechanotransduction*, Book, Section vols., H. Akazawa and I. Komuro, Eds. New York: Springer, 2007, pp. 93–105.
- [132] H. E. Cingolani, B. V. Alvarez, I. L. Ennis, and M. C. Camilión de Hurtado, “Stretch-induced alkalization of feline papillary muscle: an autocrine-paracrine system,” *Circ. Res.*, vol. 83, no. 8, pp. 775–780, Oct. 1998.
- [133] H. Leskinen, O. Vuolteenaho, and H. Ruskoaho, “Combined inhibition of endothelin and angiotensin II receptors blocks volume load-induced cardiac hormone release,” *Circ. Res.*, vol. 80, no. 1, pp. 114–123, Jan. 1997.
- [134] S. I. Berger and R. Iyengar, “Network analyses in systems pharmacology,” *Bioinforma. Oxf. Engl.*, vol. 25, no. 19, pp. 2466–2472, Oct. 2009.

- [135] A. Chopra, E. Tabdanov, H. Patel, P. A. Janmey, and J. Y. Kresh, "Cardiac myocyte remodeling mediated by N-cadherin-dependent mechanosensing," *Am. J. Physiol. Heart Circ. Physiol.*, vol. 300, no. 4, pp. H1252-1266, Apr. 2011.
- [136] K. Dasbiswas, E. Alster, and S. A. Safran, "Mechanobiological induction of long-range contractility by diffusing biomolecules and size scaling in cell assemblies," *Sci. Rep.*, vol. 6, p. 27692, Jun. 2016.
- [137] B. V. Alvarez, N. G. Pérez, I. L. Ennis, M. C. Camili6n de Hurtado, and H. E. Cingolani, "Mechanisms underlying the increase in force and Ca(2+) transient that follow stretch of cardiac muscle: a possible explanation of the Anrep effect," *Circ. Res.*, vol. 85, no. 8, pp. 716-722, Oct. 1999.
- [138] S. C. Calaghan and E. White, "Contribution of angiotensin II, endothelin 1 and the endothelium to the slow inotropic response to stretch in ferret papillary muscle," *Pflugers Arch.*, vol. 441, no. 4, pp. 514-520, Jan. 2001.
- [139] D. von Lewinski, B. Stumme, L. S. Maier, C. Luers, D. M. Bers, and B. Pieske, "Stretch-dependent slow force response in isolated rabbit myocardium is Na+ dependent," *Cardiovasc. Res.*, vol. 57, no. 4, pp. 1052-1061, Mar. 2003.
- [140] D. von Lewinski, B. Stumme, F. Fialka, C. Luers, and B. Pieske, "Functional relevance of the stretch-dependent slow force response in failing human myocardium," *Circ. Res.*, vol. 94, no. 10, pp. 1392-1398, May 2004.
- [141] B. Bernardo, K. Weeks, L. Pretorius, and J. McMullen, "Molecular distinction between physiological and pathological cardiac hypertrophy: Experimental findings and therapeutic strategies," *Pharmacol. Ther.*, vol. 128, no. 1, pp. 191-227, Oct. 2010.
- [142] S. P. Barry, S. M. Davidson, and P. A. Townsend, "Molecular regulation of cardiac hypertrophy," *Int. J. Biochem. Cell Biol.*, vol. 40, no. 10, pp. 2023-2039, 2008.
- [143] G. Dorn, "Pharmacogenetic profiling in the treatment of heart disease," *Transl. Res. J. Lab. Clin. Med.*, vol. 154, no. 6, pp. 295-302, Dec. 2009.
- [144] T. D. Schmittgen and K. J. Livak, "Analyzing real-time PCR data by the comparative C(T) method," *Nat. Protoc.*, vol. 3, no. 6, pp. 1101-1108, 2008.
- [145] M. P. Scheid, P. A. Marignani, and J. R. Woodgett, "Multiple phosphoinositide 3-kinase-dependent steps in activation of protein kinase B," *Mol. Cell. Biol.*, vol. 22, no. 17, pp. 6247-6260, Sep. 2002.
- [146] Z. Moon, Y. Wang, N. Aryan, D. D. Mousseau, and M. P. Scheid, "Serine 396 of PDK1 is required for maximal PKB activation," *Cell. Signal.*, vol. 20, no. 11, pp. 2038-2049, Nov. 2008.
- [147] C. Rommel *et al.*, "Mediation of IGF-1-induced skeletal myotube hypertrophy by PI(3)K/Akt/mTOR and PI(3)K/Akt/GSK3 pathways," *Nat. Cell Biol.*, vol. 3, no. 11, pp. 1009-1013, Nov. 2001.
- [148] H. Nojima *et al.*, "The mammalian target of rapamycin (mTOR) partner, raptor, binds the mTOR substrates p70 S6 kinase and 4E-BP1 through their TOR signaling (TOS) motif," *J. Biol. Chem.*, vol. 278, no. 18, pp. 15461-15464, May 2003.
- [149] A. Ashkenazi, "Directing cancer cells to self-destruct with pro-apoptotic receptor agonists," *Nat. Rev. Drug Discov.*, vol. 7, no. 12, pp. 1001-1012, Dec. 2008.
- [150] S. Piccolo, S. Dupont, and M. Cordenonsi, "The biology of YAP/TAZ: hippo signaling and beyond," *Physiol. Rev.*, vol. 94, no. 4, pp. 1287-1312, Oct. 2014.
- [151] R. E. Ferguson, H. P. Carroll, A. Harris, E. R. Maher, P. J. Selby, and R. E. Banks, "Housekeeping proteins: a preliminary study illustrating some limitations as useful references in protein expression studies," *Proteomics*, vol. 5, no. 2, pp. 566-571, Feb. 2005.
- [152] K. A. Janes, J. G. Albeck, S. Gaudet, P. K. Sorger, D. A. Lauffenburger, and M. B. Yaffe, "A systems model of signaling identifies a molecular basis set for cytokine-induced apoptosis," *Science*, vol. 310, no. 5754, pp. 1646-1653, Dec. 2005.
- [153] R. Aikawa *et al.*, "Insulin prevents cardiomyocytes from oxidative stress-induced apoptosis through activation of PI3 kinase/Akt," *Circulation*, vol. 102, no. 23, pp. 2873-2879, Dec. 2000.
- [154] I. Shiraiishi *et al.*, "Nuclear targeting of Akt enhances kinase activity and survival of cardiomyocytes," *Circ. Res.*, vol. 94, no. 7, pp. 884-891, Apr. 2004.

- [155] V. J. Bezzerides *et al.*, “CITED4 induces physiologic hypertrophy and promotes functional recovery after ischemic injury,” *JCI Insight*, vol. 1, no. 9, Jun. 2016.
- [156] J. Kajstura *et al.*, “Angiotensin II induces apoptosis of adult ventricular myocytes in vitro,” *J. Mol. Cell. Cardiol.*, vol. 29, no. 3, pp. 859–870, Mar. 1997.
- [157] A. González *et al.*, “Stimulation of cardiac apoptosis in essential hypertension: potential role of angiotensin II,” *Hypertens. Dallas Tex 1979*, vol. 39, no. 1, pp. 75–80, Jan. 2002.
- [158] M. Maillat, J. H. van Berlo, and J. D. Molkentin, “Molecular basis of physiological heart growth: fundamental concepts and new players,” *Nat. Rev. Mol. Cell Biol.*, vol. 14, no. 1, pp. 38–48, Jan. 2013.
- [159] B. I. Jugdutt, “Preventing adverse remodeling and rupture during healing after myocardial infarction in mice and humans,” *Circulation*, vol. 122, no. 2, pp. 103–105, Jul. 2010.
- [160] C. L. Galindo, S. Ryzhov, and D. B. Sawyer, “Neuregulin as a heart failure therapy and mediator of reverse remodeling,” *Curr. Heart Fail. Rep.*, vol. 11, no. 1, pp. 40–49, Mar. 2014.
- [161] M. L. Miller *et al.*, “Drug synergy screen and network modeling in dedifferentiated liposarcoma identifies CDK4 and IGF1R as synergistic drug targets,” *Sci. Signal.*, vol. 6, no. 294, p. ra85, Sep. 2013.
- [162] M. Fallahi-Sichani, N. J. Moerke, M. Niepel, T. Zhang, N. S. Gray, and P. K. Sorger, “Systematic analysis of BRAF(V600E) melanomas reveals a role for JNK/c-Jun pathway in adaptive resistance to drug-induced apoptosis,” *Mol. Syst. Biol.*, vol. 11, no. 3, p. 797, Mar. 2015.
- [163] D. L. Mann, P. M. Barger, and D. Burkhoff, “Myocardial recovery and the failing heart: myth, magic, or molecular target?,” *J. Am. Coll. Cardiol.*, vol. 60, no. 24, pp. 2465–2472, Dec. 2012.
- [164] T. A. McKinsey and D. A. Kass, “Small-molecule therapies for cardiac hypertrophy: moving beneath the cell surface,” *Nat. Rev. Drug Discov.*, vol. 6, no. 8, pp. 617–635, Aug. 2007.
- [165] P. M. McLendon *et al.*, “An Unbiased High Throughput Screen to Identify Novel Effectors that Impact on Cardiomyocyte Aggregate Levels,” *Circ. Res.*, Jun. 2017.
- [166] J. G. Evans and P. Matsudaira, “Linking microscopy and high content screening in large-scale biomedical research,” *Methods Mol. Biol. Clifton NJ*, vol. 356, pp. 33–38, 2007.
- [167] A. E. Carpenter *et al.*, “CellProfiler: image analysis software for identifying and quantifying cell phenotypes,” *Genome Biol.*, vol. 7, no. 10, p. R100, 2006.
- [168] L. Kamensky *et al.*, “Improved structure, function and compatibility for CellProfiler: modular high-throughput image analysis software,” *Bioinforma. Oxf. Engl.*, vol. 27, no. 8, pp. 1179–1180, Apr. 2011.
- [169] F. D. Sigoillot and R. W. King, “Vigilance and validation: Keys to success in RNAi screening,” *ACS Chem. Biol.*, vol. 6, no. 1, pp. 47–60, Jan. 2011.
- [170] R. M. Haralick, K. Shanmugam, and I. Dinstein, “Textural Features for Image Classification,” *IEEE Trans. Syst. Man Cybern.*, vol. SMC-3, no. 6, pp. 610–621, Nov. 1973.
- [171] S. Mockenhaupt, S. Grosse, D. Rupp, R. Bartenschlager, and D. Grimm, “Alleviation of off-target effects from vector-encoded shRNAs via codelivered RNA decoys,” *Proc. Natl. Acad. Sci. U. S. A.*, vol. 112, no. 30, pp. E4007–4016, Jul. 2015.
- [172] X. Lin *et al.*, “siRNA-mediated off-target gene silencing triggered by a 7 nt complementation,” *Nucleic Acids Res.*, vol. 33, no. 14, pp. 4527–4535, 2005.
- [173] I. Sudbery, A. J. Enright, A. G. Fraser, and I. Dunham, “Systematic analysis of off-target effects in an RNAi screen reveals microRNAs affecting sensitivity to TRAIL-induced apoptosis,” *BMC Genomics*, vol. 11, p. 175, Mar. 2010.
- [174] A. L. Jackson *et al.*, “Expression profiling reveals off-target gene regulation by RNAi,” *Nat. Biotechnol.*, vol. 21, no. 6, pp. 635–637, Jun. 2003.
- [175] A. Birmingham *et al.*, “3’ UTR seed matches, but not overall identity, are associated with RNAi off-targets,” *Nat. Methods*, vol. 3, no. 3, pp. 199–204, Mar. 2006.
- [176] A. L. Jackson *et al.*, “Widespread siRNA ‘off-target’ transcript silencing mediated by seed region sequence complementarity,” *RNA N. Y. N.*, vol. 12, no. 7, pp. 1179–1187, Jul. 2006.

- [177] C. Tschuch *et al.*, “Off-target effects of siRNA specific for GFP,” *BMC Mol. Biol.*, vol. 9, p. 60, Jun. 2008.
- [178] J. W. Myers, J.-T. Chi, D. Gong, M. E. Schaner, P. O. Brown, and J. E. Ferrell, “Minimizing off-target effects by using diced siRNAs for RNA interference,” *J. RNAi Gene Silenc. Int. J. RNA Gene Target. Res.*, vol. 2, no. 2, pp. 181–194, Jul. 2006.
- [179] A. Subramanian *et al.*, “Gene set enrichment analysis: a knowledge-based approach for interpreting genome-wide expression profiles,” *Proc. Natl. Acad. Sci. U. S. A.*, vol. 102, no. 43, pp. 15545–15550, Oct. 2005.
- [180] E. Y. Chen *et al.*, “Enrichr: interactive and collaborative HTML5 gene list enrichment analysis tool,” *BMC Bioinformatics*, vol. 14, p. 128, Apr. 2013.
- [181] M. V. Kuleshov *et al.*, “Enrichr: a comprehensive gene set enrichment analysis web server 2016 update,” *Nucleic Acids Res.*, vol. 44, no. W1, pp. W90–97, 08 2016.
- [182] A. Steffen *et al.*, “Sra-1 and Nap1 link Rac to actin assembly driving lamellipodia formation,” *EMBO J.*, vol. 23, no. 4, pp. 749–759, Feb. 2004.
- [183] S. Nakao, A. Platek, S. Hirano, and M. Takeichi, “Contact-dependent promotion of cell migration by the OL-protocadherin-Nap1 interaction,” *J. Cell Biol.*, vol. 182, no. 2, pp. 395–410, Jul. 2008.
- [184] A. S. Rakeman and K. V. Anderson, “Axis specification and morphogenesis in the mouse embryo require Nap1, a regulator of WAVE-mediated actin branching,” *Dev. Camb. Engl.*, vol. 133, no. 16, pp. 3075–3083, Aug. 2006.
- [185] R. E. Hershberger *et al.*, “Clinical and functional characterization of TNNT2 mutations identified in patients with dilated cardiomyopathy,” *Circ. Cardiovasc. Genet.*, vol. 2, no. 4, pp. 306–313, Aug. 2009.
- [186] L. Núñez *et al.*, “Somatic MYH7, MYBPC3, TPM1, TNNT2 and TNNI3 mutations in sporadic hypertrophic cardiomyopathy,” *Circ. J. Off. J. Jpn. Circ. Soc.*, vol. 77, no. 9, pp. 2358–2365, 2013.
- [187] K. Nishii *et al.*, “Targeted disruption of the cardiac troponin T gene causes sarcomere disassembly and defects in heartbeat within the early mouse embryo,” *Dev. Biol.*, vol. 322, no. 1, pp. 65–73, Oct. 2008.
- [188] M. D. Sutcliffe, P. M. Tan, A. Fernandez-Perez, Y.-J. Nam, N. V. Munshi, and J. J. Saucerman, “High content analysis identifies unique morphological features of reprogrammed cardiomyocytes,” *Sci. Rep.*, vol. 8, no. 1, p. 1258, Jan. 2018.
- [189] S. L. K. Bowers, W. A. McFadden, T. K. Borg, and T. A. Baudino, “Desmoplakin is important for proper cardiac cell-cell interactions,” *Microsc. Microanal. Off. J. Microsc. Soc. Am. Microbeam Anal. Soc. Microsc. Soc. Can.*, vol. 18, no. 1, pp. 107–114, Feb. 2012.
- [190] R. Martherus *et al.*, “Accelerated cardiac remodeling in desmoplakin transgenic mice in response to endurance exercise is associated with perturbed Wnt/ β -catenin signaling,” *Am. J. Physiol. Heart Circ. Physiol.*, vol. 310, no. 2, pp. H174–187, Jan. 2016.
- [191] J. S. Logue, A. X. Cartagena-Rivera, M. A. Baird, M. W. Davidson, R. S. Chadwick, and C. M. Waterman, “Erk regulation of actin capping and bundling by Eps8 promotes cortex tension and leader bleb-based migration,” *eLife*, vol. 4, p. e08314, Jul. 2015.
- [192] M. Ding, R. S. King, E. C. Berry, Y. Wang, J. Hardin, and A. D. Chisholm, “The cell signaling adaptor protein EPS-8 is essential for *C. elegans* epidermal elongation and interacts with the ankyrin repeat protein VAB-19,” *PLoS One*, vol. 3, no. 10, p. e3346, Oct. 2008.
- [193] M. M. LeWinter and H. L. Granzier, “Cardiac titin and heart disease,” *J. Cardiovasc. Pharmacol.*, vol. 63, no. 3, pp. 207–212, Mar. 2014.
- [194] L. Carrier, G. Mearini, K. Stathopoulou, and F. Cuello, “Cardiac myosin-binding protein C (MYBPC3) in cardiac pathophysiology,” *Gene*, vol. 573, no. 2, pp. 188–197, Dec. 2015.
- [195] D. S. Herman *et al.*, “Truncations of titin causing dilated cardiomyopathy,” *N. Engl. J. Med.*, vol. 366, no. 7, pp. 619–628, Feb. 2012.
- [196] J. T. Hinson *et al.*, “HEART DISEASE. Titin mutations in iPS cells define sarcomere insufficiency as a cause of dilated cardiomyopathy,” *Science*, vol. 349, no. 6251, pp. 982–986, Aug. 2015.

- [197] D. Barefield *et al.*, “Haploinsufficiency of MYBPC3 exacerbates the development of hypertrophic cardiomyopathy in heterozygous mice,” *J. Mol. Cell. Cardiol.*, vol. 79, pp. 234–243, Feb. 2015.
- [198] H. Morita *et al.*, “Shared genetic causes of cardiac hypertrophy in children and adults,” *N. Engl. J. Med.*, vol. 358, no. 18, pp. 1899–1908, May 2008.
- [199] L. Waller and L. Tian, “Computational imaging: Machine learning for 3D microscopy,” *Nature*, vol. 523, no. 7561, pp. 416–417, Jul. 2015.
- [200] I. J. Goodfellow *et al.*, “Challenges in representation learning: a report on three machine learning contests,” *Neural Netw. Off. J. Int. Neural Netw. Soc.*, vol. 64, pp. 59–63, Apr. 2015.
- [201] B. K. Lundholt, K. M. Scudder, and L. Pagliaro, “A simple technique for reducing edge effect in cell-based assays,” *J. Biomol. Screen.*, vol. 8, no. 5, pp. 566–570, Oct. 2003.
- [202] K. S. Buchholz, P. Tan, A. C. Zambon, J. J. Saucerman, A. D. McCulloch, and J. H. Omens, “Cardiac Stretch-Induced Transcriptomic Changes Are Direction Dependent,” *FASEB J.*, vol. 30, no. 1_supplement, pp. 1277.6-1277.6, Apr. 2016.